HIGH ACCURACY MESHFREE METHODS FOR WEAKLY COMPRESSIBILE FLUID AND ASSOCIATED APPLICATIONS IN LASER INDUCED EXPLOSIVE BOILING

A Dissertation

by

YU YANG

Submitted to the Office of Graduate and Professional Studies of
Texas A&M University
in partial fulfillment of the requirements for the degree of

DOCTOR OF PHILOSOPHY

Chair of Committee,	Sy-Bor Wen
Committee Members,	Debjyoti Banerjee
	David Staack
	Philip Hemmer
Head of Department,	Andreas A. Polycarpou

May 2017

Major Subject: Mechanical Engineering

ABSTRACT

Laser induced explosive boiling (LIEB) generated by localized high energy laser on solid surface has wide applications. Compared with traditional electric heating induced phase change process, LIEB has advantages in: (a) controllable ultra-short heating time, (b) no-pretreatment/fabrication required on substrate, (c) fully controllable heating size as well as heating energy.

In this study, we utilized laser induced strong local heating by guiding laser into taped micro-nozzle to induce liquid ejection from the nozzle. The localized strong heating induces rapid phase change of ink liquid inside the nozzle. As a result, high pressure can be generated inside nozzle and can squeeze liquid out from the nozzle. This inkjet process has less limitation in ink materials than current inkjet techniques. By adjusting laser energy and laser pulse duration, we are able to generate different ink patterns vary from single droplet to ink spray consisted of sub-micron droplets.

To better understand and control the LIEB process for construction laser inkjets, meshfree numerical analysis capable to study a LIEB process is also explored in this study. SPH was selected as the starting point of the meshfree numerical simulation considering its advantages in simulation of large distortion of free surface and moving interface of two phase flow. With a gaining experience in SPH, we noticed that it has limitations in achieving high enough numerical accuracy in derivative computing as well as providing stable numerical simulation without artificial smoothing processes. These limitations of traditional SPH prevent us from using SPH as a tool directly to study the LIEB.

To solve the limitations of traditional SPH, we developed a new meshfree scheme providing following improvements: (a) using equation of state of fluid directly, which handles the P, ρ, T relation as well as the associated buoyancy forces without simplifications; (b) higher order accuracy in 1^{st} and 2^{nd} derivatives calculation providing 2^{nd} and 1^{st} order accuracy for random particle distribution and even higher accuracy for symmetric conditions. With this novel high order accuracy meshfree scheme developed in this study, we have a tool not only to stimulate the LIEB process but also bubble dynamics and micro cavitation directly.

ACKNOWLEDGEMENTS

I wish to express my sincere gratitude to my advisor, Dr. Sy-Bor Wen, for his guidance and advice during my Ph.D study. Also, I would like to thank my committee members, Dr. Banerjee, Dr. Staack, and Dr. Hemmer for their kind help and support. Thanks to Dr. Philip Hemmer for allowing us to use his lab facility.

I would like to thank my colleagues, Alok Soni, Vijay Sundaram, Young Kyong Jo, and Chien-Fan Chen for their support in conducting my experiments and providing valuable suggestions.

I would like to acknowledge the facilities available at Texas A&M University, especially the Material Characterization Facility, Microscopy & Imaging center, Center for Nanoscale Science & Technology and Texas A&M supercomputing facilities which facilitated my research.

Finally, I would like to thank my husband Cong Gu, who has offered unwavering support and encouragement during my Ph.D., and my parents, who have provided me with the best education they could from my childhood and continues to support me through my life.

CONTRIBUTORS AND FUNDING SOURCES

This work was supervised by a dissertation committee consisting of Dr. Sy-Bor Wen, Dr. Banerjee, and Dr. Staack in the Department of Mechanical Engineering and Dr. Hemmer of the Department of Electrical & Computer Engineering.

All work for the dissertation was completed independently by the student.

This research work was made possible in part by the National Science Foundation under NSF CBET-0845794 CAREER: Experimental and Theoretical Analysis for Optical Induced Thermal Energy Transport in Nano-Optical Systems with Pulsed Light Sources.

NOMENCLATURE

SPH	Smoothed Particle Hydrodynamics
LIEB	Laser Induced Explosive Boiling
CSPH	Compressible Smoothed Particle Hydrodynamics
ISPH	Incompressible Smoothed Particle Hydrodynamics
W	Smoothing function
W_{ij}	Smoothing function value between particle i and j
$\vec{r}_i$	Position vector of particle i
$\vec{r}_{ij}$	Distance vector between particle i and j
p	Pressure
h	Smoothing length of smoothing function
T	Temperature
m_i	Mass of particle i
ρ	Density
$\vec{v}$	Velocity
$\nabla_i W_{ij}$	Gradient of smoothing function evaluated at particle i
υ	Kinetic viscosity
μ	Dynamic viscosity
$\underset{\tau}{\Rightarrow}$	Stress applied to the mass
q	Heat flux

k	Heat conductivity
U	Internal energy
V_i	Volume of particle i
Re	Reynolds number
Ra	Rayleigh number
Pr	Prandtl number
β	Thermal expansion coefficient
α	Thermal diffusivity
σ	Surface tension
Fr	Froude number (speed-length ratio)
We	Weber number (fluid's inertia compared to surface tension)

TABLE OF CONTENTS

Page

LIST OF FIGURES

Page

LIST OF TABLES

Page

1. INTRODUCTION

1.1 Laser Induced Explosive Boiling (LIEB)

Interaction of laser beam with a solid surface can generate highly localized heating which can induce rapid phase change of adjacent liquid. This phenomenon is called laser induced explosive boiling (LIEB) of the liquid. Compared with traditional boiling process mainly driven by electronic heaters, LIEB can easily provide very short pulsed heating in miniature areas without relying on pre-installed heating element. For example, traditional electric heated and associated boiling process is limited by RC constant of the electric circuit and has difficulty to achieve less than ~100 100 ns pulsed heating. On the other hand, LIEB can be induced in a pulse with a duration as short as few femtoseconds when fs laser with high laser energy. In addition, with the possibility to confine laser light to a ~100s nm^2 spot, LIEB can be easily induced within <1 μm^2 area, which is also difficult to be achieved an electronic heater.

As a short summary, LIEB has several advantages over traditional electronic heating during a boiling process. First, LIEB can be much faster (nanosecond or femtosecond) than the boiling induced by electronic devices. The fast response of LIEB can reduce the amount of unwanted energy dissipate into surrounding to limit the heat affected zone as well as the associated thermal damage of the surrounding. Second, LIEB requires few to no preparation of the target surface for a boiling process. LIEB only requires controlled laser beam to be delivered to the solid surface/liquid domain where microscale boiling is desired. With these very short heating time and very confined heating

areas, “explosive” boiling process can occur during LIEB, which can be very different from traditional slower and larger area boiling process induced by electronic heater and has a potential to drive the fluid very far away from thermal equilibrium (e.g., superheated liquid states) during the explosive boiling. The highly transient superheated fluid/vapor bubble from LIEB can provide extremely high vapor pressure (MPa or above) within a sub-μm domain, which can be applied as a high intensity pulsed force source for different micro-electrical-mechanical devices (MEMS) [1, 2].

One important application of LIEB is in the bio-medicals[3, 4]. With the extremely high pressure in a very confined area, the vapor bubble from LIEB can provide enough stress to dissect bio-tissue with μm precision. For example, LIEB with excimer laser is commonly used in laser-assisted in situ keratomileusis (LASIK) [4] to precisely sculpt the cornea to correct vision deficiencies. With many important applications in the micro/nano fields, LIEB have received a significant attention from the development of the pulse laser (i.e., late 1980s). To understand the LIEB process in order to better control it in these numerous applications, experimental analyses for LIEB have been conducted by many different groups in the recent two decades[5-9]. At the same time, numerical simulation of this rapid boiling process induced by pulsed laser heating on the solid surface. Most of the theoretical analysis select meshfree method for this fast response boiling process induced by high energy pulsed laser due to its characteristics which will be discussed next section.

1.2 Meshfree Simulation

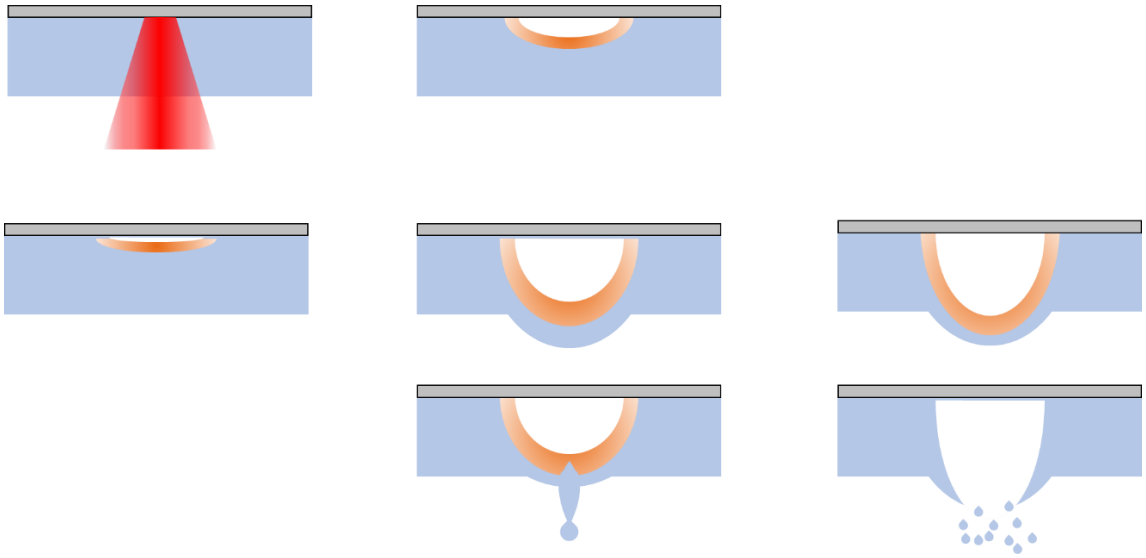

Figure 1 Schematic of laser induced boiling and liquid ejections

Figure 1 shows an example of pulsed laser induced boiling of liquid, bubble formation on top of solid surface, and 3 types of bubble collapse. Different level of laser energy will induce different phenomena. In this example LIEB includes multiple physics such as light absorption, joule heating, heat diffusion and phase change inside the target and stress formation and elastic wave propagation in the fluid domain. Therefore, the corresponding theoretical analysis for LIEB should be able to capture these main characteristics. To handle these physical processes in order to characterize an LIEB, the analysis should consider: (1) interfaces between liquid domain and background gas (top surface of liquid film); (2) rapid expansion of vapor bubble inside a liquid domain; (3) transient phase change between liquid and vapor under intense laser induced joule heating.

Traditional meshed analysis such as Finite-Difference-Method and Finite-Element-Method have difficulties in tracing the free surface and the interface between the vapor/liquid with high spatial resolution. Finite-Volume-Method (FVM), on the other hand, can deal moving boundaries and free surface more efficient. However, as a standard meshed method, FVM is also limited in mesh generation when simulation domain includes large distortion, moving interface, deformable boundaries, and free surface [10]. All these features are there in the LIEB example shown in Figure 1. Therefore, most studies of LIEB focus on meshfree methods in the theoretical analysis. Molecular dynamics (MD) model may be the most commonly adopted meshfree method that has been applied in studying the dynamics of LIEB (e.g., molecular-level modeling of early stages of LIEB and nano-bubble generation was done by E. Leveugle et al. [11] in 2007). Due to the time consuming N-body simulation in MD, it is challenging to apply MD in a domain large than ~100 nm with a simulation time longer than 10s ns. Since LIEB has a characteristic size more than a few microns and can last for more than a few ns, a macroscale meshfree method by solving macroscale continuous equations will be required in this study. Compared with microscale meshed methods, macroscale meshfree methods uses a set of free moving nodes (or "particles") to record the physical values as well as to solve the governing equations for mass, momentum and energy conservations in partial differential or integral format [12]. Among the available macroscale meshfree methods, smoothed particle hydrodynamics (SPH) has been developed for more than 30 years and is well-adopted in astrophysics and geophysics. Therefore, SPH is selected as the starting point of macroscale meshfree method of this study to understand the dynamics of LIEB with different laser

conditions. Description of traditional SPH as well as its limitations which should be handled before studying the LIEB are described in the following sections.

1.3 Smoothed Particle Hydrodynamics (SPH)

Smoothed Particle Hydrodynamics (SPH) was proposed by Lucy [13], Gingold and Monaghan in 1977 [14]. SPH divide a simulation domain into a set of particles and the physical properties at each location of the simulation domain are interpolated from their values recorded in the set of particles during the simulation. The set of particles keep adjusting their positions to better fit the geometry of the simulation domain. Thus, SPH can handle the interface intrinsically through having the particles tracking the exact locations of the moving interface/boundary and free surface. With these characteristics, SPH can handle a simulation domain with large deformation or the occurrence of discontinuities during the simulation (as Figure 2).

Traditional SPH is limited by its algorithm using artificial sound of speed and viscosity in fluid simulation as well as energy transport analysis. Therefore, simulation results need to be verified with either experimental results or other CFD analysis results when different artificial values are applied during calculation. Non-physical properties used can be verified for only limited amount of cases. For most simulation conditions, such as LIEB, we can find neither experimental results nor reliable computing analysis. Therefore, meshfree algorithm using real physical properties is required and we present our new algorithm which can handle fluid and energy transport using physical properties of fluid in Section 3 and 4.

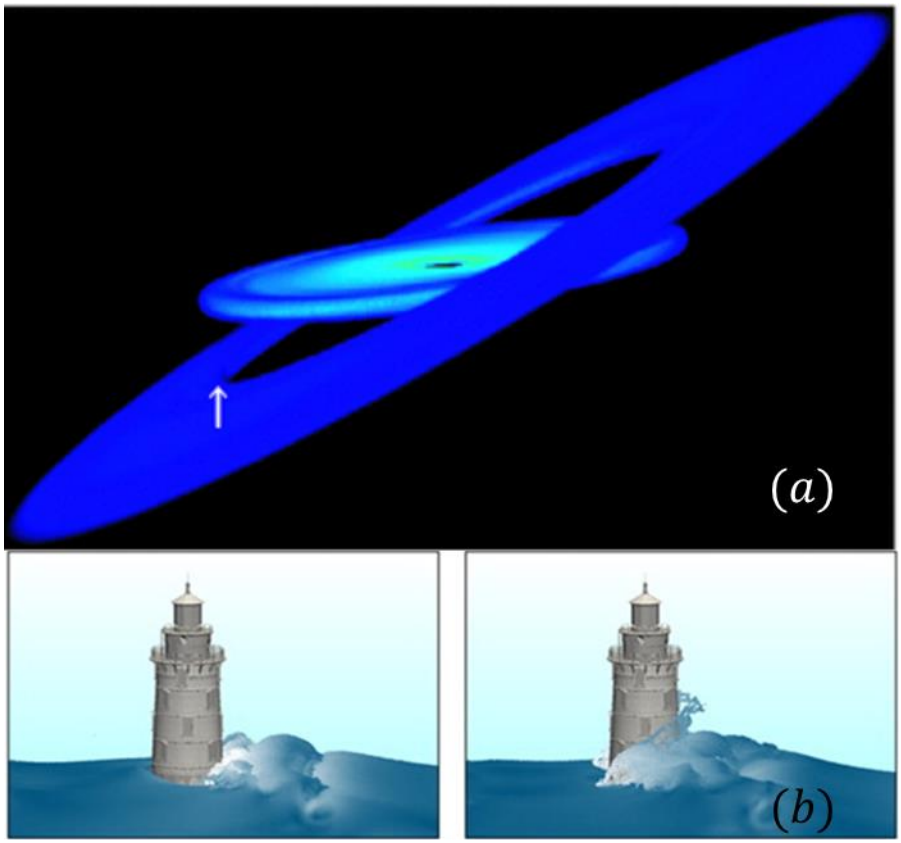

Figure 2 SPH applications: (a) calculation of warp propagation in astrophysical accretion disc (reprinted with permission from [15]); (b) wave impact on a lighthouse at t=13 s and 15 s (reprinted with permission from [16]).

1.4 Scope of the Dissertation

This dissertation starts with a detailed introduction and literature review of Smoothed Particle Hydrodynamics in next section. The introduction includes basics of SPH approximation of field variables and its derivatives in 2.3, SPH formulas of Naiver-Stocks Equations in 2.4, Boundary Conditions and numerical algorithm adopted in 2.5 and 2.6. Last part of Section 2 is the review of fluid and energy transport studies using SPH and their limitations in 2.7 and 2.8. Following that, Section 3 shows the usage of traditional SPH in simulating free convection problems with significantly change of fluid density.

Applied governing equations are discussed in 0, boundary conditions in 3.2, and numerical scheme in 3.3. Numerical tests results are presented and discussed in 3.4. Section 4 starts with the discussion of convergence problems and accuracy of derivatives in traditional SPH. Based on the results in Section 3, we noticed that traditional SPH cannot handle weakly compressible fluid with large sound speed (e.g., water). However, most of the LIEB experiments and applications are in aqueous conditions. Therefore, in Section 4 we presented our new high accuracy method, the new first and second derivatives formulas and derivations are presented in 4.1. By adopting this new algorithm, test cases and their results are shown in 4.3.

Section 5 illustrates laser induced liquid ejection, which can be another potential application of LIEB in engineering. Application of LIEB in inkjet and current inkjet technologies are discussed in 5.1 and 5.2. New non-contact laser induced droplet ejection system was presented in 5.4 and 5.5 including fabrication procedure of nozzle and experimental setup. The test results using multiple laser light durations and energy are shown in 5.6. The last section is the conclusion of this study and possible extension of this research.

2. REVIEW OF SMOOTHED PARTICLE HYDRODYNAMICS

2.1. Numerical Approximation for Fluid Problems

Fluid problems are generally described by fundamental governing equations of fluid-the mass, momentum and energy. These equations represent fundamental principles of physics using mathematics. There are various ways to represent the fluid problems, and most of them use partial differential equations (PDEs) to describe fluid properties over the entire fluid domain also as a function of time. To illustrate the physical phenomena such as fluid motion and heat diffusion, solutions of governing equations (mostly PDEs) are required. However, pure analytical solutions can be found only in few fluid problems with certain boundary conditions and boundary conditions. In recent decades, numerical methods have been adopted to approximate solutions of fluid problems in most engineering. The key of numerical methods is the discretization of fluid domain into a set of sub-system with known property distributions inside each sub-system. Therefore, with given initial property assignment, derivatives of physical properties are able to be approximated by algebra formulas between sub-systems close to each other. Finally, PDEs can be reduced into sets of algebra equations for each sub-system.

Based on the way to find sub-system close to each other in order to obtain accurate derivative values, numerical methods are divided into two groups: meshed methods and meshfree methods (as Figure 3). For meshed methods, each sub-system is connected with others, therefore derivatives of physical properties can be easily calculated from connected neighbor sub-systems using algebra formulas. On the other hand, meshfree methods

doesn’t connect with each other so that they are not able to find the left/right/top/bottom sub-system directly. Therefore, in order to find neighborhoods meshfree methods need to search within certain distance from the center of the sub-system and use all detected sub-systems inside this search range for derivative approximation. Also, there are different ways to represent physical properties inside each sub-system and approximate derivative between sub-systems. For example, distribution of physical properties inside each sub-system can be represented as flat planes, planes fit in certain ordinary differential equations (ODEs), or planes satisfying given surface integral.

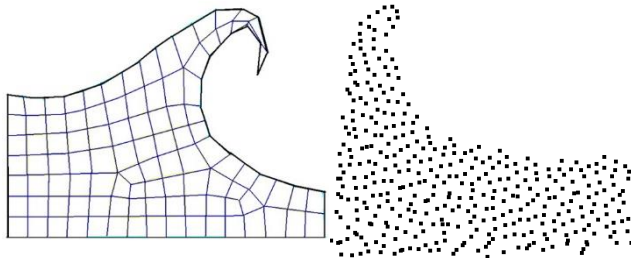

Figure 3 Representation of a wave using mesh and meshfree methods

For example, finite difference method (FDM) is a popular to approximate derivatives by using difference equations between connected sub-systems. Physical properties are usually stored at the vertices between connected sub-systems, and can be used to estimate first order derivatives (the slop of physical properties inside this sub-system) by various types of difference equations (e.g., forward, backward, and central difference formulas). Finite element method (FEM), another wildly used mesh method also divided the entire domain into sub-systems and the governing equations can be

approximated by polynomial or other types of approximation inside each sub-system (also named element in FEM). For example, N. Sukumar and E.A. Malsch [17] discussed FEM approximation using polynomial functions and Figure 4 below shows the reconstructed property field using FEM.

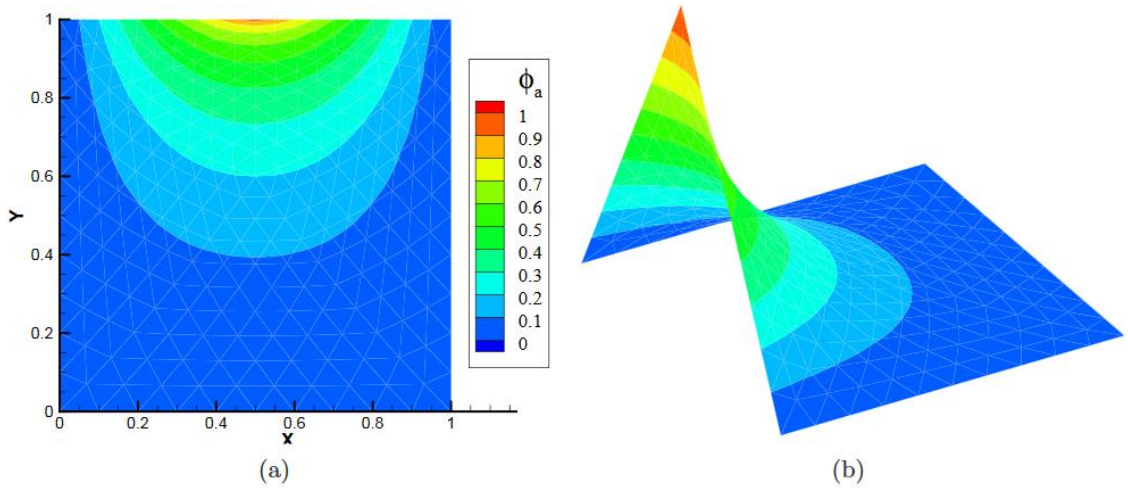

Figure 4 Finite element method using polynomial function as shape function inside elements

Another mesh method wildly used in Computational Fluid Dynamics is Finite Volume Method (FVM) which approximate function inside sub-system (named controlled volume in FVM method) with a constrain of divergence term converted to surface integral. The surface integral form the conservation law for each small sub-system and can recover the global conservation of fluid system.

Similar to mesh method, meshfree free method also need to approximated governing equations within sub-system by different ways in order to compute derivatives and further integral over the entire domain. SPH method as a wildly used meshfree

method, the most traditional way to approximate derivatives is quite similar to finite difference method which linearize based on vertices values of each sub-system. We will discuss the discretization and approximation method of traditional SPH method in following sections.

2.2. Background of SPH

As discussed in 1.2 and 1.3, meshfree methods use arbitrary beads/particles distributed over entire domain instead of a mesh system to generate numerical results of conservation equation in integral or PDE formats with different boundary conditions. Smoothed Particle Hydrodynamics (SPH) is a 'truly' meshfree methods which represents the entire system is represented with sets of particles and each particle obtain its physical/chemical properties. These particles interact with neighboring particles within a predefined cut-off radius. In order to determine the evolution of fluid properties at each simulated particle positions, governing equations of SPH are discretized following these distributed particles, which is name SPH approximations.

As a typical Lagrangian methods, SPH satisfy exact mass conservation automatically since the number of the simulation particles are fixed. Since the size/shape of the entire system are determined by the locations of the SPH particles, no explicit traces are needed to define material interface, free surface, or moving boundaries during SPH simulations. This 'natural' tracking of interface and moving boundaries is not affected by the complexity of the geometry of the simulation domain. Another benefit of SPH is a straightforward handling of large deformation in the solid or

fluid domains without ceaseless reconstruction of grid/mesh at the expense of heavy computing load and a high risk of numerical instability.

2.3. SPH Approximation

The basis of SPH relying on representing value a physical quantity ϕ at arbitrary location $\vec{r}_i$ with kernel integration (or weighted integration) and the followed summation approximation for this kernel integration.

2.3.1. Kernel Integration Approximation

In kernel approximation step, the estimated value of quantity ϕ is derived from a smoothing function W (also named kernel/weight functions) which has a maximum value at the center and attenuated to zero outside of a specified cut-off radius. With the kernel approximation $\langle \phi \rangle$ can be written as:

$$\langle \phi \rangle = \int_{\Omega} \phi(\vec{r}') W(\vec{r} - \vec{r}', h) d\vec{r}' \qquad \textbf{Equation 1}$$

where $2h$ is the smoothing length, also named cut off radius, which determines the supporting radius of the smoothing function W. Usually, the smoothing function is an even function although it is not strictly enforced in most cases. Choosing even function as smoothing function means center particle obtains symmetric influence from surrounding particles.

In our study, we used a common format (i.e., Wendland format) of the weight function W as Eq.2.

$$W\left(\vec{r},h\right)=\alpha_D\left(1-\frac{s}{2}\right)^4\left(2s+1\right)\quad 0\le s\le 2$$ **Equation 2**

where $\vec{r}$ and $2h$ are the position of particle and cut off radius of the weight function, and α_D equals $7/\left(4\pi h^2\right)$ in 2D and $21/\left(16\pi h^2\right)$ in 3D, and $s=\left(r_i-r_j\right)/h$.

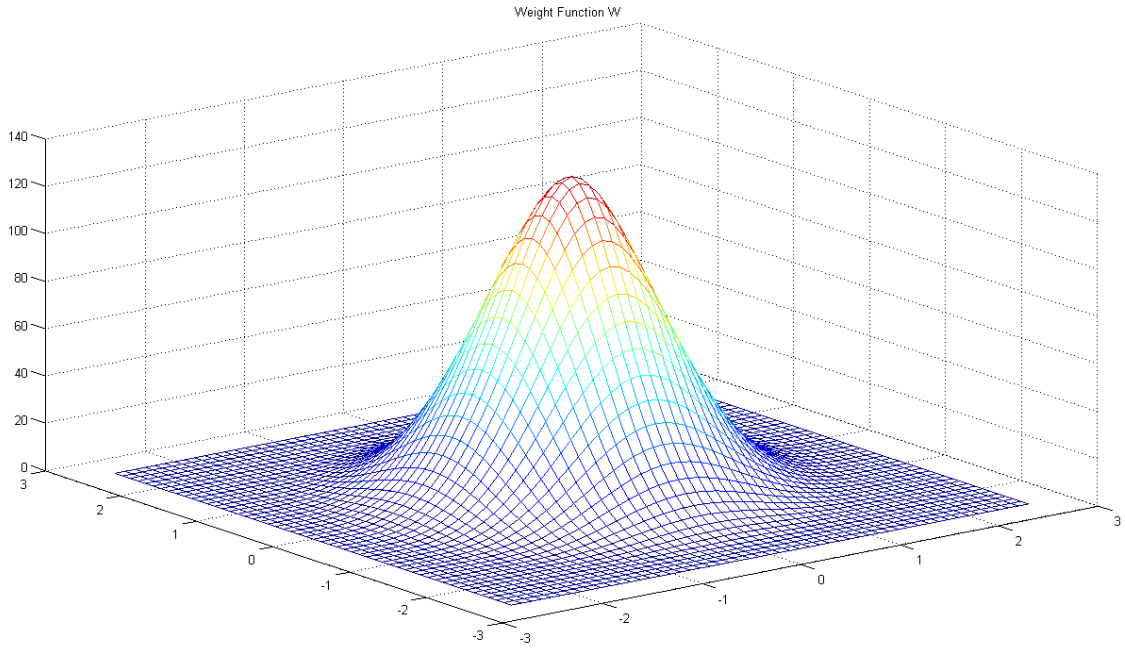

Figure 5 Wendland smoothing function without dimensional factor

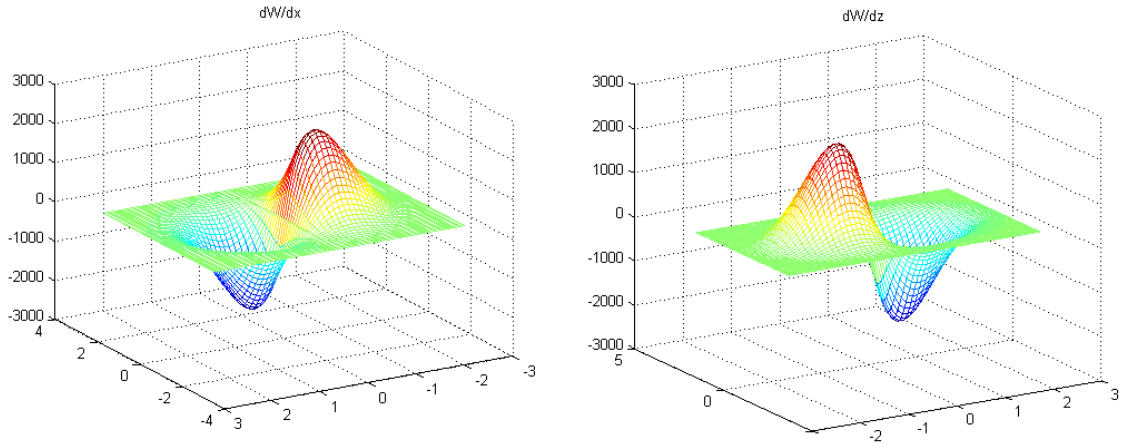

Figure 6 Gradient of wendland smoothing function without dimensional factor

Figure 5 and Figure 6 shows the value of weight function and the gradient in a 2D domain. The Wendland weight function has been verified as a computational efficient and stable weight function in 2D and 3D SPH [18, 19]. In [20-22], the kernel approximation is claimed to have second order accuracy.

2.3.2. Particle Approximation

The second step for the SPH approximation is particle approximation which means the value of central particle is approximated by the summation of values sitting within it supporting area of smoothing function. In SPH, computing domain is discretized into a set of particles with initial location and property information (see Figure 7 for illustration of 2D case).

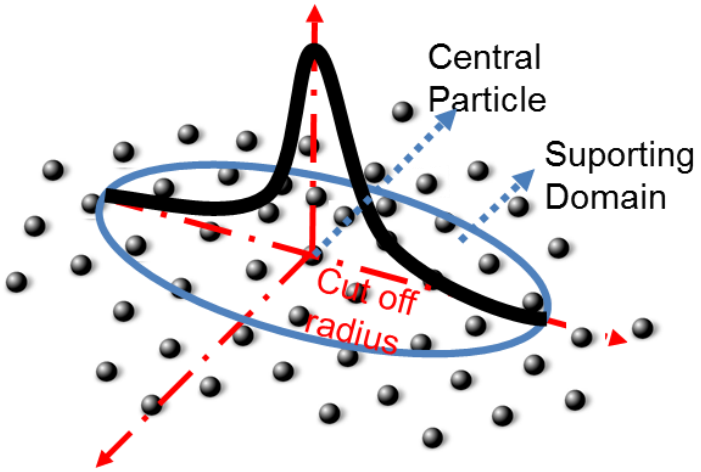

Figure 7 SPH particle approximation in a 2D case

The local field quantity ϕ (e.g., T and P) at location i (e.g., the location of the i^{th} particle) of the simulation domain is evaluated from a spatial average of the field values stored in the neighboring j particles with smoothing function [20]. Figure 8 represents the SPH approximation of a constant physical property in 1D case.

$$\phi_i = \int \phi(r_i) W_{ij}(r_i - r', h)\, dr' \cong \sum_j m_j \frac{\phi_j}{\rho_j} W_{ij}(r_i - r_j, h) \qquad \textbf{Equation 3}$$

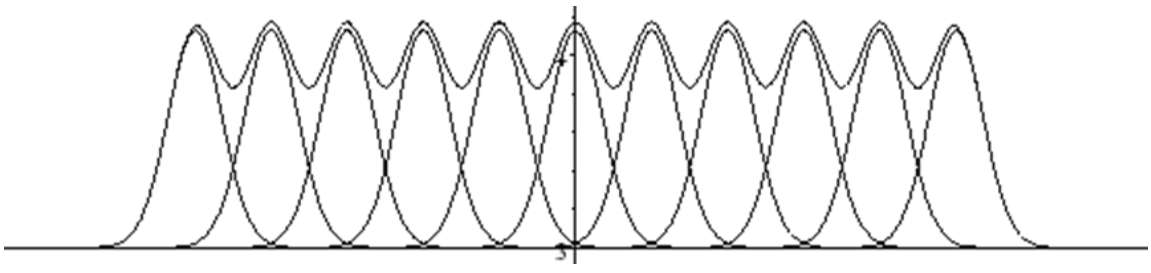

Figure 8 1D SPH approximation of a constant physical property

2.3.3. First Derivatives

Various methods (as Table 1 shows) were proposed to calculate derivative of ϕ by differentiating Eq. 3 with different manipulations.

Table 1 Summary of current SPH methods for 1st derivative

	First Derivation
Standard Method	$\nabla\phi_i = \frac{1}{\Psi}\left(\nabla(\Psi\phi) - \phi\nabla\Psi\right) = \frac{1}{\Psi_i}\sum_j m_j \frac{\Psi_j}{\rho_j}\left(\phi_j - \phi_i\right)\nabla_i W_{ij}$
Linear Exact Method	$\nabla_i^l\phi = \mathrm{M}^{ln} J_\phi^n$ $\mathrm{M}^{ln} = \left(\sum_j \frac{m_j}{\rho_j}\left(\vec{r}_j - \vec{r}_i\right)^l \nabla_i^n W_{ij}\right)^{-1}$ $J_\phi^n = \sum_j \frac{m_j}{\rho_j}\left(\phi_j - \phi_i\right)\nabla_i^n W_{ij}$
Integral Approximation	$\begin{bmatrix} \frac{\partial\phi}{\partial x_1} \\ \frac{\partial\phi}{\partial x_2} \\ \frac{\partial\phi}{\partial x_3} \end{bmatrix} = \begin{bmatrix} \tau_{11} & \tau_{12} & \tau_{13} \\ \tau_{21} & \tau_{22} & \tau_{23} \\ \tau_{31} & \tau_{32} & \tau_{33} \end{bmatrix}^{-1} \begin{bmatrix} I_1 \\ I_2 \\ I_3 \end{bmatrix}$ $\tau_{ij} = \int\left(x_i' - x_i\right)\left(x_j' - x_j\right)W_{ij}d\vec{r}$ $I_i = \int\left[\phi(\vec{r}') - \phi(\vec{r})\right]\left(x_i' - x_i\right)W_{ij}d\vec{r}$ $i, j = 1,3$

2.3.3.a. Standard Method

From SPH kernel approximation and particle approximation, the standard procedure for derivative of function ϕ can be written as Eq. 4 which is an exact derivative of Eq. 3 [21]. This derivative result cannot vanish if function ϕ is a constant and if the particle distribution is not perfectly symmetric.

$$\nabla\phi_i = \sum_j m_j \frac{\phi_j}{\rho_j}\nabla W_{ij}\left(r_i - r_j, h\right) \qquad \textbf{Equation 4}$$

Monaghan proposed an alternative way to calculate $\nabla\phi_i$ as

$$\nabla \phi_i = \frac{1}{\Psi}\left(\nabla\left(\Psi \phi\right) - \phi \nabla \Psi\right) = \frac{1}{\Psi_i}\sum_j m_j \frac{\Psi_j}{\rho_j}\left(\phi_j - \phi_i\right)\nabla_i W_{ij} \qquad \textbf{Equation 5}$$

where Ψ is any differentiable function. This form of derivative vanish when ϕ is a constant even when center particle is surrounded by random distributed particles. Different SPH formulas can be derived by choosing different Ψ functions. For example,

Eq. 6 can be derived if $\Psi = 1$ and Eq. 7 if $\Psi = \rho$.

$$\nabla \phi_i = \sum_j \frac{m_j}{\rho_j}\left(\phi_j - \phi_i\right)\nabla_i W_{ij} \qquad \textbf{Equation 6}$$

$$\nabla \phi_i = \frac{1}{\rho_i}\sum_j m_j \left(\phi_j - \phi_i\right)\nabla_i W_{ij} \qquad \textbf{Equation 7}$$

With these two equations, mass conservation of fluid (Eq. 24) can be expressed as following 2 different formats.

$$\frac{d\rho_i}{dt}_i = -\rho_i \sum_j \frac{m_j}{\rho_j}\left(v_j - v_i\right)\nabla_i W_{ij} \qquad \textbf{Equation 8}$$

$$\frac{d\rho_i}{dt}_i = -\sum_j m_j \left(v_j - v_i\right)\nabla_i W_{ij} \qquad \textbf{Equation 9}$$

By comparing these two formulas, we can find that Eq. 8 involves ρ in the summation. They can both vanish to zero when center fluid particle is surrounded by random distributed particles if velocity is constant. However, if the computational domain is made up with two or more fluid with different density ration (for example liquid-gas interface), Eq. 8 can provide more accurate and stable result [23]. It turned out that both equations can be applied when density ratio is less than two, but Eq. 8 can be better choice if density ratio larger than two.

One of the main drawback for the standard gradient formula is it low accuracy and high sensitivity of distribution of surrounding particles [24]. Therefore, other higher order accuracy gradient formulas were proposed. The following described 2 higher accuracy methods proposed recently.

2.3.3.b. Linear-Exact Method

In 2004, Price and Monaghan [25] improved standard first order derivative by expanding the summation terms on the right hand side of Eq. 6 or Eq.7, named Linear-Exact (LE), which provides:

$$\sum_j \frac{m_j}{\rho_j}\phi_j \nabla_i W_{ij} = \sum_j \frac{m_j}{\rho_j}\left\{\phi_i + \left(\vec{r}_j - \vec{r}_i\right)\cdot\nabla_i\phi + \ldots\right\}\nabla_i W_{ij} \qquad \textbf{Equation 10}$$

Then, rearrange the equation and get:

$\sum_j \frac{m_j}{\rho_j}\left(\phi_j - \phi_i\right)\nabla_i^n W_{ij} = \nabla_i^l \phi \sum_j \frac{m_j}{\rho_j}\left(\vec{r}_j - \vec{r}_i\right)\nabla_i^n W_{ij}$. In this discussion, we use upper indices (l, m, n) refer to spatial directions, and lower indices refer to the particles. The linear exact gradient estimation can be obtained by matrix inversion as:

$$\nabla_i^l \phi = \mathrm{M}^{ln} J_\phi^n \qquad \textbf{Equation 11}$$

where $\mathrm{M}^{ln} = \left(\sum_j \frac{m_j}{\rho_j}\left(\vec{r}_j - \vec{r}_i\right)^l \nabla_i^n W_{ij}\right)^{-1}$ and $J_\phi^n = \sum_j \frac{m_j}{\rho_j}\left(\phi_j - \phi_i\right)\nabla_i^n W_{ij}$.

2.3.3.c. Integral Approximation Method

Another different way to estimate first order derivative is inspired by the second order derivative approximation from Brookshaw [26], name Integral Approximation (IA).

This new expression was proposed by Garvia-Senz etc. [27] using an integral expression defined as:

$$I(\vec{r}) = \int_{\Omega} \left[\phi(\vec{r}') - \phi(\vec{r})\right](\vec{r}' - \vec{r}) W(\vec{r}' - \vec{r}, h)\, d\vec{r}' \qquad \textbf{Equation 12}$$

Expanding $\left[\phi(\vec{r}') - \phi(\vec{r})\right]$ to the first order and gives $\nabla\phi \cdot (\vec{r}' - \vec{r}) + O(\Delta x^2)$. For 3D case, $\vec{r}' - \vec{r} = (x_1' - x_1)\vec{i} + (x_2' - x_2)\vec{j} + (x_3' - x_3)\vec{k}$. Then rewrite integral expression as:

$$\begin{bmatrix} \frac{\partial \phi}{\partial x_1} \\ \frac{\partial \phi}{\partial x_2} \\ \frac{\partial \phi}{\partial x_3} \end{bmatrix} = \begin{bmatrix} \tau_{11} & \tau_{12} & \tau_{13} \\ \tau_{21} & \tau_{22} & \tau_{23} \\ \tau_{31} & \tau_{32} & \tau_{33} \end{bmatrix}^{-1} \begin{bmatrix} I_1 \\ I_2 \\ I_3 \end{bmatrix} = \begin{bmatrix} c_{11} & c_{12} & c_{13} \\ c_{21} & c_{22} & c_{23} \\ c_{31} & c_{32} & c_{33} \end{bmatrix} \begin{bmatrix} I_1 \\ I_2 \\ I_3 \end{bmatrix} \qquad \textbf{Equation 13}$$

where, $\tau_{ij} = \int (x_i' - x_i)(x_j' - x_j) W_{ij} d\vec{r}$; $i, j = 1, 3$ and $I_i = \int \left[\phi(\vec{r}') - \phi(\vec{r})\right](x_i' - x_i) W_{ij} d\vec{r}$; $i = 1, 3$. Value of the gradient can be calculated by solving Eq. 13. This approximation provides an antisymmetric gradient estimation which can ensure the exact conservation although it breaks the exactness of gradient of linear functions.

Both Integral Approximation and Linear Exact approximation of first derivative obtains a one order higher accuracy than standard approximation [24] in both symmetrically or randomly distributed particles in 2D domain calculation.

2.3.4. Second Derivatives

The thermal diffusion in energy conservation equation and viscous force term in momentum equations require the second order derivatives of physical properties over fluid domain. Therefore, to find numerical solutions of fluid problems, approximation formulas

for second derivatives of physical properties are required. Four different ways to approximate second derivative using SPH method are discussed below.

2.3.4.a. Standard Method

Similar to the first derivative, standard SPH formula of second derivatives can be derived by differentiating Eq. 3 twice as:

$$\left(\nabla^2 \phi\right)_i = \sum_j m_j \phi_j \nabla_i^2 W_{ij} \qquad \textbf{Equation 14}$$

As shown in Figure 3, the reconstructed surface with SPH method will have the wavy pattern which will induce small error in first derivative but tremendous errors when this wavy patter is used for second derivative calculation. However, this formula can induce dramatic increase of error. Also, the second order derivative of smoothing function can have both positive and negative value depending on the distance away from central particle. This change of sign can induce non-physical results in the calculation. Another drawback of applying this formula is non-convergence of properties inside a confined domain. To obtain a higher accuracy in second derivative in SPH simulation, various expressions have been proposed and verified in recent decades.

2.3.4.b. Integral Approximation Method

In 1985, Brookshaw [26] proposed an expression derived from an integral approximation starting with 1D case:

$$\int \frac{\phi(x') - \phi(x)}{x' - x} \frac{\partial W(x' - x, h)}{\partial x} dx' = \frac{1}{2} \frac{d^2 \phi}{dx^2} + O\left(h^2\right) \qquad \textbf{Equation 15}$$

where W is the smoothing function satisfying general requirement $\int W = 1$. Thus, we are able to get following expression:

$$\left(\frac{d^2\phi}{dx^2} \right)_i = 2\sum_j \frac{m_j}{\rho_j} \frac{\left(\phi_i - \phi_j\right)}{x_i - x_j} \frac{\partial W_{ij}}{\partial x_i} + \mathrm{O}\left(h^2\right) \qquad \textbf{Equation 16}$$

The high accuracy described here only happen when surrounding fluid particles are located exactly symmetric. This formula can be extended in 2D and 3D cases, and they are commonly applied in SPH calculation of viscous force and heat dissipation. Compared with Eq. 14, Eq. 16 will not change the sign at various distance from central particle which provides physical dissipation direction during calculation. Eq. 16 can satisfy general requirement of traditional SPH calculation for highly compressible fluids.

2.3.4.c. Higher Order Laplacian and Corrected Higher Order Laplacian Method

Higher order accuracy expressions of second derivative (especially for Laplacian) have been proposed in order to solve pressure Poisson equation in projection-based fluid dynamics computing (check whether it is valid for compressible flow). For example, Khayyer and Gotoh [28, 29] improved Laplacian formula for further stabilization of pressure calculation (Higher order Laplacian method).

The Laplacian at central particle can be expressed as the divergence of gradient at the central particle:

$$\left\langle \nabla^2 \phi \right\rangle_i = \nabla \cdot \left\langle \nabla \phi \right\rangle_i \qquad \textbf{Equation 17}$$

The gradient calculation at central particle can be written in various ways as discussion before. Here, if standard SPH formula $\left\langle \nabla \phi \right\rangle_i = \sum_j \left(\phi_j - \phi_i\right) \nabla W_{ij}$ was applied, the Laplacian at central particle can be written as:

$$\nabla \cdot \left\langle \nabla \phi \right\rangle_i = \sum_j \left(\nabla \phi_{ij} \cdot \nabla W_{ij} + \phi_{ij} \nabla^2 W_{ij} \right) \qquad \textbf{Equation 18}$$

where $\phi_{ij} = \phi_j - \phi_i$. In 2D coordinates, $\nabla \phi_{ij}$ and ∇W_{ij} can be expressed as:

$$\nabla \phi_{ij} = \frac{\partial \phi_{ij}}{\partial r_{ij}} \frac{\partial r_{ij}}{\partial x_{ij}} \vec{i} + \frac{\partial \phi_{ij}}{\partial r_{ij}} \frac{\partial r_{ij}}{\partial y_{ij}} \vec{j} = \nabla \phi_j - \nabla \phi_i$$
$$\nabla W_{ij} = \frac{\partial W_{ij}}{\partial r_{ij}} \frac{\partial r_{ij}}{\partial x_{ij}} \vec{i} + \frac{\partial W_{ij}}{\partial r_{ij}} \frac{\partial r_{ij}}{\partial y_{ij}} \vec{j} \qquad \textbf{Equation 19}$$

Then,

$$\nabla \phi_{ij} \cdot \nabla W_{ij} = \frac{\partial \phi_{ij}}{\partial r_{ij}} \frac{\partial W_{ij}}{\partial r_{ij}}$$
$$\nabla^2 W_{ij} = \frac{\partial^2 W_{ij}}{\partial^2 r_{ij}} + \frac{1}{r_{ij}} \frac{\partial W_{ij}}{\partial r_{ij}} \qquad \textbf{Equation 20}$$

Substitute these two equations into Laplacian formula:

$$\nabla \cdot \left\langle \nabla \phi \right\rangle_i = \sum_j \left(\phi_{ij} \frac{\partial^2 W_{ij}}{\partial r_{ij}^2} - \frac{\phi_{ij}}{r_{ij}} \frac{\partial W_{ij}}{\partial r_{ij}} \right) \qquad \textbf{Equation 21}$$

Although higher order Laplacian formula provides enhanced pressure calculation, reduces numerical oscillations during simulation, it still has issue of inconsistency [30]. This formula will result in inaccuracy with lack of a compact supporting domain (for example free surface) [31]. The supporting domain in this study is determined as the domain within cut-off radius of each center particle.

Another Corrected Higher order Laplacian method was proposed [31] with a basis on Linear Exact method for first derivative (discussed in previous section). Follow the similar procedure, Laplacian expression can be rewritten as:

$$\left\langle \nabla^2 \phi \right\rangle_i = \sum_j \left(\nabla_{ij} \phi_{ij} \cdot C_i \nabla_{ij} W_{ij} + \phi_{ij} \nabla_{ij} \cdot \left(C_i \nabla_{ij} W_{ij} \right) \right) \qquad \textbf{Equation 22}$$

where $\nabla_{ij} = \left(\frac{\partial}{\partial x_{ij}}, \frac{\partial}{\partial y_{ij}} \right), \nabla_i = \left(\frac{\partial}{\partial x_i}, \frac{\partial}{\partial y_i} \right)$, and $C_i = \begin{bmatrix} -\sum_j \frac{\partial W}{\partial r} \frac{x_{ij}^2}{|r_{ij}|} & -\sum_j \frac{\partial W}{\partial r} \frac{x_{ij} y_{ij}}{|r_{ij}|} \\ -\sum_j \frac{\partial W}{\partial r} \frac{x_{ij} y_{ij}}{|r_{ij}|} & -\sum_j \frac{\partial W}{\partial r} \frac{y_{ij}^2}{|r_{ij}|} \end{bmatrix}^{-1}$.

Then, the final expression of this Corrected Higher Order Laplacian methods can be derived following the same procedure. This method guarantees the first order accuracy even with randomly distributed particles.

2.3.4.d. Integral Approximation of First Derivative

Another route to calculate the second derivative can be derived directly from first derivative formula. The Integral Approximation method of first derivative can be applied to calculate $\nabla \phi = \frac{\partial \phi}{\partial x_1} \vec{i} + \frac{\partial \phi}{\partial x_2} \vec{j} + \frac{\partial \phi}{\partial x_3} \vec{k}$ from Eq. 13 or 18. Then calculate divergence of $\nabla \phi$ using first derivative as following:

$$\begin{aligned} \nabla^2 \phi &= \frac{\partial^2 \phi}{\partial x_1^2} + \frac{\partial^2 \phi}{\partial x_2^2} + \frac{\partial^2 \phi}{\partial x_2^2} \\ &= c_{11} I_{1\nabla\phi} + c_{12} I_{2\nabla\phi} + c_{13} I_{3\nabla\phi} \\ &+ c_{21} I_{1\nabla\phi} + c_{22} I_{2\nabla\phi} + c_{23} I_{3\nabla\phi} \\ &+ c_{31} I_{1\nabla\phi} + c_{32} I_{2\nabla\phi} + c_{33} I_{3\nabla\phi} \end{aligned} \qquad \textbf{Equation 23}$$

where, $\left[c_{ij} \right] = \left[\tau_{ij} \right]^{-1} = \left[\int \left(x_i' - x_i \right) \left(x_j' - x_j \right) W_{ij} d\vec{r} \right]^{-1}$; $i, j = 1, 3$ and

$I_{i\nabla\phi} = \int \left[\nabla_i \phi \left(\vec{r}' \right) - \nabla_i \phi \left(\vec{r} \right) \right] \left(x_i' - x_i \right) W_{ij} d\vec{r}$; $i = 1, 3$.

These methods (c.f. Table 2) highly depend on the accuracy of first derivative method and geometry condition. It can provide reasonable high accuracy even with non-compact supporting domain as long as the adopted first derivative is accurate enough. This method also guarantees the first order accuracy even with randomly distributed particles.

Table 2 Summary of methods for 2nd derivation

	Second Derivation
Standard Method	$\left(\nabla^2\phi\right)_i = \sum_j m_j \phi_j \nabla_i^2 W_{ij}$
Integral Approximation	$\left(\frac{d^2\phi}{dx^2}\right)_i = 2\sum_j \frac{m_j}{\rho_j}\frac{\left(\phi_i-\phi_j\right)}{x_i-x_j}\frac{\partial W_{ij}}{\partial x_i}+\mathrm{O}\left(h^2\right)$
Higher order Laplacian and Corrected Higher order Laplacian Method	$\left\langle\nabla^2\phi\right\rangle_i = \sum_j\left(\nabla_{ij}\phi_{ij}\cdot C_i\nabla_{ij}W_{ij}+\phi_{ij}\nabla_{ij}\cdot\left(C_i\nabla_{ij}W_{ij}\right)\right)$ $\nabla_{ij}=\left(\frac{\partial}{\partial x_{ij}},\frac{\partial}{\partial y_{ij}}\right),\nabla_i=\left(\frac{\partial}{\partial x_i},\frac{\partial}{\partial y_i}\right)$ $\quad C_i=\begin{bmatrix}-\sum_j\frac{\partial W}{\partial r}\frac{x_{ij}^2}{\lvert r_{ij}\rvert} & -\sum_j\frac{\partial W}{\partial r}\frac{x_{ij}y_{ij}}{\lvert r_{ij}\rvert}\\ -\sum_j\frac{\partial W}{\partial r}\frac{x_{ij}y_{ij}}{\lvert r_{ij}\rvert} & -\sum_j\frac{\partial W}{\partial r}\frac{y_{ij}^2}{\lvert r_{ij}\rvert}\end{bmatrix}^{-1}$ $i,\ j=1,3$
Integral Approximation of First Derivative	$\nabla^2\phi=\frac{\partial^2\phi}{\partial x_1^2}+\frac{\partial^2\phi}{\partial x_2^2}+\frac{\partial^2\phi}{\partial x_2^2}$ $=c_{11}I_{1\nabla\phi}+c_{12}I_{2\nabla\phi}+c_{13}I_{3\nabla\phi}$ $+c_{21}I_{1\nabla\phi}+c_{22}I_{2\nabla\phi}+c_{23}I_{3\nabla\phi}$ $+c_{31}I_{1\nabla\phi}+c_{32}I_{2\nabla\phi}+c_{33}I_{3\nabla\phi}$	$\left[c_{ij}\right]=\left[\tau_{ij}\right]^{-1}=\left[\int\left(x_i'-x_i\right)\left(x_j'-x_j\right)W_{ij}d\vec{r}\right]^{-1}$ $I_{i\nabla\phi}=\int\left[\nabla_i\phi\left(\vec{r}'\right)-\nabla_i\phi\left(\vec{r}\right)\right]\left(x_i'-x_i\right)W_{ij}d\vec{r}$ $i,\ j=1,3$

2.4. Navier-Stokes (N-S) Equation for Compressible and Incompressible Flow

In the past decades, two typical SPH algorithms based on two groups of governing equations have been studied and adopted. One is Truly Incompressible SPH (ISPH), and another is Compressible SPH. The macroscale governing equations in Lagrangian

coordinates which can be used to determine the pressure, velocity, temperature and density fields both ISPH and CSPH are listed in Table 3 below.

Table 3 Governing equations of standard weakly compressible SPH and incompressible SPH

	Compressible SPH [32]	**Truly Incompressible SPH [32]**
Governing Equations	$\frac{1}{\rho}\frac{d\rho}{dt} + \nabla \cdot \vec{u} = 0$ $\frac{d\vec{u}}{dt} = -\frac{1}{\rho}\nabla p + \nabla \cdot (\nu \nabla \vec{u}) + \vec{F}$ $p = \frac{\rho_0 c_0^2}{\gamma}\left(\left(\frac{\rho}{\rho_0}\right)^{\gamma} - 1\right)$	$\nabla \cdot \vec{u} = 0$ $\frac{d\vec{u}}{dt} = -\frac{1}{\rho}\nabla p + \nabla \cdot (\nu \nabla \vec{u}) + \vec{F}$

Truly incompressible method applies incompressibility constrains (i.e. $\nabla \cdot \vec{u} = 0$) during simulation. Therefore, there is no need to worry about the highly nonlinear p vs ρ correlation during incompressible fluid simulation and is numerically stable. Compare with truly incompressible method, the highly nonlinear p vs ρ correlation used in compressible methods can easily induce numerical instability especially for large sound speed C_0. However, compared with compressible SPH, truly incompressible SPH has limitations in computational analysis and reasonable prediction of various fluid flow under different conditions. For examples, ISPH cannot be applied when phenomena of our interest involve with the compressibility of fluid (e.g., pressure wave, free convections,

and phase changes). Therefore, in this study, we mainly focused on compressible SPH with governing equations as:

$$\frac{d\rho}{dt} = -\rho \nabla \cdot v \qquad \textbf{Equation 24}$$

$$\rho \frac{dv}{dt} = -\nabla p + \rho g + \upsilon_0 \nabla^2 \vec{v} \qquad \textbf{Equation 25}$$

$$\rho \frac{DU}{Dt} = -\nabla \cdot q - p(\nabla \cdot v) - (\tau : \nabla v) \qquad \textbf{Equation 26}$$

where ρ , v , U and p are the density, velocity, internal energy and pressure of a controlled mass; g , υ_0 , and $\vec{\tau}$ are the gravitation acceleration, kinetic viscosity, and stress tensor applied to the controlled mass. The conductive heat flux q in Eq.26 can be determined with Fourier's law as

$$q = -k \nabla T \qquad \textbf{Equation 27}$$

where T and k are the local temperature and heat conductivity of the controlled mass.

Substituting SPH approximations for first and second order derivatives in Eq. 24-26, we can have SPH formulations of Navier-Stokes Equations in the following formats.

For example, the most widely used standard SPH formulations for N-S equations can be written as:

$$\frac{d\rho_i}{dt} = \sum_j m_j \vec{v}_{ij} \nabla_i W_{ij} \quad OR \quad \rho_i = \sum_j m_j W_{ij}$$

$$\frac{d\vec{v}_i}{dt} = -\sum_j m_j \left(\frac{p_j}{\rho_j^2} + \frac{p_i}{\rho_i^2} \right) \nabla_j W_{ij} + \vec{g} + \sum_j \frac{\xi m_j 2\mu r_{ij} \cdot v_{ij} \nabla_i W_{ij}}{\rho_i \rho_j r_{ij}^2}$$

$$\frac{dU_i}{dt} = \sum_j \frac{4 m_j}{\rho_i \rho_j} \frac{k_i k_j}{k_i + k_j} T_{ij} \frac{\vec{r}_{ij} \cdot \nabla_i W_{ij}}{r_{ij}^2}$$

Equation 28

$$p_i = \frac{\rho_0 c_0^2}{\gamma} \left(\left(\frac{\rho}{\rho_0} \right)^{\gamma} - 1 \right)$$

where μ and ξ are the physical viscosity of fluid and artificial viscous coefficient to stabilized the simulation. In most paper, ξ is selected around 4 [33].

This standard SPH formula for N-S equations have their limitation [34] in global conservation of momentum of the entire system. Also, the truncation errors during the discretization might be too high for a stable simulation in certain cases.

2.5. Interface Treatment

There are two types of interface in SPH simulation, one is solid-liquid interface and another is liquid-gas interface. We are going to talk about the treatment of these two-different interface in SPH simulation in order to achieve more accurate and stable numerical simulation.

2.5.1. Solid-Liquid Interaction

Precise estimation of solid-liquid interaction is essential in simulations with SPH. Assigning solid wall boundary conditions mimicking real physical conditions is a challenging part of a SPH simulation. One possible issue of solid-fluid boundary is the unrealistic penetration or detachment of fluid particles from the boundary walls when the

particles approaches the wall along the minimum/maximum force trajectories. This unrealistic particle penetration/detachment can destroy mass conservation of the simulation domain.

One of the most common way of SPH in treating boundary particles is named "Dynamic Boundary Condition" [35]. In dynamic boundary condition, boundary particles satisfy the same governing equations as fluid particles while their locations are not change with respect to time. Monaghan and Kos [36] proposed another approach named "Repulsive Boundary Condition" in treating boundary particles in SPH. In this repulsive boundary condition, boundary particles provide repulsive force to approaching liquid particles from solid boundary particles. The repulsive force can be mimicked with Lennard-Jones potential which is a function of separation distance between liquid and solid particle in a SPH simulation. In addition to the above two common approaches, other boundary conditions such as ghost particle [37] ,mirroring particle, and semi-analytical wall boundary conditions are also proposed recently to better handle the solid-liquid interaction at the boundary during a SPH simulation [38-40]. In addition to single layer solid boundary, multiple Layers of boundary particles are also proposed to provide symmetric in the support domain when the fluid particles are close to the in the solid-fluid interface, which can in turn numerical accuracy and stability especially when the interface has a complex geometry [41].

2.5.1.a.Dynamic Boundary Condition

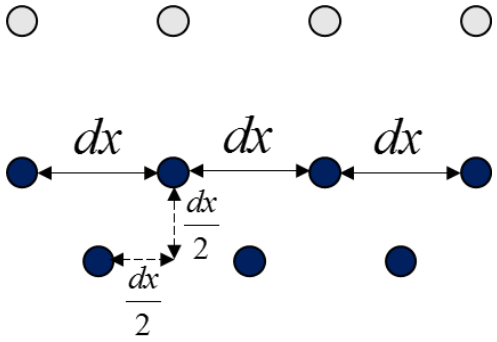

Figure 9 Sketch of boundary particles assignment in dynamic boundary condition

The solid particles is dynamics BCs are considering the same as fluid particles satisfying the same momentum, mass, energy, and state equations of the fluid particles. The main difference compared with fluid particle, solid particles in dynamics BCs are not moving in most cases. In this method, boundary particles are assigned as the blue nodes in Figure 9. Whenever a fluid particle approaches the boundary, the pressure of the boundary particle increases following the mass conservation and equation of state. Due to the increased pressure of boundary particles, fluid particles approaching the solid boundary will be deaccelerated and most likely stopped or even pushed back before unphysical penetration.

2.5.1.b.Repulsive Boundary Condition

In order to prevent penetration during shock wave simulation, which cannot be easily handled with the above dynamic boundary condition, a general form of repulsive force boundary condition was proposed:

$$F_{ij}^{k} = \mathrm{B}\left(r_n, r_t\right) n_j^{k} \qquad \textbf{Equation 29}$$

with F_{ij}^{k} represents the repulsive force on fluid particle i due to the boundary particle j, n_j^{k} the unit normal to boundary particle j, and $\mathrm{B}\left(r_n, r_t\right)$ a function increases rapidly when r_n approaches zero.

To simulate the repulsive force between solid and fluid particles, Monaghan proposed a given potential function similar to Lennard-Jones potential (such as Eq. 30). Therefore, the fluid particle experiences larger repulsive force when it is closer to the solid boundary. This increasing repulsive force can effectively prevents the fluid particles penetration to the solid wall.

$$F_{ij}^{k} = \left[\left(\frac{r_o}{r_{ij}}\right)^{n_1} - \left(\frac{r_o}{r_{ij}}\right)^{n_2}\right] \frac{\mathrm{K}\, r_{ij}^{k}}{r_{ij}^{2}} \quad if \ \frac{r_{ij}}{r_o} \le 1 \qquad \textbf{Equation 30}$$

where, F_{ij}^{k} represents the repulsive force on fluid particle i due to the presence of boundary particle j. The polynomial indices n1 and n2 are commonly selected as 12 or 4 respectively r_0 is the cut-off distance, and K is a parameter adjusting the absolute value of the repulsive force.

One important characteristic of repulsive boundary condition needs to be addressed is the disturbance (i.e., artificial pressure source) can be induced by the repulsive boundary. In other words, the global momentum conservation may not be valid with repulsive boundary conditions.

2.5.1.c.Multi-layer Particle Boundary Condition

One of the most important issue for the solid boundary in SPH is the asymmetric of fluid particles' supporting domain when they are approaching to the solid boundaries. In this multi-layer particle boundary condition, layers of ghost (also named dummy) particles are added to the solid boundaries with their properties obtained by mirroring fluid particles across the solid boundary. This multi-layer particle boundary condition can provide symmetric supporting domain for fluid particles when they are close to the solid boundaries. With the mirrored velocity profile for the dummy particle in the solid boundary, velocity of the solid particles at the solid/liquid interface will exactly be zero which automatically satisfy the non-slip boundary condition used for most macroscale hydrodynamic simulations [42].

2.5.1.d.Generalized Boundary Condition [41]

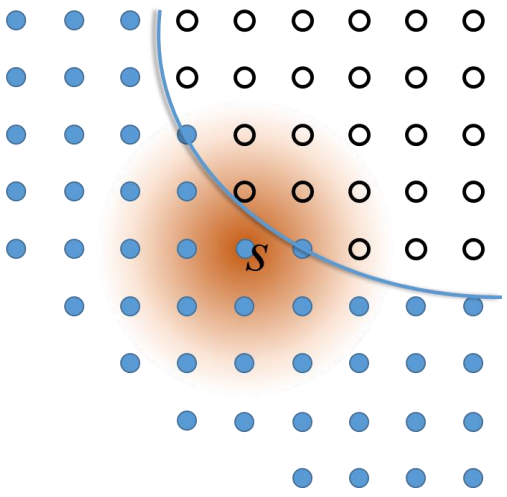

Figure 10 Sketch of 2D SPH using dummy particle boundary condition (solid wall particles are represented as blue dots while fluid particles are represented as black circles)

A generalized boundary condition (as Figure 10) using ghost particles was proposed [41] which can better handle sharp edge and complex geometries compared with multi-layer particle boundary condition discussed before. In this boundary conditions, velocities of ghost particles added at the solid boundaries are obtained by extrapolating the smoothed velocity field of the fluid to the positions of the dummy particles as:

$$\left\langle \vec{v}_i \right\rangle = \frac{\sum_j \vec{v}_j W_{ij}}{\sum_j W_{ij}} \qquad \textbf{Equation 31}$$

Then, the wall dummy particles' velocity can be found by:

$$\vec{v}_s = 2\vec{v}_i - \left\langle \vec{v}_i \right\rangle \qquad \textbf{Equation 32}$$

where, $\vec{v}_i$ is the prescribed wall velocity. Furthermore, pressure values of the wall dummy particles can be estimated from force balance at the solid-liquid interface as:

$$\frac{d\vec{v}_f}{dt} = -\frac{\nabla p_f}{\rho_f} + \vec{g} = \vec{a}_s \qquad \textbf{Equation 33}$$

where, subscript f and s refer to the fluid phase and solid phase. Then, the pressure of solid dummy particles due to the fluid particles can be found by:

$$p_s = \frac{\sum_f p_f W_{sf} + (\vec{g} - \vec{a}_s) \cdot \sum_f \rho_f \vec{r}_{sf} W_{sf}}{\sum_f W_{sf}} \qquad \textbf{Equation 34}$$

2.5.2. Liquid-Gas Interface

Interface between liquid and gas materials in two phase flow problems causes discontinuity in the density field. This discontinuity of density can induce either extremely

large acceleration of the gas particles or extremely small acceleration of the fluid particle when the pressure field is continuous. This abnormal and non-physical particle acceleration at the interface can result in numerical instability of SPH simulation during two phase flow simulations.

To solve this issue, a smoothed density profile $\bar{\rho}_i$ at the interface with following equation can be adopted in the calculation of momentum conservation and energy conservation.

$$\bar{\rho}_i = \sum_j m_j W_{ij} \qquad \textbf{Equation 35}$$

2.6. Numerical Algorithms

Once the GE and the interface boundary conditions are determined, numerical algorithm is required to solve the governing equations. Typical numerical algorithm used in compressible SPH solves momentum, density, position and energy equations in a sequence as:

$$\begin{aligned}
\vec{u}^{\,t+dt} &= \vec{u}^{\,t} + \left(-\frac{1}{\rho}\nabla p^{\,t} + \nabla \cdot \left(\nu \nabla \vec{u}^{\,t} \right) + \bar{F} \right) \Delta t \\
\vec{r}^{\,t+dt} &= \vec{r}^{\,t} + \vec{u}^{\,t+dt} \Delta t \\
\rho^{\,t+dt} &= \rho^{\,t} - \rho^{\,t} \left(\nabla \cdot \vec{u}^{\,t+dt} \right) \Delta t \\
p^{\,t+dt} &= EoS \left(\rho^{\,t+dt} \right)
\end{aligned} \qquad \textbf{Equation 36}$$

The most commonly used equation of state for compressible liquid is the Tait Equation as:

$$p = \frac{\rho_0 c_0^2}{\gamma}\left(\left(\frac{\rho}{\rho_0}\right)^{\gamma} - 1\right)$$ **Equation 37**

where γ is the exponential index is commonly selected as 7 generally, c_0 is the sound speed of the liquid at reference density ρ_0. The commonly sound speed used in the above Tait equation is between 3 and 20 (i.e., is moderate compressible fluid).

2.7. Application of SPH in Fluid Dynamics Problems with Energy Transport

With its capability in handling complex geometries, free surfaces, and interfaces in multiphase systems, SPH has been adopted for transient natural convection by many groups in recent decades (c.f., Table 4). Both CSPH and ISPH have been applied to simulate transient natural convection in different geometries. Danis *et al.* [43] and Aly [44] further improved SPH methods for modelling natural convections in multi-phase systems with Boussinesq approximation. Since the Boussinesq approximation is not valid especially for large temperature changes, efforts have been devoted to extend Boussinesq approach for more generous natural convection modelling with SPH. Szewc *et al.* [45] introduced a density correction term as a function of temperature to extend Boussinesq for larger temperature variations. Such method has been successfully in simulating natural convections in a square cavity using SPH.

Table 4 Application of SPH in heat and mass flows

Year	Author	Title	Journal	Notes
1998	Paul W. Cleary (Australia)	Modelling confined multi-material heat and mass flows using SPH	Applied Mathematical Modelling 22 (1998) 981-993	Boussinesq Approximation is implemented in SPH
2011	K. Szewc (Poland) J. Pozorski (Poland) A. Taniere (France)	Modeling of natural convection with smoothed Particle Hydrodynamics: Non-Boussinesq formulation	International Journal of Heat and Mass Transfer 54 (2011) 4807-4816	1. Gay-Lussac number introduced to describe the density variations caused by temperature. 2. Hydrostatic forces of the center point : $\mathbf{F}_{ij} = \frac{1}{\varrho_{ij}^{corr}}\left[\frac{\partial p}{\partial x}, \frac{\partial p}{\partial y}\right]_{ij} = \frac{1}{\varrho_{ij}^{corr}}\left[\frac{p_{ij}^{E} - p_{ij}^{W}}{\Delta x_{ij}}, \frac{p_{ij}^{N} - p_{ij}^{S}}{\Delta y_{ij}}\right]$
2013	M. E. Danis(Turkey) M. Orhan(Turkey) A. Ecder(Turkey)	ISPH modelling of transient natural convection	International Journal of Computational Fluid Dynamics 27 (2013)No.1, 15-31	1. Eulerian form of governing equation is used. 2. Boussinesq approximation implemented. 3. Density field is kept constant and uniformity of particle distribution is guaranteed during the simulation.
2015	Abdelraheem Mahmoud Aly (Egypt)	Modeling of multi-phase flows and natural convection in a square cavity using an incompressible smoothed particle hydrodynamics	International Journal of Numerical Methods for Heat & Fluid Flow	Solve Pressure Poisson equation

2.8. Limitations of SPH in Energy Transport and Fluid Dynamics Problems

Due to the large temperature variation during LIEB, the Boussinesq approximation assuming a linear correlation between the buoyancy force and the temperature difference, which is only valid for small temperature variations, is no longer appropriate. Therefore, SPH cannot handle the situations with large temperature difference and highly transient dynamics since the linear temperature difference and buoyancy force correlation is no longer valid [46, 47]. Szewc et al. [45] mitigate this problem through extending the Boussinesq formulation by introducing Gay-Lussac number to better describe the buoyancy force with larger temperature gradient. Until now, no SPH simulation directly determine the buoyancy force from the equation the state of the simulated fluid which can handle the buoyancy force at all temperature range has been done and is required in the simulation of

LIEB. Therefore, we have to calculate the buoyancy force from the density variation of the fluid with/without phase change directly.

3. SPH FOR TRANSIENT HEAT TRANSFER WITHOUT BOUSSINESQ APPROXIMATION

We first modified the equation of state used in traditional CSPH algorithm in order to better handle higher temperature gradient natural convection without Boussinesq approximation. The key modifications of SPH in this section compared with traditional SPH algorithm include: a) revised expression of momentum equation in SPH for presence of multiphase flow; b) Equation of Station of real water with low compressibility; c) higher order numerical scheme from 3.3 to reduce the pressure fluctuation during SPH simulation with low compressible fluids. Simulations codes used for call cases in this study are modified based on the original series code of SPHysics [16, 48].

In this section, fluid is assumed to have large viscosity (e.g., around 0.0001). This large viscosity is required also in many numerical simulations when the fluid has low compressibility. Low compressibility fluid is sensitive to density fluctuation during a numerical simulation. Even a small fluctuation in the divergence calculation due to the numerical errors (e.g., truncation errors) can cause large pressure noises in the low compressibility flow, which in turn can induce large nonphysical acceleration and destroy the entire simulation. For high fluid viscosity, the large velocity noise during a simulation with low compressibility fluid has a chance to be damped out before inducing a cascade numerical instabilities. It was also discussed in [49, 50] and [51] that traditional SPH cannot a stable simulation results in a closed domain when = Re>100 (i.e., low viscosity fluid).

3.1 Governing Equations

The governing equations adopted in this section are Eq. 38-40. Mass conservation is written as:

$$\frac{d\rho_i}{dt} = \sum_j m_j \mathbf{v}_{ij} \cdot \nabla_{ij} W(\mathbf{r}_i - \mathbf{r}_j, h) \qquad \textbf{Equation 38}$$

Momentum conservation equation in SPH simulation can be derived by substituting SPH approximation of first derivative into momentum conservation equation (Detailed derivation are available in [52].) as

$$\frac{dv_i}{dt} = -\frac{1}{\rho_i}\sum_j V_j \left(p_i + p_j\right)\nabla W_{ij}\left(r_i - r_j, h\right) + g + \sum_j \frac{\xi m_j 2\mu r_{ij} \cdot v_{ij} \nabla_i W_{ij}}{\rho_i \rho_j r_{ij}^2} \qquad \textbf{Equation 39}$$

where μ and ξ are the viscosity of fluid and viscous coefficient equals 4 [33].

The macroscale energy conservation laws in SPH simulation can be derived by substituting SPH approximation of first derivative into energy conservation equation (detailed derivation can be found in [33, 53]) as

$$\frac{dU_i}{dt} = \sum_j \frac{4m_j}{\rho_i \rho_j} \frac{k_i k_j}{k_i + k_j} T_{ij} \frac{\bar{r}_{ij} \cdot \nabla_i W_{ij}}{r_{ij}^2} \qquad \textbf{Equation 40}$$

3.2 Interface Treatment

3.2.1 Solid-Fluid Interface

We increased the dumpy wall particles from one layer to four layers (as Figure 11). By assuming the first layer wall particle as a symmetric axis with zero velocity, the

velocity, pressure and density of the second, third and fourth layers of the wall bead can be assigned by mirroring the corresponding values in the fluid domain as:

$$\vec{v}_{inside\_solid} = -\vec{v}(r_{mirror}) = -\sum_j v_j W_{ij}(\mathbf{r}_{mirror} - \mathbf{r}_j, h) \quad \textbf{Equation 41}$$

$$p_{inside\_solid} = p(r_{mirror}) = \sum_j p_j W_{ij}(\mathbf{r}_{mirror} - \mathbf{r}_j, h) \quad \textbf{Equation 42}$$

$$\rho_{inside\_solid} = \rho(r_{mirror}) = \sum_j \rho_j W_{ij}(\mathbf{r}_{mirror} - \mathbf{r}_j, h) \quad \textbf{Equation 43}$$

$$a_{solid} = -\sum_j a_j W_{ij}(\mathbf{r}_{mirror} - \mathbf{r}_j, h) \quad \textbf{Equation 44}$$

With this field mirroring, the confine domains simulation is relaxed to a quasi-semi-infinite domain simulation, which can increase the stability in a SPH simulation.

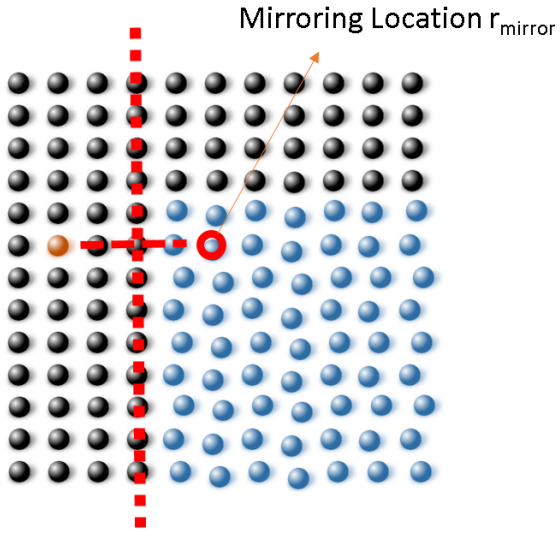

Figure 11 Mirroring boundary conditions: assigning mirroring location of outer layer wall particles

For pressure field, since it reaches its apex at the interface, a simple mirroring the pressure field in the fluid domain to the solid wall will significantly underestimate the pressure of the first layer wall particles. To handle this problem, the pressure of the first layer wall particle is determined from the stagnation pressure of the fluid particle adjacent to the wall, which can result in enough deceleration of the fluid particle to prevent them penetrating through the wall particles. The exact equation to calculation the pressure of first layer solid particles is illustrated in Eq. 45.

$$p_s = \begin{cases} \dfrac{\sum_{fluid} p_{fluid} W_{fs} + \sum_{fluid} \rho_{fluid} \left(g \cdot \vec{r}_{fs} + \dfrac{v_{fs}^2}{2} \right) W_{fs}}{\sum_{fluid} W_{fs}} & if \ \dfrac{\sum_{fluid} v_f W_{sf}}{\sum_{fluid} W_{sf}} \cdot \vec{r}_{sf} > 0 \\ \dfrac{\sum_{fluid} p_{fluid} W_{fs} + \sum_{fluid} \rho_{fluid} \left(g \cdot \vec{r}_{fs} - \dfrac{v_{fs}^2}{2} \right) W_{fs}}{\sum_{fluid} W_{fs}} & if \ \dfrac{\sum_{fluid} v_f W_{sf}}{\sum_{fluid} W_{sf}} \cdot \vec{r}_{sf} < 0 \end{cases} \qquad \textbf{Equation 45}$$

3.2.2 Liquid-Gas Interface

To solve the discontinuity of density at the interface of a gas/liquid multiphase system, a smoothed density profile $\overline{\rho}_i$ at the interface with Eq. 46 is adopted in the calculation of particle acceleration at the interface with Eq. 47.

$$\frac{dv_i}{dt} = -\frac{1}{\overline{\rho}_i} \sum_j V_j \left(p_i + p_j \right) \nabla W_{ij} \left(r_i - r_j, h \right) + g + \sum_j \frac{\xi m_j 2 \mu r_{ij} \cdot v_{ij} \nabla_i W_{ij}}{\rho_i \rho_j r_{ij}^2} \qquad \textbf{Equation 46}$$

$$\overline{\rho}_i = \sum_j m_j W_{ij} (\mathbf{r}_i - \mathbf{r}_j, h) \qquad \textbf{Equation 47}$$

3.3 Numerical Scheme

To further reduce the numerical instability during a SPH simulation of water-like fluid with low compressibility, we introduce 6th order Rung-Kutta scheme [54] for numerical integration of variable U in the transient analysis as:

$$
\begin{aligned}
U_i^{(1)} &= U_i^n \\
U_i^{(2)} &= U_i^n + \frac{7-\sqrt{21}}{14}\Delta t \cdot H\left(t^n, U_i^n\right) \\
U_i^{(3)} &= U_i^n + \frac{1}{2}\Delta t \cdot H\left(t^n + \frac{7-\sqrt{21}}{14}\Delta t, U_i^{(2)}\right) \\
U_i^{(4)} &= U_i^n + \frac{7+\sqrt{21}}{14}\Delta t \cdot H\left(t^n + \frac{1}{2}\Delta t, U_i^{(3)}\right) \\
U_i^{(5)} &= U_i^n + \Delta t \cdot H\left(t^n + \frac{7+\sqrt{21}}{14}\Delta t, U_i^{(4)}\right) \\
U_i^{n+1} &= U_i^n + \frac{1}{180}\left(\begin{array}{l} 9H\left(t^n, U_i^n\right) + 49H\left(t^n + \frac{7-\sqrt{21}}{14}\Delta t, U_i^{(2)}\right) + 64H\left(t^n + \frac{1}{2}\Delta t, U_i^{(3)}\right) \\ +49H\left(t^n + \frac{7+\sqrt{21}}{14}\Delta t, U_i^{(4)}\right) + 9H\left(t^n + \Delta t, U_i^{(5)}\right) \end{array}\right)
\end{aligned}
$$

Equation 48

with $\frac{\partial U_i}{\partial t} = H\left(t, U_i\right)$

This high order scheme can significantly reduce the numerical errors during the time marching calculation and the associated noises in a SPH simulation.

To verify this modified SPH scheme with higher numerical integration, we studied 5 different heat convection cases. First of all, we simulated natural convection of high viscous fluid inside an enclosure. Secondly, natural convection of water inside an enclosure with velocity smoothing was tested. Thirdly, we simulated natural convection of two phase heat convection flow with water and air to verify the capability of handling multiphase systems using our modified scheme. Fourthly, Rayleigh- Bénard convection

of water-like low-compressibility fluid was simulated. The last case simulated using this scheme in this section is two phase Rayleigh- Bénard convection with water and air. Detailed information and results discussion are presented in following section.

3.4 Results and Discussion

3.4.1 Natural Convection of High Viscous Fluid Inside an Enclosure

To verify this modified SPH scheme with 6^{th} order RK numerical integration, we first simulated natural convection of high viscous fluid with low compressibility inside an enclosure. The equation of states of the fluids is assumed to be the same as water with 100 time higher viscosity $\upsilon_0 = 10^{-4} m^2 / s$. This high viscous fluid can achieve a stable SPH results based on previous reports [43, 45, 55].

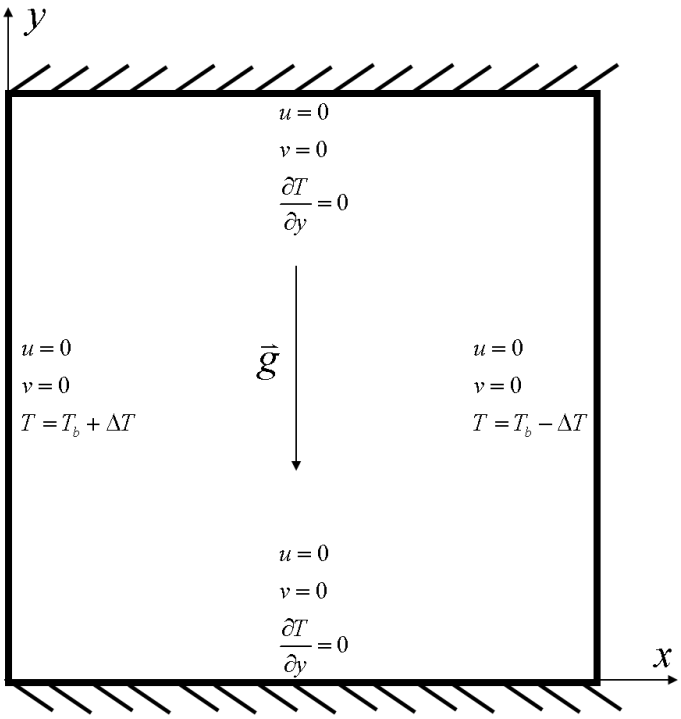

Figure 12 Schematic of square enclosure physical domain and boundary conditions with $\Delta T = 5K$

The simulation domain is illustrated in Figure 12. Higher temperature is assigned at the left wall with the lower temperature assign at the right wall. Due to the temperature difference, distributions of the temperature, density and pressure are changed inside the square enclosure. A flow field is then induced by the density distribution and resulting buoyancy force of the fluid particles, which is exactly a natural convection inside an enclosure.

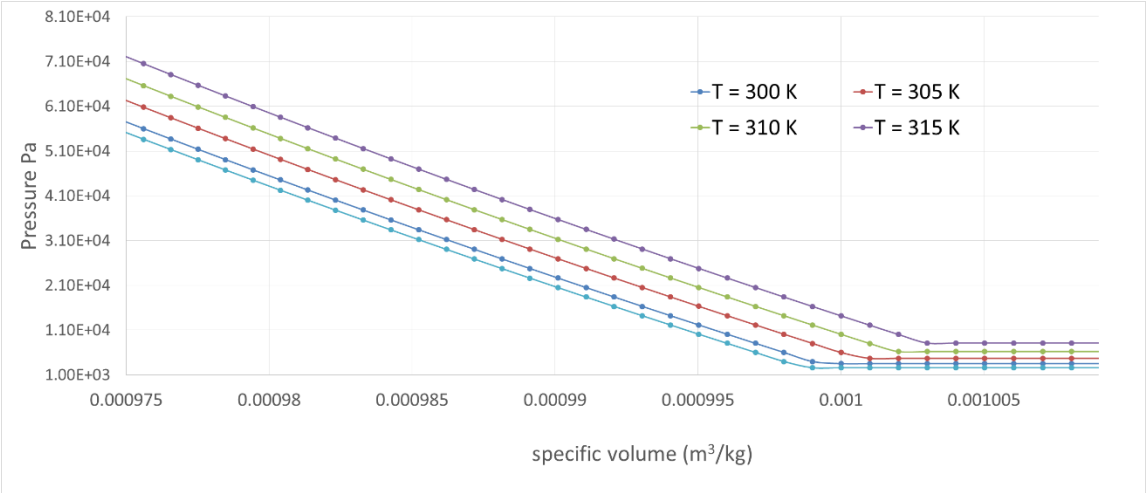

Figure 13 Illustration of water p-v correlation with T = 300K, 305K, 310K and 315K

In this simulation, equation of state of fluid inside the enclosure is the tabulated pressure-density correlation from [56] and illustrated in Figure 13. Prandtl number Pr which is the ratio of dynamics viscosity υ to thermal diffusivity α , equals 709. Rayleigh number which is defined in Eq. 49 is $\sim 1.8 \times 10^{8}$ in this simulation.

$$Ra_{Lx} = \frac{\beta g \left(T_h - T_c\right) L_x^{\,3}}{\upsilon^{2}} \mathrm{Pr} \qquad \textbf{Equation 49}$$

where β is thermal expansion coefficient which equals $0.000207 / K$, T_h is the higher temperature which is 300 K in this case, T_c is the lower temperature equals 290 K in this simulation, and L_x is the characteristic length of enclosure equals 0.5 m in this simulation.

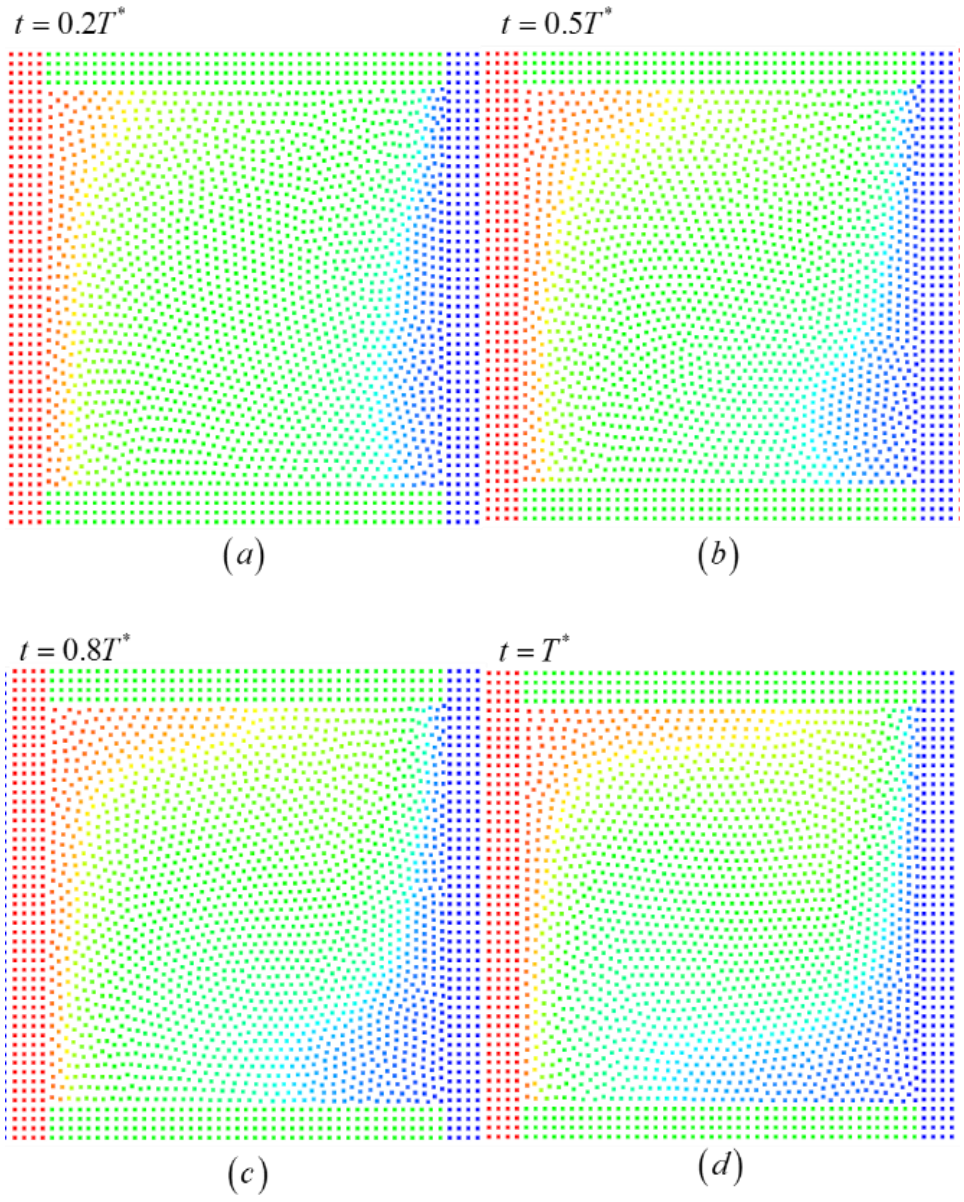

Figure 14 SPH particle snapshot of temperature profile under various t (T^* represent the time it takes to be fully developed)

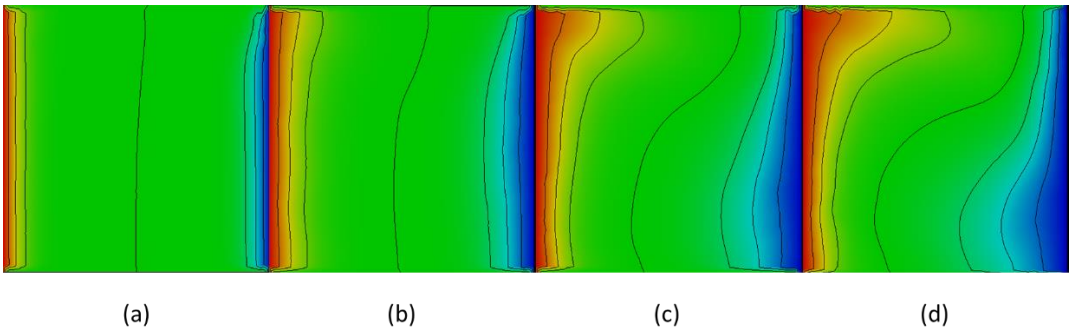

Figure 15 Contour plot of temperature profile under various t

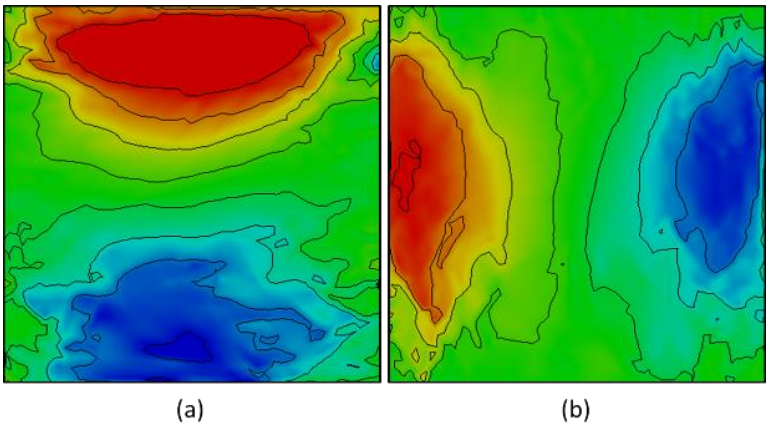

Figure 16 Plots of velocity distribution in steady state: (a) x direction velocity profile; (b) z direction velocity profile;

Figure 14 and Figure 15 present the particle plots and the contour plots of temperature fields at different time. Figure 16 shows the velocity plot of vertical velocity v_z and horizontal velocity v_x. The temperature contours in the beginning of heating are almost vertical due to heat conduction with small velocity values. As the time is going on, pressure increases in the hot liquid region which induces both the decrement of hot liquid density and the increment of vertical velocity. When the hot liquid reaches the top surface, it starts moving horizontally and forms circulation inside the enclosure. At the meantime,

the temperature contours are screwed to the horizontal direction. When the flow is fully developed, as illustrated in in Figure 14, a vortex around the center of the enclosure. The velocity, pressure and density profiles from the SPH simulation at steady-state condition fit with previous studies [57].

The transient time duration of the natural convection before it reaches a steady-state flow pattern can be also estimated from scale analysis [58] as.

$$t_f \approx \left(\frac{\upsilon L_z}{g\beta\left(T_h - T_c\right)\alpha} \right)^{\frac{1}{2}}$$

Equation 50

Based on the result of scaling analysis, required time for the simulation domain to reach steady-state flow under this temperature and fluid conditions is ~120s, which is qualitatively consist with the current simulating taking 100s to reach the flow pattern presented in Figure 16.

3.4.2 Natural Convection of Water inside an Enclosure with Velocity-Smoothing

The second case we simulated is natural convection of water in the same enclosure as Figure 12. The physical properties of fluids are the same as real water with viscosity $\upsilon_0 = 10^{-6} m^2/s$. In this case, Pr is ~7.09, and Ra is $\sim 1.8 \times 10^{10}$ as case one.

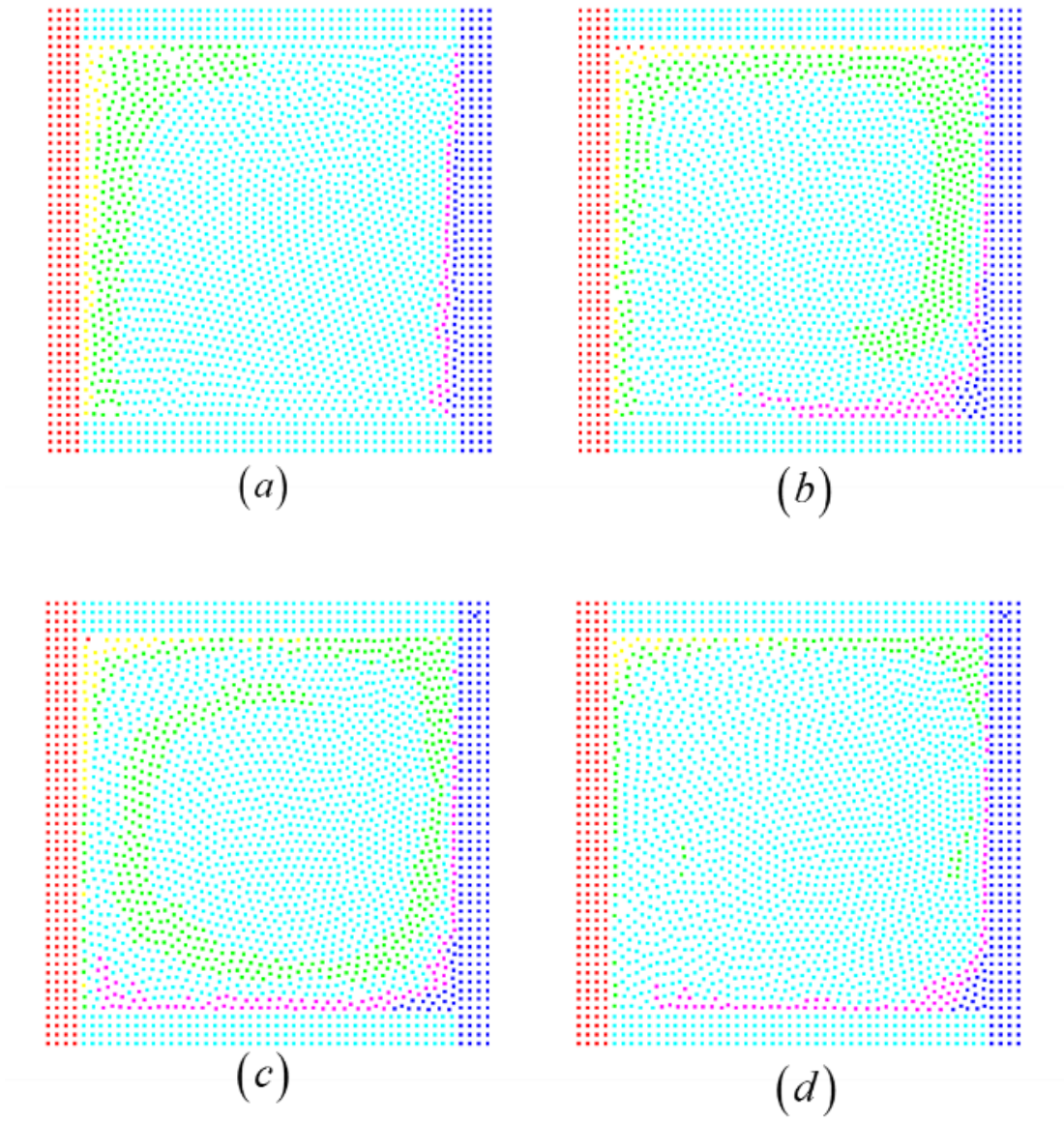

Figure 17 SPH particle snapshot of temperature profile at (a) $t = 0.2 \times T^*$; (b) $t = 0.5 \times T^*$; (c) $t = 0.8 \times T^*$; (d) $t = T^*$

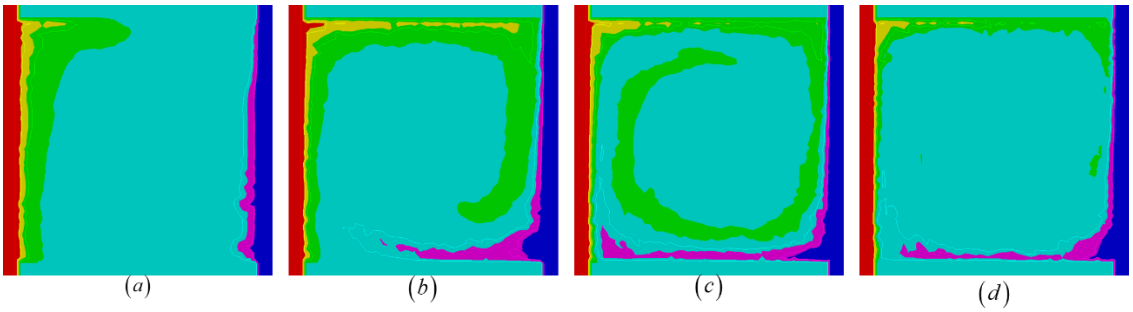

Figure 18 Contour plot of temperature profile at (a) $t = 0.2 \times T^*$; (b) $t = 0.5 \times T^*$; (c) $t = 0.8 \times T^*$; (d) $t = T^*$

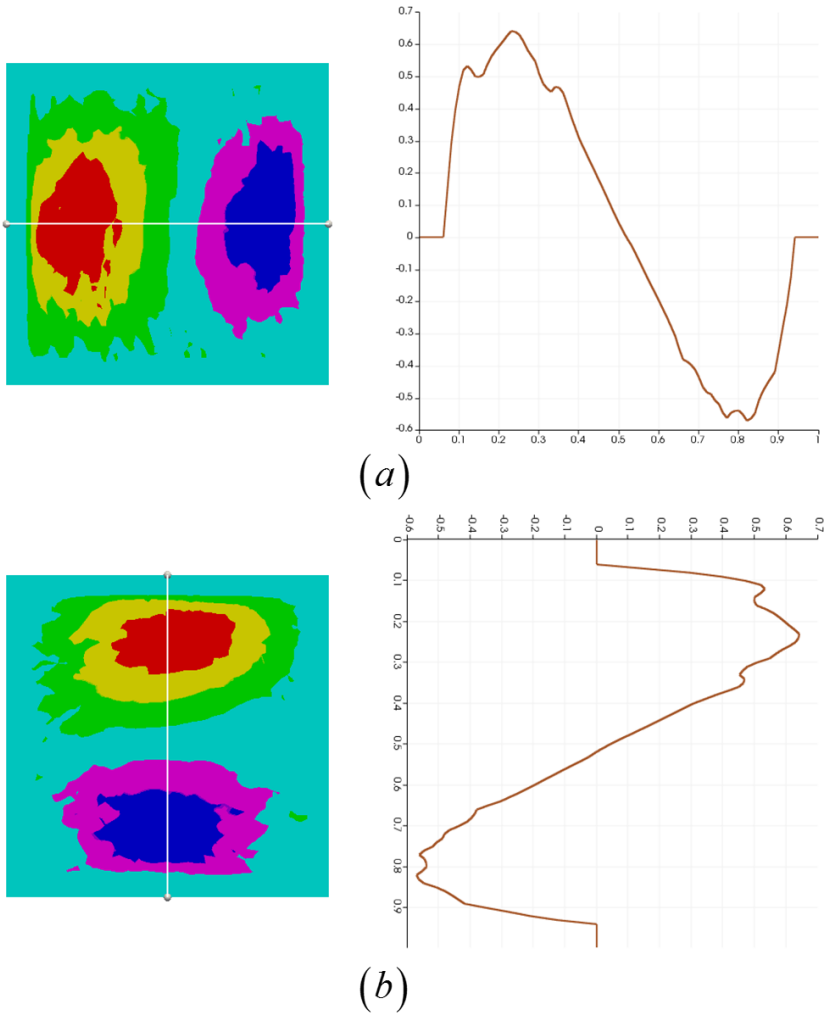

Figure 19 Plots of velocity distribution in steady state: (a) x direction velocity profile; (b) z direction velocity profile;

Figure 17 and Figure 18 present the particle plots and the contour plots of temperature fields at different time. Figure 19 shows the velocity plot of vertical velocity v_z and horizontal velocity v_x. Compared with case one, temperature plot with lower viscosity fro this simulation has more noise but keep the same general shape as case one. The velocity plots are similar to case one but with more noise. The difference between cases one and two are the exact values of velocities when they are fully developed as well as the required time to reach steady state. In case two, the maximum velocity ~0.7 m/s which is 2 orders larger than that in case one (~0.005 m/s). The required time to reach steady state in this simulation is ~20 s which is about one order smaller than that in case one.

3.4.3 Natural Convection of Two Phase Flow with Water and Air

The third case we studied is the natural convection of water with gas layer on top of the liquid domain as illustrated in Figure 20.

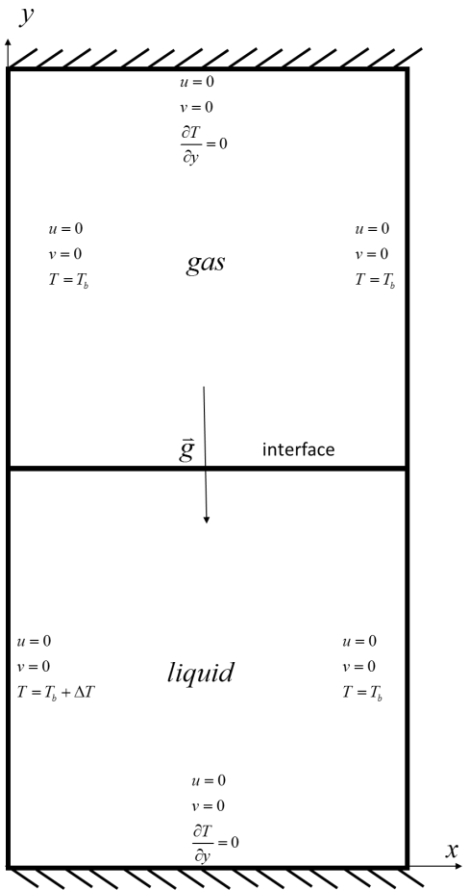

Figure 20 Schematic of enclosure with 0.5×1.0 physical domain and boundary conditions

To illustrate the potential of SPH in handling interfaces in multi-phase flows. The simulation domain of this case is doubled compared with cases one and two. The upper domain is filled with air particles while the lower domain is filled with water. The sizes of both the upper and lower domains are 0.5 m by 0.5 m. Initial temperature of air and water are 295K. When t > 0, the left wall of the water domain is increased to 300K and right wall is reduced to 290K as illustrated in Figure 20. The ideal gas law of air and tabulated Equation of State for water are applied to relate fluid pressures to their densities.

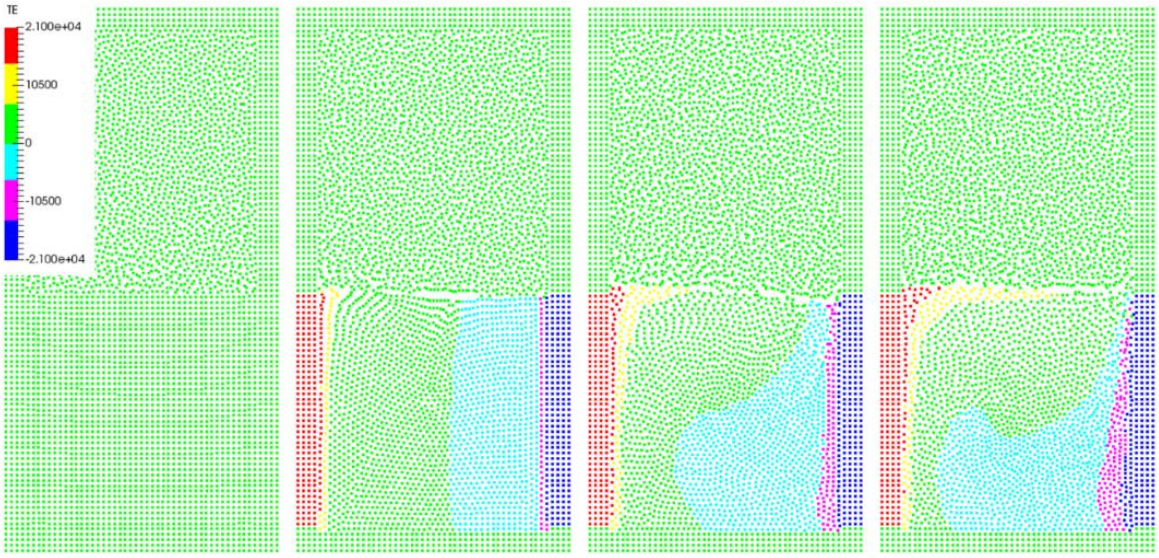

Figure 21 SPH particle snapshot of temperature profile (t_{fully} represents the time it takes to reach fully developed pattern)

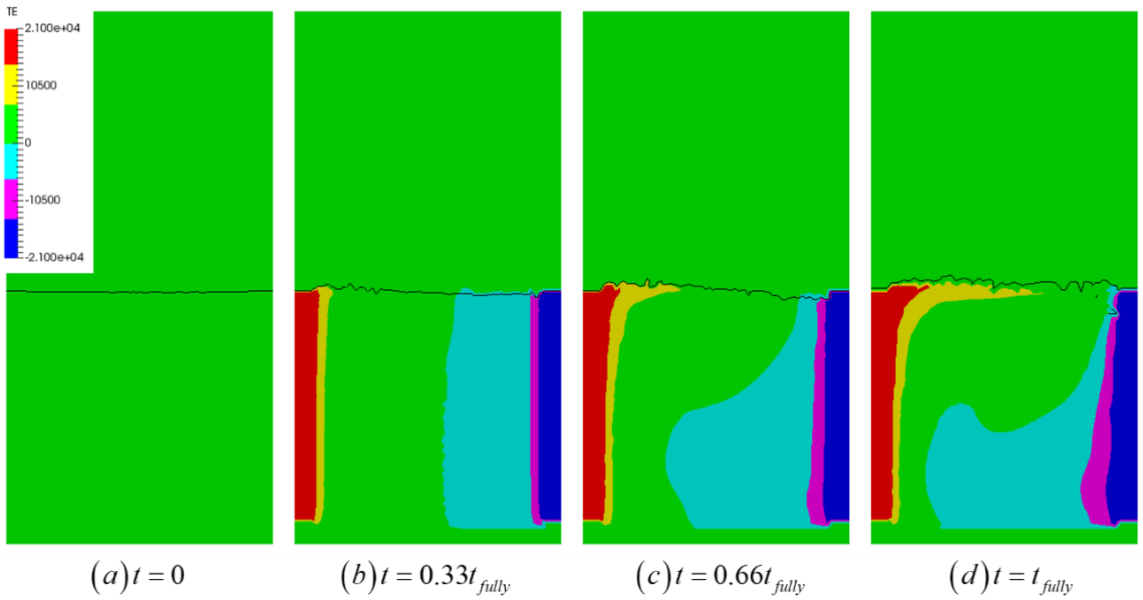

Figure 22 Contour plot of temperature profile of multiphase system under various time

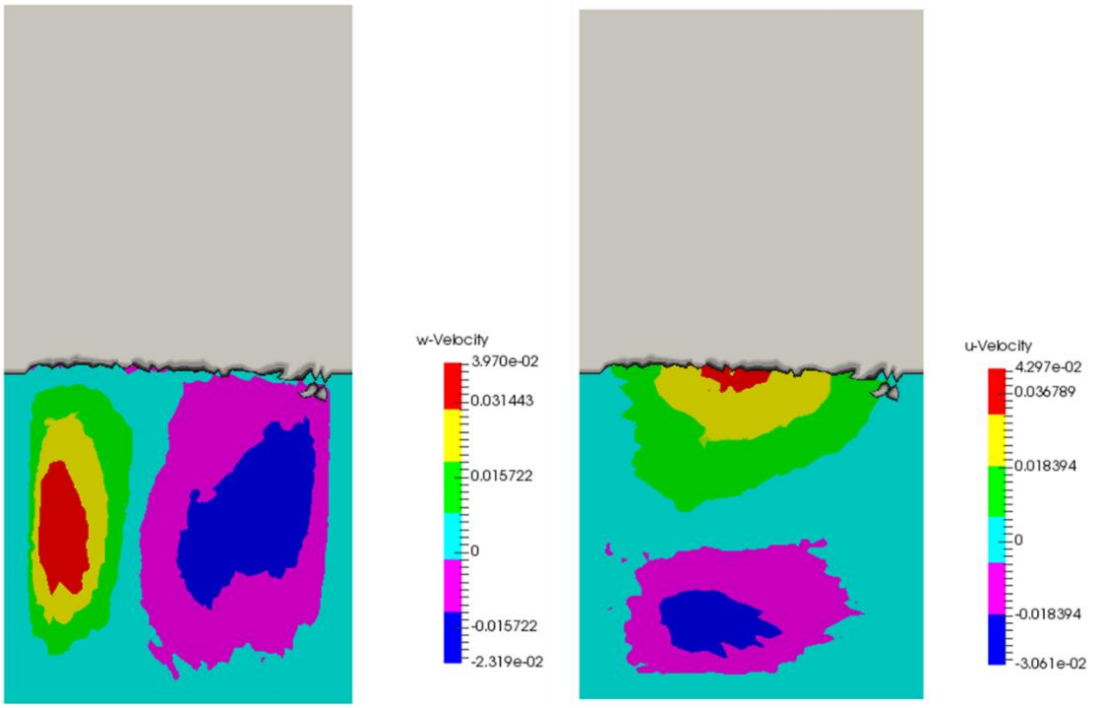

Figure 23 Contour plot of fluid velocity in z-direction (left) and x-direction (right)

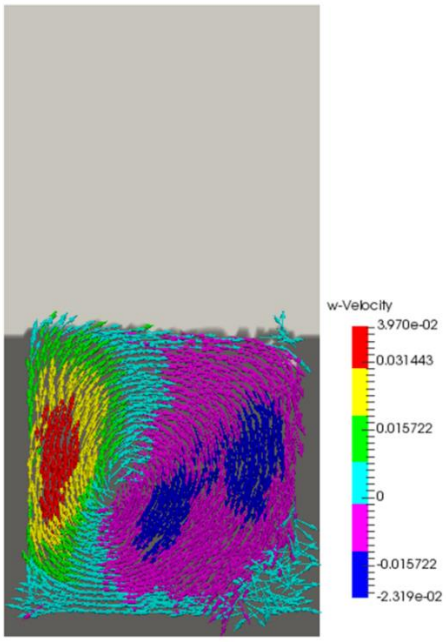

Figure 24 Velocity vector plot in fluid domain after fully developed

Temperature profiles are shown in Figure 21 and Figure 22. Different from single phase natural convection inside an enclosure, liquid water can slight moving upward during a natural convection with air presented on top of it. This will induce disturbance of interface and form wavy interface. Velocity contour plot and velocity vector plot of water domain are shown in Figure 23 and Figure 24. Circulation of water can be observed in Figure 23 and Figure 24, which is similar to case one and case two.

3.4.4 Rayleigh-Bénard Convection of Water

The 4th case studied is heating of water-like fluid (with low compressibility but high viscosity) from bottom of an enclosure and cooling from top of the enclosure as Figure 25. Such configuration is also known as Rayleigh-Bénard convection of fluid inside an enclosure. The simulation domain is 1.0×1.0 meter, initial temperature of the fluid is $T_b = 295K$ and $\Delta T = 5K$ in Figure 25.

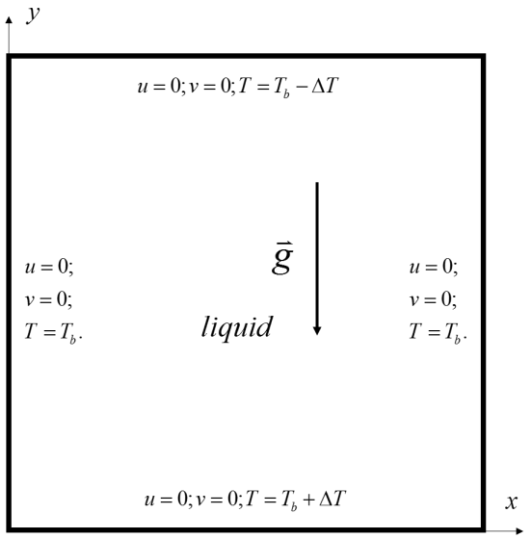

Figure 25 Schematic of enclosure with 1.0m×1.0m physical domain and boundary conditions

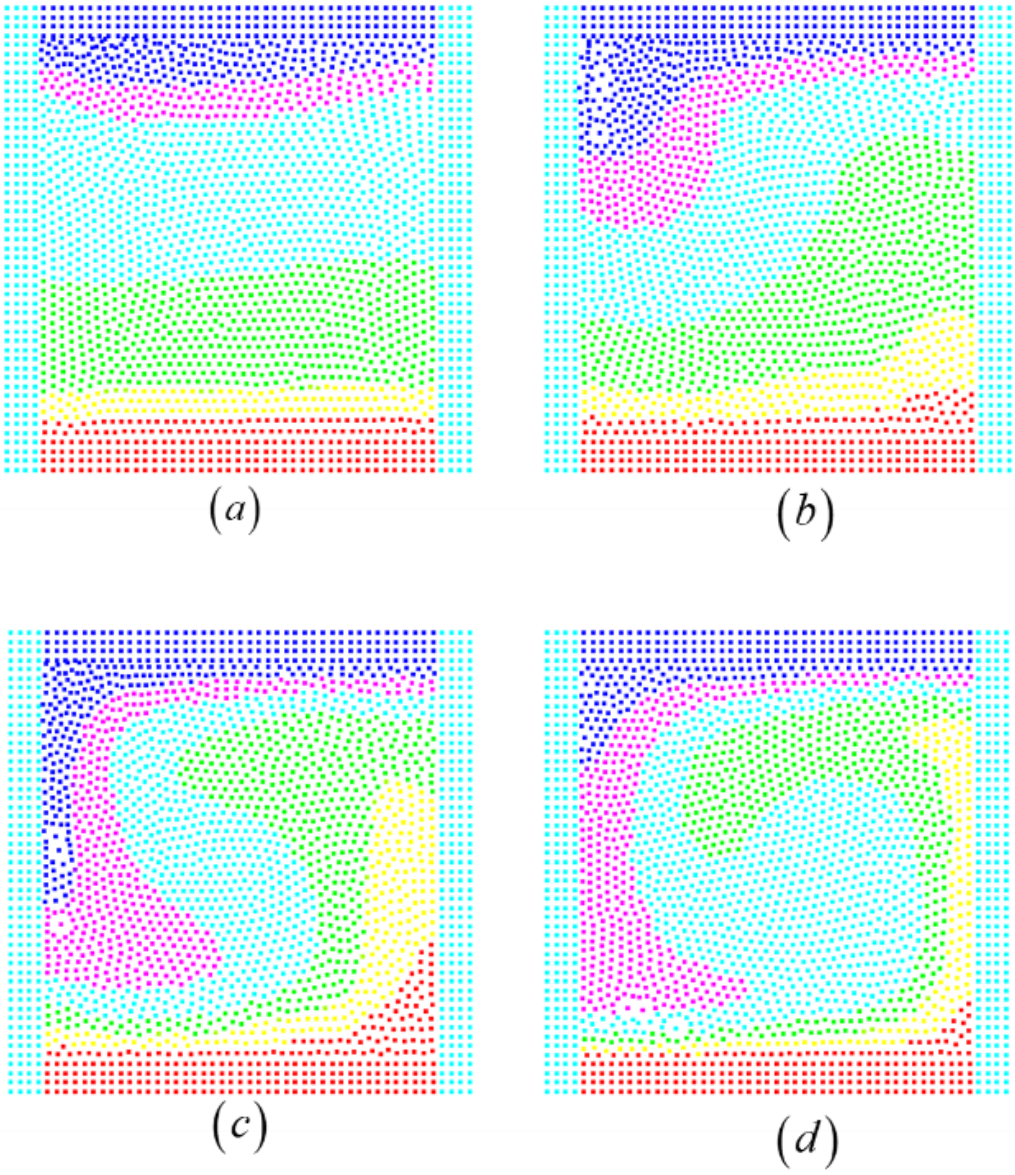

Figure 26 SPH particle snapshot of temperature profile at $(a)\ t = 0.2 \times t_{fully}$, $(b)\ t = 0.5 \times t_{fully}$, $(c)\ t = 0.8 \times t_{fully}$, $(d)\ t = t_{fully}$, (t_{fully} represents the time it takes to reach fully developed pattern)

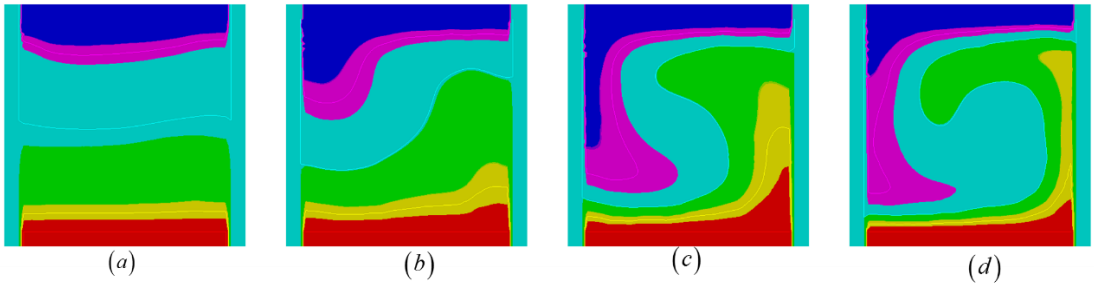

Figure 27 Contour plot of temperature profile at $(a)\ t = 0.2 \times t_{fully}$, $(b)\ t = 0.5 \times t_{fully}$, $(c)\ t = 0.8 \times t_{fully}$, $(d)\ t = t_{fully}$, (t_{fully} represents the time it takes to reach fully developed pattern)

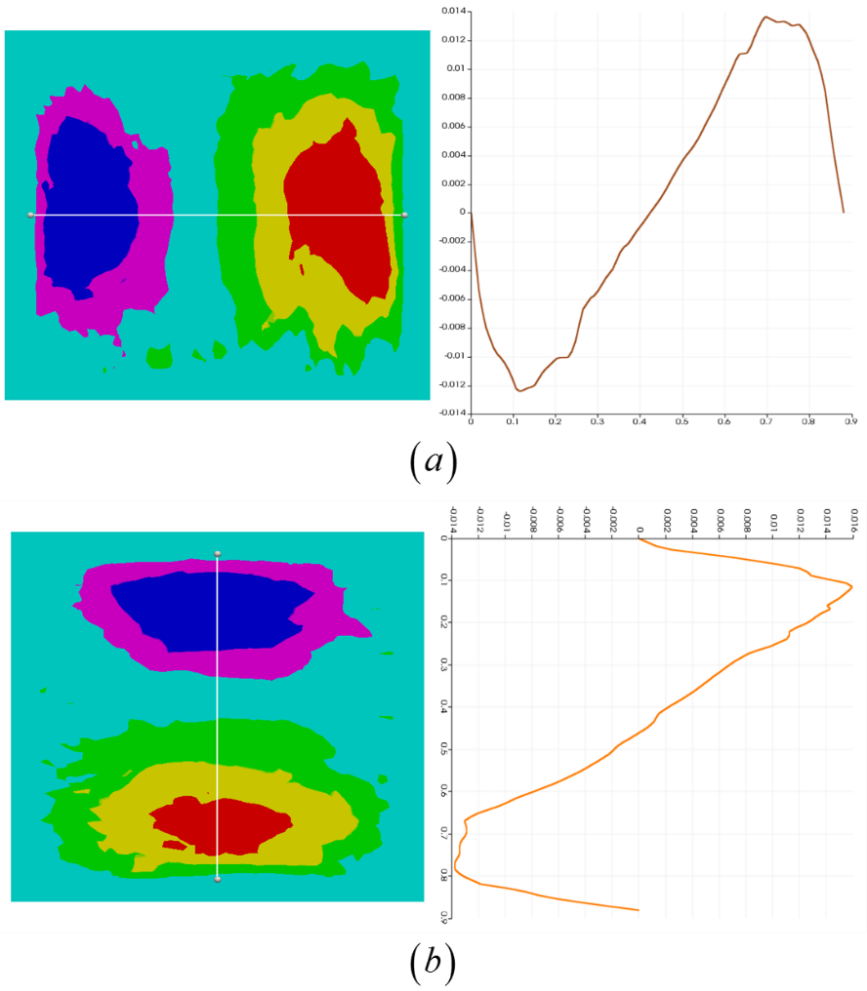

Figure 28 Plots of velocity distribution in steady state: (a) x direction velocity profile; (b) z direction velocity profile;

Figure 26 is the snapshot of SPH particles' temperature distribution and Figure 27 presents the contour plots of temperature profiles over entire domain at different times. The temperature profiles are in good agreement with reported Rayleigh- Bénard convection cell pattern [59]. The circulation of the fluid inside the enclosure with the velocity profiles of fluid are illustrated in Figure 28.

3.4.5 Two Phase Rayleigh- Bénard Convection with Water and Air

The 5th case we studied is two phase Rayleigh- Bénard convection between high and low temperature surfaces as shown in Figure 29.

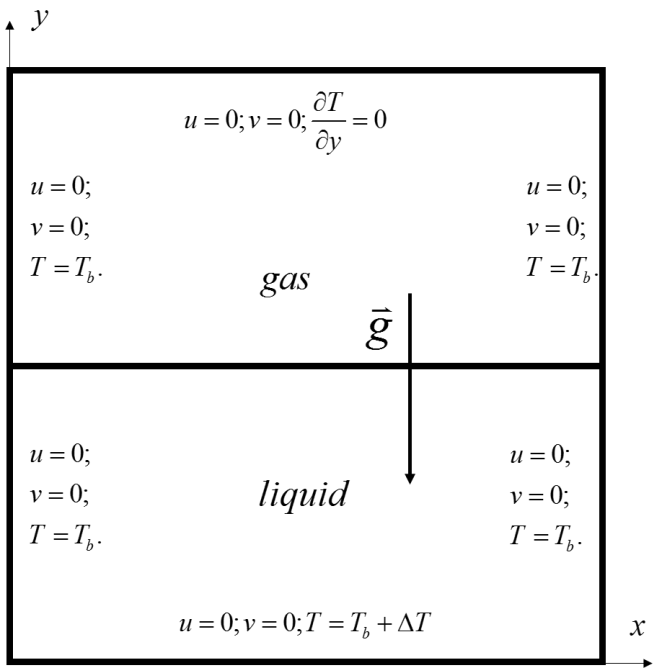

Figure 29 Schematic of enclosure with 1.0×1.0 physical domain and boundary conditions

The upper simulation domain is filled with air particles while the lower domain is filled with water like fluid. Sizes of both the upper and lower domains are$1.0 \text{ m} \times 0.5 \text{ m}$.

Initial temperature of the air and the water are 295K. When t > 0, the bottom temperature of the water domain is increased to 300K as illustrated in Figure 29. Ideal gas law of air and tabulated Equation of State for water are applied to relate pressures to their densities.

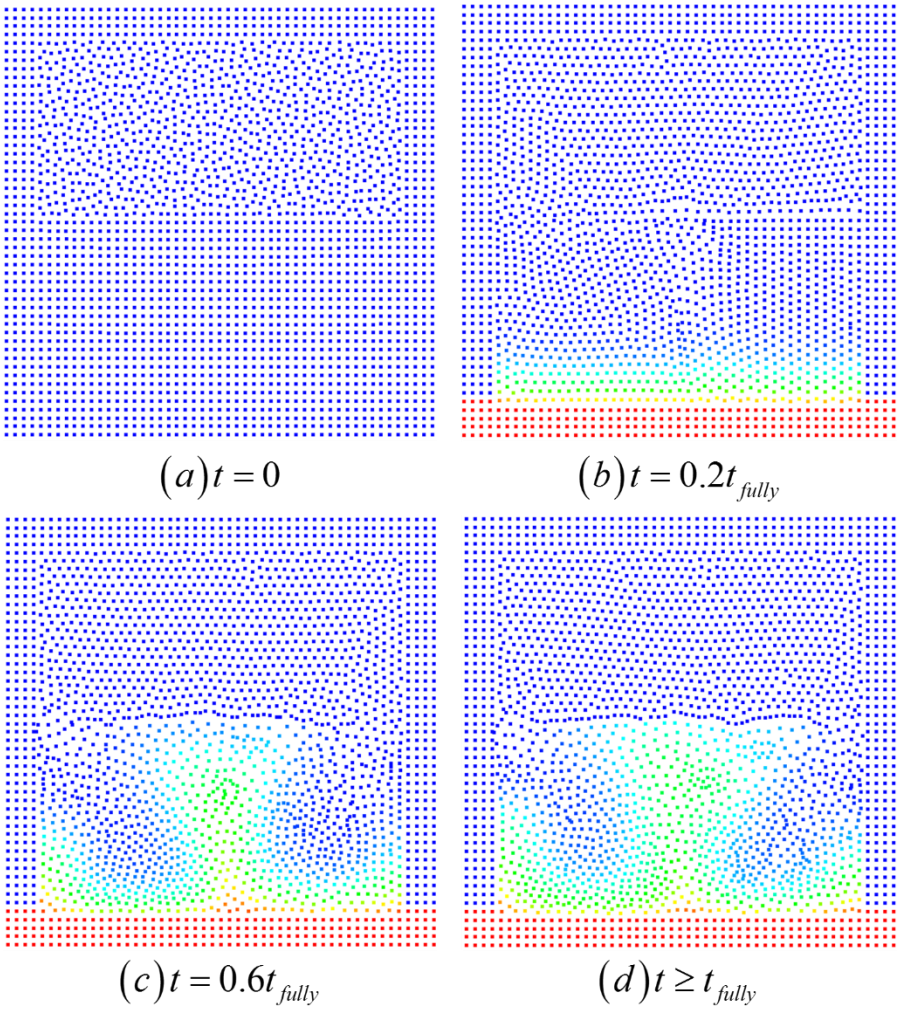

Figure 30 SPH particle snapshot of temperature profile (t_{fully} represents the time it takes to reach fully developed pattern)

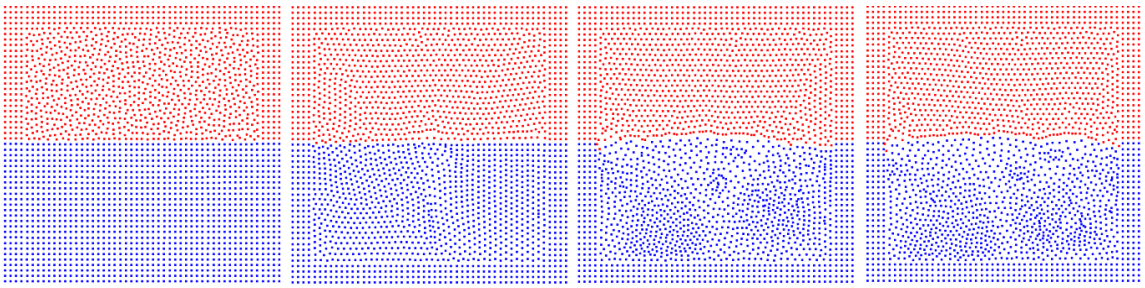

Figure 31 SPH particle snapshot of liquid-gas interface during convection (t_{fully} represents the time it takes to reach fully developed pattern)

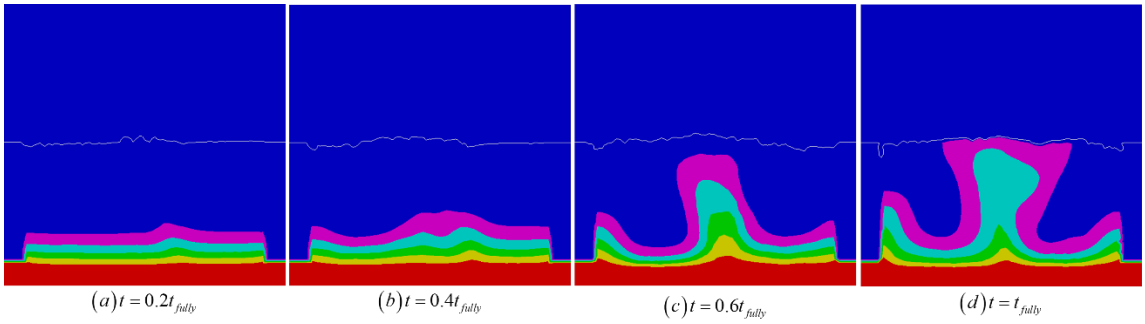

Figure 32 Contour plot of temperature distribution and interface during convection (t_{fully} represents the time it takes to reach fully developed pattern)

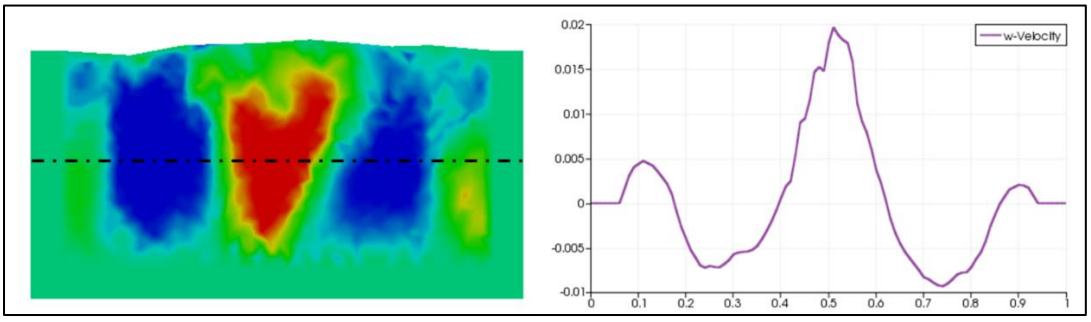

Figure 33 Left: contour plot of velocity in y direction after fully developed; right: plot of velocity along y=0.25.

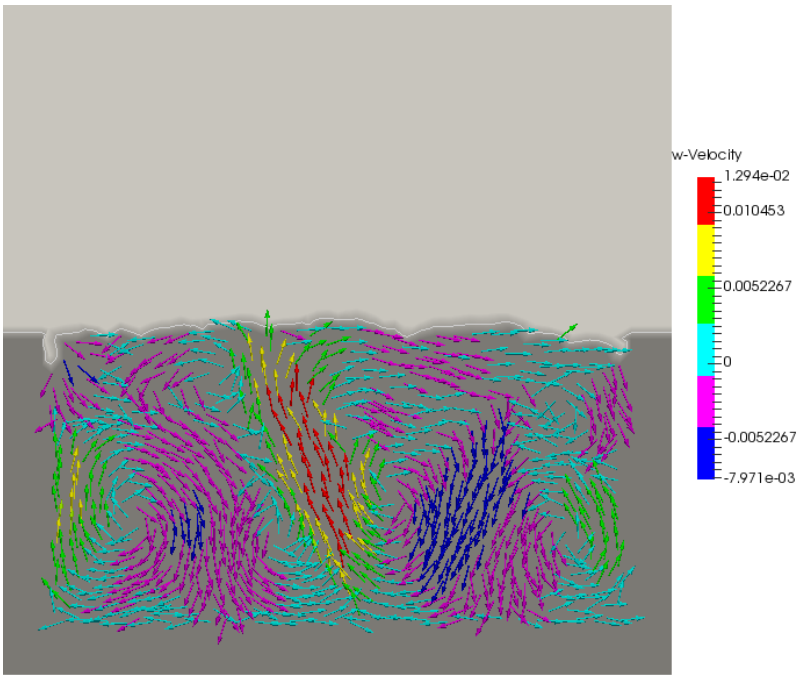

Figure 34 Velocity vector plot in fluid domain after fully developed

The calculated temperature profiles are shown in Figure 30, Figure 31 and Figure 32. The water like liquid with higher temperature is moving upward and forms the circulation inside the liquid domain. Contour plots of velocity in y-direction are shown in Figure 33. From both Figure 33 and Figure 34, the convective Bénard cells [59] can be observed when the simulation reaches steady state. During this two-phase natural convection, liquid-gas interface is slightly distorted as shown in Figure 31 due to the expansion and the associated upward motion of fluid with high temperature. From the results, proposed liquid-gas interface treatment can provide reasonable and stable results for multiphase system during two phase convection.

3.5 Conclusion

Single and two phase transient natural convection inside an enclosure were numerically investigated using traditional compressible SPH methods with the modification of introducing higher R-K numerical scheme and smoothing density discontinuity in momentum equation. The modified SPH algorithm without Boussinesq approximation can be a useful tool for determine mass and energy transport of various fluids with different compressibility and density. The results are in good agreement with previously published works using finite volume method and scaling analysis.

However, we also notice the decrease of accuracy in these simulations when we tried to increase the numerical stability by introducing additional smoothing process. The decrease of accuracy might make the SPH fail to capture some important physical phenomena during simulation, which means this algorithm might not be realistic enough as a predictive tool for unexplored experimental designs. The additional smoothing processes are not required with the modified SPH in this section under high viscous flow condition and can be used to realistically predict the physical process with slow and highly viscous fluid dynamics. To simulate low compressibility and low viscous fluid without introducing smoothing process during the simulation, we need an even higher accuracy algorithm compared with current SPH. This novel high accuracy algorithm developed by us is presented in next section.

4. HIGHER ORDER ACCURACY SPH ALGORITHM FOR WEAKLY COMPRESSIBLE FLUID SYSTEM

SPH approximation uses difference equation to estimate the derivatives of physical property (as discussed in 2.3.3and 2.3.4) which is quite similar to the finite difference method (FDM). If we take a look at the distribution of reconstructed property (i.e., Figure 8 shows the 1D cases of constant property) with traditional SPH approximation, wavy distribution over the simulation domain can manage first order derivative only when particles are uniformly distributed. Calculating 2^{nd} derivatives with traditional SPH is always a problem also due to the way reconstruction property values with the SPH approximation. To solve this large numerical errors, we proposed a higher order numerical method using 2^{nd} order polynomials to approximate physical properties inside discretized sub-systems (particles supporting domain). To find the proper polynomials fit in governing equations, we start from the convergence and error analysis of traditional SPH method.

4.1 Convergence and Higher Order Correction of SPH Methods

The convergence of SPH formulas is important and has been discussed by difference research groups [60, 61] in various approaches. Generally, analytic discussion of convergence starts from finding out the expression of error in the SPH approximation. Gradient of a physical property can be expressed by applying Taylor's expansion as Eq. 51. Then, by subtracting traditional SPH derivative formula from gradient expression in

Eq. 51, the error of derivative calculated in a 2D SPH simulation can be expressed as Eq. 52.

$$\left\langle \nabla f \right\rangle_i = \sum_j \frac{m_j}{\rho_j}\left(f_j - f_i \right)\nabla W_{ij}$$
$$= \sum_j \frac{m_j}{\rho_j}\left(-\bar{r}_{ij}^{\alpha} \nabla^{\alpha} f\Big|_i + \frac{1}{2}\bar{r}_{ij}^{\alpha}\bar{r}_{ij}^{\beta} \nabla^{\alpha}\nabla^{\beta} f\Big|_i - \frac{1}{6}\bar{r}_{ij}^{\alpha}\bar{r}_{ij}^{\beta}\bar{r}_{ij}^{\gamma} \nabla^{\alpha}\nabla^{\beta}\nabla^{\gamma} f\Big|_i + H.O.T \right)\nabla W_{ij}$$

Equation 51

where $\bar{r}_{ij}^{\alpha}\nabla^{\alpha} f = \left(\bar{r}_i - \bar{r}_j\right)^{\alpha} \nabla^{\alpha} f = \left(x_i - x_j\right)\nabla^{x} f + \left(y_i - y_j\right)\nabla^{y} f + \left(z_i - z_j\right)\nabla^{z} f$. The Greek letters as superscript takes value 1,2 in 2D cases and 1,2,3 in 3D cases.

The error can be expressed as:

$$\nabla^{\alpha} f\Big|_i \left(-\sum_j \frac{m_j}{\rho_j}\bar{r}_{ij}^{\alpha}\nabla^{\delta} W_{ij} - I \right) - \nabla^{\alpha}\nabla^{\beta} f\Big|_i \left(\frac{1}{2}\sum_j \frac{m_j}{\rho_j}\bar{r}_{ij}^{\alpha}\bar{r}_{ij}^{\beta}\nabla^{\delta} W_{ij} \right) + \nabla^{\alpha}\nabla^{\beta}\nabla^{\gamma} f\Big|_i \left(\frac{1}{6}\sum_j \frac{m_j}{\rho_j}\bar{r}_{ij}^{\alpha}\bar{r}_{ij}^{\beta}\bar{r}_{ij}^{\gamma}\nabla^{\delta} W_{ij} \right) + H.O.T$$

Equation 52

It is easy to find that error value is dominated by the first term in this expression which is not zero generally. To reduce the error, various methods have been proposed recently, and some of them are discussed in the next section.

4.1.1. Gradient Correction and Kernel Correction (Bonet and Lok [62])

Bonet and Lok [62] first proposed a gradient correction term for the gradient calculation by introducing a matrix *L*. Therefore, the gradient of kernel function can be corrected by matrix *L* as:

$$\tilde{\nabla} W\left(x_i\right) = L_i \nabla W\left(x_i\right) \qquad \textbf{Equation 53}$$

The matrix L can be calculated for each particle by setting the first term of Eq. 46 equals zero, which gives:

$$L_i = \left(\sum_{j=1}^{N} V_j \vec{r}_{ij}^{\,\alpha} \nabla^{\delta} W_{ij} \right)^{-1} \qquad \textbf{Equation 54}$$

Also, Bonet and Lok proposed additional correction named kernel correction which can be expressed as:

$$\tilde{W}_i\left(x\right) = W_i\left(x\right)\alpha\left(x\right)\left[1 + \beta\left(x\right)\cdot\left(x - x_i\right)\right] \qquad \textbf{Equation 55}$$

where the parameters $\alpha(x)$ and $\beta(x)$ enforce the linear property can be exactly interpolated. For example, a linear distributed property ϕ which satisfy the left-hand-side of Eq. 56 can also be guarantee to satisfy the right-hand-side by applying this kernel correction.

$$\phi_0 + \phi_1 \cdot \vec{x} = \sum_{j=1}^{N} V_j \left(\phi_0 + \phi_1 \cdot \vec{x}_i\right) \tilde{W}_i\left(x\right) \qquad \textbf{Equation 56}$$

The first drawback of this method is that this can only guarantee the accuracy in reproducing gradient value when the physical property varies linearly inside the simulation domain. The gradient calculation won't be exact if the physical property shows nonlinear variation. To solve this drawback, more correction function and matrix are required. Another drawback of this method is additional calculation load in order to find corresponding $\alpha(x)$, $\beta(x)$ and matrix L for each particle at each time step.

4.1.2. New Derivative Operators (He [63])

Based on method proposed by Bonet and Lok, He proposed a new method which introduced a new kernel gradient $\overline{\overline{\nabla W}}_{ij}$ as Eq. 57.

$$\overline{\overline{\nabla W}}_{ij} \equiv \overline{\overline{B}}^{\alpha\beta\gamma\delta\varepsilon} \left(s_1\right)_{ij}^{\beta} \left(s_2\right)_{ij}^{\gamma} \left(s_3\right)_{ij}^{\delta} \nabla^{\varepsilon} W_{ij} \qquad \textbf{Equation 57}$$

where, $\overline{\overline{B}}^{\alpha\beta\gamma\delta\varepsilon}$ is a 5th order tensor, $\left(s_1\right)_{ij} = \left(s_2\right)_{ij} \equiv \vec{r}_{ij} + \bar{r}_{ij}^{2}$ $\left(s_3\right)_{ij} \equiv \vec{e}_{ij} + \vec{e}_{ij}^{4}$.

Applying Taylor's expansion of field function, the error of this new gradient kernel function can be expressed as equation below.

$$\left\langle \nabla f \right\rangle_i \Big|_{new} - \nabla^{\alpha} f \Big|_i = \nabla^{\eta}\nabla^{\theta}\nabla^{\lambda}\nabla^{\varepsilon} f \Big|_i \left(\frac{1}{24} \sum_j \frac{m_j}{\rho_j} \bar{r}_{ij}^{\eta} \bar{r}_{ij}^{\theta} \bar{r}_{ij}^{\lambda} \bar{r}_{ij}^{\varepsilon} \overline{\overline{B}}_i^{\alpha\beta\gamma\delta\varepsilon} \left(s_1\right)_{ij}^{\beta} \left(s_2\right)_{ij}^{\gamma} \left(s_3\right)_{ij}^{\delta} \nabla^{\varepsilon} W_{ij} \right) + H.O.T$$

Equation 58

with

$$\begin{bmatrix} \sum_j \frac{m_j}{\rho_j} \bar{r}_{ij}^{\eta} \left(s_1\right)_{ij}^{\beta} \left(s_2\right)_{ij}^{\gamma} \left(s_3\right)_{ij}^{\delta} \nabla^{\varepsilon} W_{ij} \\ \sum_j \frac{m_j}{\rho_j} \bar{r}_{ij}^{\theta} \bar{r}_{ij}^{\varepsilon} \left(s_1\right)_{ij}^{\beta} \left(s_2\right)_{ij}^{\gamma} \left(s_3\right)_{ij}^{\delta} \nabla^{\varepsilon} W_{ij} \\ \sum_j \frac{m_j}{\rho_j} \bar{r}_{ij}^{\eta} \bar{r}_{ij}^{\theta} \bar{r}_{ij}^{\lambda} \left(s_1\right)_{ij}^{\beta} \left(s_2\right)_{ij}^{\gamma} \left(s_3\right)_{ij}^{\delta} \nabla^{\varepsilon} W_{ij} \end{bmatrix} \overline{\overline{B}}_i^{\alpha\beta\gamma\delta\varepsilon} = \begin{bmatrix} -I^{\eta\alpha} \\ 0^{\eta\varepsilon\alpha} \\ 0^{\eta\varepsilon\theta\lambda} \end{bmatrix}$$

Equation 59

It is claimed that this new kernel will provide at least 2 orders consistency which is higher than the method from Bonet and Lok.

Similarly, correction of Laplacian approximation was proposed and introduced another tensor Y_{ij}.

$$\left\langle \nabla \cdot \nabla f \right\rangle_i \Big|_{S1} = 2 \sum_j \frac{m_j}{\rho_j} \left(\frac{f_i - f_j}{\left| \vec{r}_{ij} \right|} - \vec{e}_{ij}^{\,\alpha} \left\langle \nabla^{\alpha} f \right\rangle_i \Big|_{F1} \right) Y_{ij}$$

$$Y_{ij} \equiv \hat{\hat{B}}_i^{\alpha\beta\gamma\delta} \left(s_4 \right)_{ij}^{\alpha} \left(s_5 \right)_{ij}^{\beta} \left(s_6 \right)_{ij}^{\gamma} \nabla^{\delta} W_{ij}$$

$$\left(s_4 \right)_{ij} \equiv \vec{e}_{ij} + \vec{e}_{ij}^{\,2} \quad \left(s_5 \right)_{ij} \equiv \vec{e}_{ij} + \vec{e}_{ij}^{\,3} \quad \left(s_6 \right)_{ij} \equiv \vec{e}_{ij} + \vec{e}_{ij}^{\,4}$$

Equation 60

The corrected Laplacian formula provide 2 order accuracy and expressed as following equation.

$$\left\langle \nabla \cdot \nabla f \right\rangle_i \Big|_{new} - \nabla \cdot \nabla f \Big|_i = \nabla^{\eta} \nabla^{\theta} \nabla^{\lambda} \nabla^{\xi} \nabla^{\nu} f \Big|_i \times \left\{ \frac{1}{60} \sum_j \frac{m_j}{\rho_j} \left[\vec{e}_{ij}^{\,\phi} \left(\sum_j \frac{m_j}{\rho_j} \vec{r}_{ij}^{\,\eta} \vec{r}_{ij}^{\,\theta} \vec{r}_{ij}^{\,\lambda} \vec{r}_{ij}^{\,\xi} \vec{r}_{ij}^{\,\nu} \overline{\overline{\nabla^{\phi} W_{ij}}} \right) + \vec{e}_{ij}^{\,\eta} \vec{r}_{ij}^{\,\theta} \vec{r}_{ij}^{\,\lambda} \vec{r}_{ij}^{\,\xi} \vec{r}_{ij}^{\,\nu} \right] Y_{ij} \right\} + H.O.T$$

Equation 61

$$\begin{bmatrix} \sum_j \frac{m_j}{\rho_j} \left\{ \vec{e}_{ij}^{\,\phi} \left(\sum_j \frac{m_j}{\rho_j} \vec{r}_{ij}^{\,\eta} \vec{r}_{ij}^{\,\theta} \overline{\overline{\nabla^{\phi} W_{ij}}} \right) + \vec{e}_{ij}^{\,\eta} \vec{r}_{ij}^{\,\theta} \right\} \left(s_4 \right)_{ij}^{\alpha} \left(s_5 \right)_{ij}^{\beta} \left(s_6 \right)_{ij}^{\gamma} \nabla^{\delta} W_{ij} \\ \sum_j \frac{m_j}{\rho_j} \left\{ \vec{e}_{ij}^{\,\phi} \left(\sum_j \frac{m_j}{\rho_j} \vec{r}_{ij}^{\,\eta} \vec{r}_{ij}^{\,\theta} \vec{r}_{ij}^{\,\lambda} \overline{\overline{\nabla^{\phi} W_{ij}}} \right) + \vec{e}_{ij}^{\,\eta} \vec{r}_{ij}^{\,\theta} \vec{r}_{ij}^{\,\lambda} \right\} \left(s_4 \right)_{ij}^{\alpha} \left(s_5 \right)_{ij}^{\beta} \left(s_6 \right)_{ij}^{\gamma} \nabla^{\delta} W_{ij} \\ \sum_j \frac{m_j}{\rho_j} \left\{ \vec{e}_{ij}^{\,\phi} \left(\sum_j \frac{m_j}{\rho_j} \vec{r}_{ij}^{\,\eta} \vec{r}_{ij}^{\,\theta} \vec{r}_{ij}^{\,\lambda} \vec{r}_{ij}^{\,\xi} \overline{\overline{\nabla^{\phi} W_{ij}}} \right) + \vec{e}_{ij}^{\,\eta} \vec{r}_{ij}^{\,\theta} \vec{r}_{ij}^{\,\lambda} \vec{r}_{ij}^{\,\xi} \right\} \left(s_4 \right)_{ij}^{\alpha} \left(s_5 \right)_{ij}^{\beta} \left(s_6 \right)_{ij}^{\gamma} \nabla^{\delta} W_{ij} \end{bmatrix} \hat{\hat{B}}_i^{\alpha\beta\gamma\delta} = \begin{bmatrix} -I^{\eta\theta} \\ 0^{\eta\theta\lambda} \\ 0^{\eta\theta\lambda\xi} \end{bmatrix}$$

Equation 62

When Eq. 61 is satisfied, the dominating term of this error is claimed to include 5th derivative of field property, and 4th order accuracy can be obtained by this method. Therefore, this new method can be applied to evaluate 4th order polynomial and provide exact value.

However, two tensors $\overline{\overline{B}}^{=\alpha\beta\gamma\delta\varepsilon}$ and Y_{ij} introduced in this new algorithm include 32 unknowns each. In either gradient or Laplacian approximation, number of equations are

less than unknowns introduced, therefore certain elements of tensor need to be set to zero in order to solve these equation sets. And only with property selection of zero elements inside tensor, the described higher order accuracy can be achieved. The second drawback of this method is its even heavier computing compared with Bonet and Lok's method.

4.1.3. Finite Difference Smoothed Particle Method

The method proposed by He tried to approximate property distribution inside each sub-system by higher order polynomial. To achieve the same goal, we can start from another approach by obtaining derivatives directly from Taylor series expansion.

We started from an expression of field property ϕ at location j as following equation.

$$\phi_j = \phi_i + \left.\frac{\partial \phi}{\partial x}\right|_i dx + \left.\frac{\partial \phi}{\partial z}\right|_i dz + \frac{1}{2}\left.\frac{\partial^2 \phi}{\partial x^2}\right|_i dx^2 + \frac{1}{2}\left.\frac{\partial^2 \phi}{\partial z^2}\right|_i dz^2 + H.O.T \qquad \textbf{Equation 63}$$

If we multiply the both side of the equation with a proper weight function and sum up all neighbored particles around the center i, we can get:

$$\sum_j (\phi_j - \phi_i)\hat{W}_{ij} = \sum_j \left.\frac{\partial \phi}{\partial x}\right|_i dx\hat{W}_{ij} + \sum_j \left.\frac{\partial \phi}{\partial z}\right|_i dz\hat{W}_{ij} + \sum_j \frac{1}{2}\left.\frac{\partial^2 \phi}{\partial x^2}\right|_i dx^2\hat{W}_{ij} + \sum_j \frac{1}{2}\left.\frac{\partial^2 \phi}{\partial z^2}\right|_i dz^2\hat{W}_{ij} + H.O.T$$

Equation 64

where $\hat{W}_{ij}$ is the modified weight. In Eq. 64, we have 4 unknowns ($\frac{\partial \phi}{\partial x}$, $\frac{\partial \phi}{\partial z}$, $\frac{\partial^2 \phi}{\partial x^2}$, and $\frac{\partial^2 \phi}{\partial z^2}$). This expression is quite similar to the Integral Approximation Method (IAM) discussed in 2.3.3, but different from IAM, 3rd and 4th terms are not combined with other higher order terms in. In real simulation conditions, 3rd and 4th term on the right-hand side

of Eq. 64 are not constantly zero and sometime they can even have significant contribution when large local gradient variations present. Therefore, these two terms should be included in our general formula of derivative calculation.

To solve the four unknowns in Eq. 64, we substitute two kernel functions ($\hat{W}_{ijx} = W_{ij} \times dx \times V_j$ and $\hat{W}_{ijz} = W_{ij} \times dz \times V_j$) into this equation and get 2 equations as Eq. 65 below. These modified weight functions are plot in Figure 35 below.

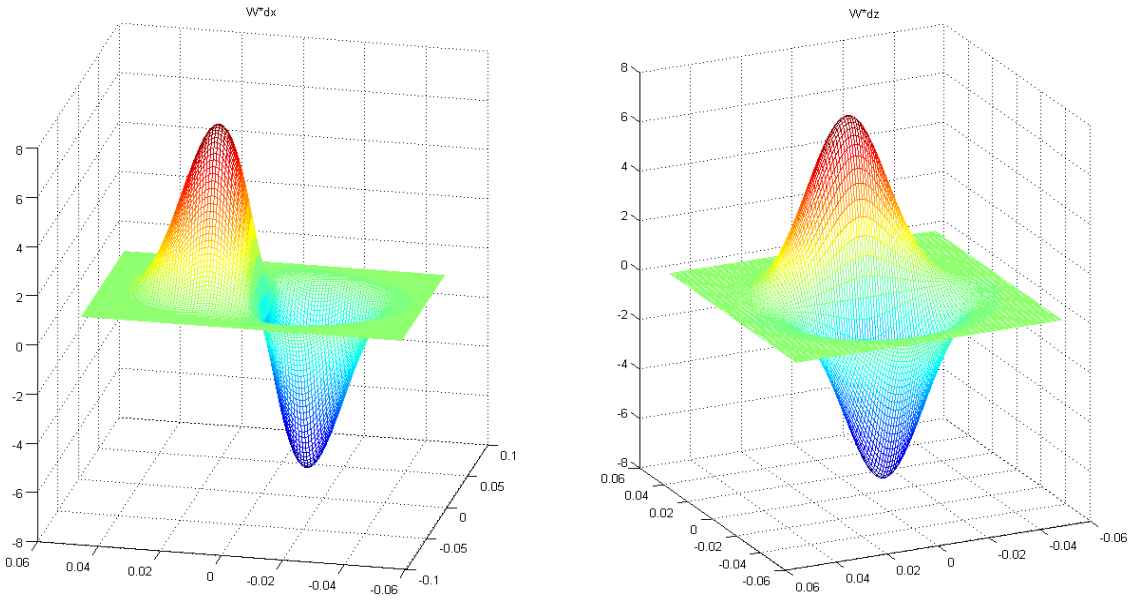

Figure 35 Modified weight functions selected

These two anti-symmetric modified weight functions are selected because they can cancel the contribution from perpendicular axis and emphasis contributions from corresponding axis.

$$\sum_j \left(\phi_j - \phi_i\right) W_{ij} \cdot dx \cdot V_j = \sum_j \left.\frac{\partial \phi}{\partial x}\right|_i dx \cdot W_{ij} \cdot dx \cdot V_j + \sum_j \left.\frac{\partial \phi}{\partial z}\right|_i dz \cdot W_{ij} \cdot dx \cdot V_j$$
$$+ \sum_j \left.\frac{1}{2}\frac{\partial^2 \phi}{\partial x^2}\right|_i dx^2 \cdot W_{ij} \cdot dx \cdot V_j + \sum_j \left.\frac{1}{2}\frac{\partial^2 \phi}{\partial z^2}\right|_i dz^2 \cdot W_{ij} \cdot dx \cdot V_j + H.O.T \qquad (a)$$

Equation 65

$$\sum_j \left(\phi_j - \phi_i\right) W_{ij} \cdot dz \cdot V_j = \sum_j \left.\frac{\partial \phi}{\partial x}\right|_i dx \cdot W_{ij} \cdot dz \cdot V_j + \sum_j \left.\frac{\partial \phi}{\partial z}\right|_i dz \cdot W_{ij} \cdot dz \cdot V_j$$
$$+ \sum_j \left.\frac{1}{2}\frac{\partial^2 \phi}{\partial x^2}\right|_i dx^2 \cdot W_{ij} \cdot dz \cdot V_j + \sum_j \left.\frac{1}{2}\frac{\partial^2 \phi}{\partial z^2}\right|_i dz^2 \cdot W_{ij} \cdot dz \cdot V_j + H.O.T \qquad (b)$$

Obviously, 2 equations are not enough to solve 4 unknowns. To find another 2 equations, we split the supporting domain of particle i as Figure 36 below. For Eq. 65 (a), rather than applying to the entire domain as other SPH approximation, it is applied to left and right subdomain separately to obtain two equations describing the first and second order derivative of the physical properties in x direction. Eq. 65 (b) is applied to both top and bottom subdomain separately to obtain two equations describing the first and second order derivative of physical properties in z direction.

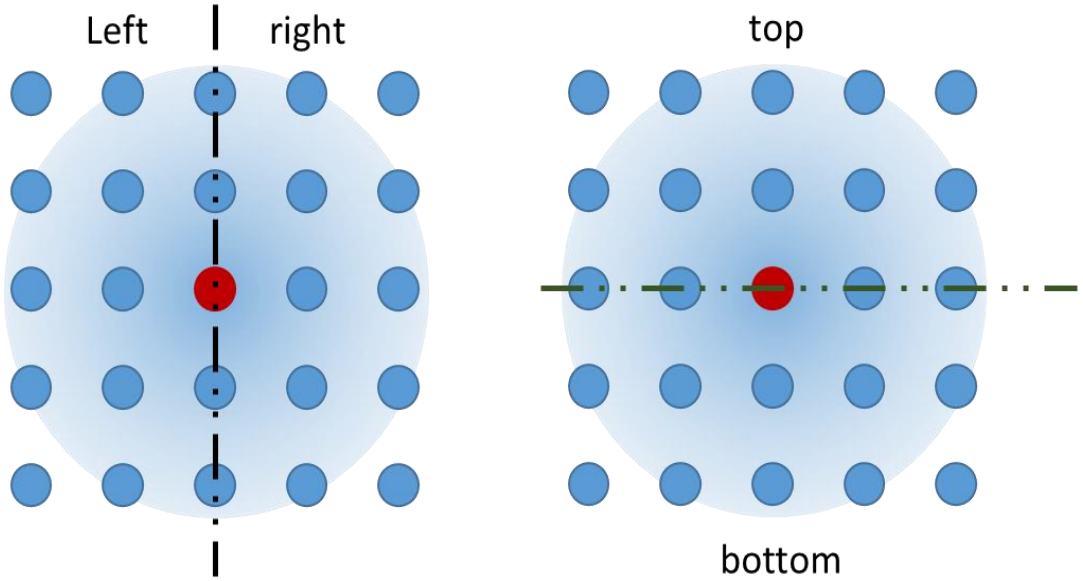

Figure 36 Split into 4 subdomains for center particle

Therefore, as Figure 36 shows, we are able to obtain set of 4 equations for solving 4 unknowns ($\frac{\partial \phi}{\partial x}$, $\frac{\partial \phi}{\partial z}$, $\frac{\partial^2 \phi}{\partial x^2}$, and $\frac{\partial^2 \phi}{\partial z^2}$) as follow:

$$\sum_{j\in right}\left[\phi_i-\phi_j\right]dx_{ij}W_{ij}V_j=\frac{\partial\phi}{\partial x}\sum_{j\in right}dx_{ij}\times dx_{ij}W_{ij}V_j+\frac{\partial\phi}{\partial z}\sum_{j\in right}dz_{ij}\times dx_{ij}W_{ij}V_j$$
$$+\frac{1}{2}\frac{\partial^2\phi}{\partial x^2}\sum_{j\in right}dx_{ij}\times dx_{ij}^2W_{ij}V_j+\frac{1}{2}\frac{\partial^2\phi}{\partial z^2}\sum_{j\in right}dx_{ij}\times dz_{ij}^2W_{ij}V_j \qquad (a)$$

$$\sum_{j\in left}\left[\phi_i-\phi_j\right]dx_{ij}W_{ij}V_j=\frac{\partial\phi}{\partial x}\sum_{j\in left}dx_{ij}\times dx_{ij}W_{ij}V_j+\frac{\partial\phi}{\partial z}\sum_{j\in left}dz_{ij}\times dx_{ij}W_{ij}V_j$$
$$+\frac{1}{2}\frac{\partial^2\phi}{\partial x^2}\sum_{j\in left}dx_{ij}\times dx_{ij}^2W_{ij}V_j+\frac{1}{2}\frac{\partial^2\phi}{\partial z^2}\sum_{j\in left}dx_{ij}\times dz_{ij}^2W_{ij}V_j \qquad (b)$$

$$\sum_{j\in top}\left[\phi_i-\phi_j\right]dz_{ij}W_{ij}V_j=\frac{\partial\phi}{\partial x}\sum_{j\in top}dz_{ij}\times dx_{ij}W_{ij}V_j+\frac{\partial\phi}{\partial z}\sum_{j\in top}dz_{ij}\times dz_{ij}W_{ij}V_j$$
$$+\frac{1}{2}\frac{\partial^2\phi}{\partial x^2}\sum_{j\in top}dz_{ij}\times dx_{ij}^2W_{ij}V_j+\frac{1}{2}\frac{\partial^2\phi}{\partial z^2}\sum_{j\in top}dz_{ij}\times dz_{ij}^2W_{ij}V_j \qquad (c)$$

$$\sum_{j\in bottom}\left[\phi_i-\phi_j\right]dz_{ij}W_{ij}V_j=\frac{\partial\phi}{\partial x}\sum_{j\in bottom}dz_{ij}\times dx_{ij}W_{ij}V_j+\frac{\partial\phi}{\partial z}\sum_{j\in bottom}dz_{ij}\times dz_{ij}W_{ij}V_j$$
$$+\frac{1}{2}\frac{\partial^2\phi}{\partial x^2}\sum_{j\in bottom}dz_{ij}\times dx_{ij}^2W_{ij}V_j+\frac{1}{2}\frac{\partial^2\phi}{\partial z^2}\sum_{j\in bottom}dz_{ij}\times dz_{ij}^2W_{ij}V_j \qquad (d)$$

Equation 66

Equation 66 can be written in matrix format as follows.

$$T=\mathrm{M}\begin{bmatrix}\dfrac{\partial\phi}{\partial x}\\[2ex]\dfrac{\partial\phi}{\partial z}\\[2ex]\dfrac{\partial^2\phi}{\partial x^2}\\[2ex]\dfrac{\partial^2\phi}{\partial z^2}\end{bmatrix}$$

Equation 67

where

$$\mathrm{M} = \begin{bmatrix} \sum_{j\in right} dx_{ij}^2 W_{ij} V_j & \sum_{j\in right} dz_{ij} \times dx_{ij} W_{ij} V_j & \frac{1}{2}\sum_{j\in right} dx_{ij}^3 W_{ij} V_j & \frac{1}{2}\sum_{j\in right} dx_{ij} \times dz_{ij}^2 W_{ij} V_j \\ \sum_{j\in left} dx_{ij}^2 W_{ij} V_j & \sum_{j\in left} dz_{ij} \times dx_{ij} W_{ij} V_j & \frac{1}{2}\sum_{j\in left} dx_{ij}^3 W_{ij} V_j & \frac{1}{2}\sum_{j\in left} dx_{ij} \times dz_{ij}^2 W_{ij} V_j \\ \sum_{j\in top} dz_{ij} \times dx_{ij} W_{ij} V_j & \sum_{j\in top} dz_{ij}^2 W_{ij} V_j & \frac{1}{2}\sum_{j\in top} dz_{ij} \times dx_{ij}^2 W_{ij} V_j & \frac{1}{2}\sum_{j\in top} dz_{ij}^3 W_{ij} V_j \\ \sum_{j\in bottom} dz_{ij} \times dx_{ij} W_{ij} V_j & \sum_{j\in bottom} dz_{ij}^2 W_{ij} V_j & \frac{1}{2}\sum_{j\in bottom} dz_{ij} \times dx_{ij}^2 W_{ij} V_j & \frac{1}{2}\sum_{j\in bottom} dz_{ij}^3 W_{ij} V_j \end{bmatrix}$$

and

$$T = \begin{bmatrix} \sum_{j\in right} \left[\phi_i - \phi_j\right] dx_{ij} W_{ij} V_j \\ \sum_{j\in left} \left[\phi_i - \phi_j\right] dx_{ij} W_{ij} V_j \\ \sum_{j\in top} \left[\phi_i - \phi_j\right] dz_{ij} W_{ij} V_j \\ \sum_{j\in bottom} \left[\phi_i - \phi_j\right] dz_{ij} W_{ij} V_j \end{bmatrix}.$$

By matrix inversion, the $\frac{\partial \phi}{\partial x}$, $\frac{\partial \phi}{\partial z}$, $\frac{\partial^2 \phi}{\partial x^2}$, and $\frac{\partial^2 \phi}{\partial z^2}$ can be obtained by $\mathrm{M}^{-1} \cdot T$.

This novel scheme proposed in this study handles both 1st and 2nd derivatives directly from Taylor series expansion without further assumption. Therefore, this method guarantees 2nd order accuracy of derivative calculation and 1st order accuracy for Laplacian calculation without increment of calculation load. The accuracy can be further improved to 4th and 3rd when the meshfree particles have a symmetric distribution (e.g., remehsed discussed in 4.3.1) Note that all other SPH scheme can only guarantee 1st order accuracy for derivative calculation and less than 1st order accuracy for Laplacian. In the

next section, we describe the required numerical scheme to use this novel high order meshfree method to simulate weakly compressible flow.

4.2 Numerical Scheme and Boundary Conditions

4.2.1 Numerical Algorithm

The calculated first order and second order derivatives from Eq. 67 can be substituted into following governing equations for compressible.

$$\frac{1}{\rho}\frac{d\rho}{dt} + \nabla \cdot \bar{u} = 0$$
$$\frac{d\bar{u}}{dt} = -\frac{1}{\rho}\nabla p + \nabla \cdot (\nu \nabla \bar{u}) + \bar{F} \qquad \textbf{Equation 68}$$
$$p = EoS(\rho, T)$$

Velocity acceleration can be obtained by substituting first order gradient of pressure and second order gradient of velocity into momentum equation. With the $\frac{d\bar{u}}{dt}$ value for each particle, velocity value for the next time step can be obtained with Runge-Kutta scheme as discussed in 3.3.

Numerical scheme discussed in previous section calculates pressure value of each particle from equation of state by substituting updated fluid density, and the updated density value is estimated from density acceleration using mass conservation equation. However, to use this high order novel scheme, we adopted different approach for pressure and density calculation by calculating pressure acceleration directly with modified mass

conservation equation as Eq. 69. This new formula is obtained by substituting isothermal compressibility $\frac{1}{\rho}\frac{d\rho}{dt} = \kappa_T \frac{dp}{dt}$ into mass conservation equation.

$$\frac{dp}{dt} = -\frac{1}{\kappa_T}\nabla \cdot \vec{u} \qquad \textbf{Equation 69}$$

Therefore, pressure acceleration can be obtained from $\nabla \cdot \vec{u}$ with Eq. 69. With obtained $\frac{dp}{dt}$, pressure value of the next time step can be determined with numerical scheme discussed in 4.2.2. The fluid density can be calculated with simplified isothermal equation of state as $\rho = \rho_0 + \kappa_T (p - p_0)$.

However, stability of this algorithm for low compressibility (such as water whose compressibility can be as low as10^{-10} /K) highly depends on the accuracy and stability of gradient calculation which should introduce a numerical error more than 10^{-10}. From our benchmark result shown in 4.3, the accuracy of proposed new method for derivative calculations with dx = 0.01 and dt = 0.00001s can provide small enough numerical error for direct simulation of low compressibility fluid such as water.

The flowchart of this new algorithm in order to use the novel high order accuracy meshfree method developed in this study is shown in Figure 37 below.

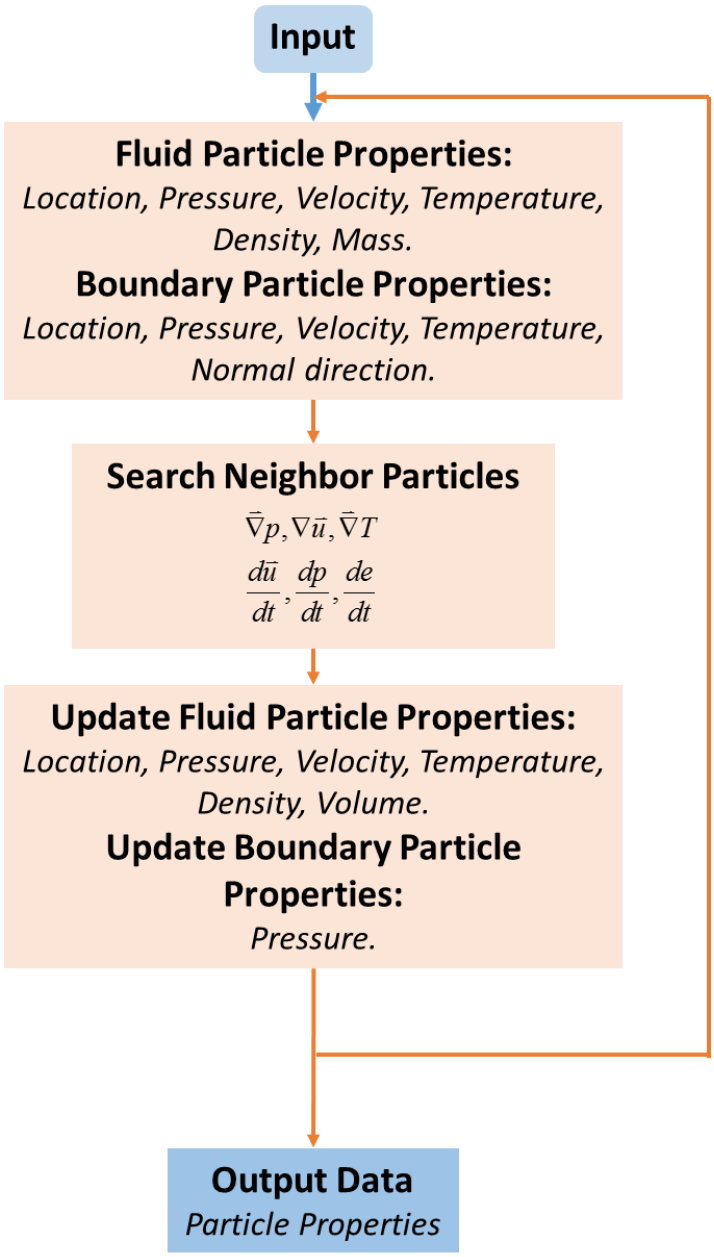

Figure 37 SPH algorithm using higher accuracy gradient method

4.2.2 Strong Stability Preserving (SSP) Runge-Kutta Time Discretization

The adopted numerical integration scheme is 3rd order Runge-Kutta method. To increase numerical stability, we followed Strong Stability-Preserving (SSP) time

discretization methods [64]. Different from traditional linear stable higher-order time discretize method which induce numerical oscillations due to its lack of strong stability, SSP Runge Kutta method can reduce numerical oscillations. Nonlinear method of 3rd order Runge-Kutta method as Eq. 70 was used in this study.

$$u^{(1)} = u^{n} + \Delta t L\left(u^{n}\right)$$
$$u^{(2)} = \frac{3}{4}u^{n} + \frac{1}{4}u^{(1)} + \frac{1}{4}\Delta t L\left(u^{(1)}\right) \qquad \textbf{Equation 70}$$
$$u^{n+1} = \frac{1}{3}u^{n} + \frac{2}{3}u^{(2)} + \frac{2}{3}\Delta t L\left(u^{(2)}\right)$$

4.2.3 Boundary Condition

In this novel method, dynamic boundary conditions by treating wall particles as non-moving fluid particles following the same conservation equations. With this high accuracy scheme for gradient value calculations, no repulsive force oscillation happens in dynamic boundary with this new scheme compared with traditional SPH. As a result, the chance of non-physical penetration of fluid particles through the wall is diminished. Similar to other SPH method, we also adopted multilayer solid particles (discussed in 2.5.1.c) to ensure symmetrical particle distribution for fluid interacting with solid walls. This symmetric distribution can ensure high numerical accuracy (i.e., more than 2nd order and approach to 4th order) for fluid particles both far away from the wall and adjacent to the solid walls.

For those wall particles (i.e., the 2nd to the 4th layer of the wall particles after solid-liquid interface) not interacting directly with fluid particles, pressure values are determined from extrapolation with the pressure gradient at the solid-liquid interface.

To verify our proposed new algorithm, we tested Couette Flow and Lid-Driven Flow inside an enclosure as the benchmarks. Simulation conditions and results of these benchmark cases are presented in next section.

4.3 Test Cases

4.3.1. Couette Flow

We first simulated Coutte flow which is a laminar flow between two infinite plates as illustrated in Figure 38 below. Bottom plate is not moving and located at z=0 while top plate moves with a constant x directions speed U_0 and is located at $z = L$.

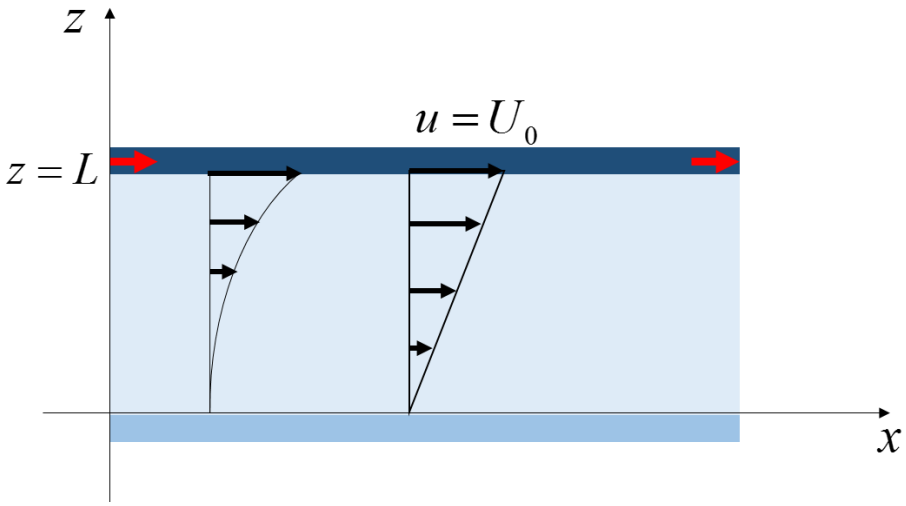

Figure 38 Illustration of Couette flow

In this coquette flow study, a $0.45m \times 0.5m$ domain with 600 particles arranged rectangular at t = 0 as illustrated in Figure 39 is used in the simulation. The upper plate

moves in x direction with constant velocity $U_0 = 2.0$. Periodic boundary condition is applied in x direction to mimic an infinite domain in the x direction.

Figure 39 Initial velocity plot of Couette flow

Simulation result of the velocity profiles at different times are shown in following figures. The dimensionless time in this study is the ratio of time with total time the simulation takes to reach steady state.

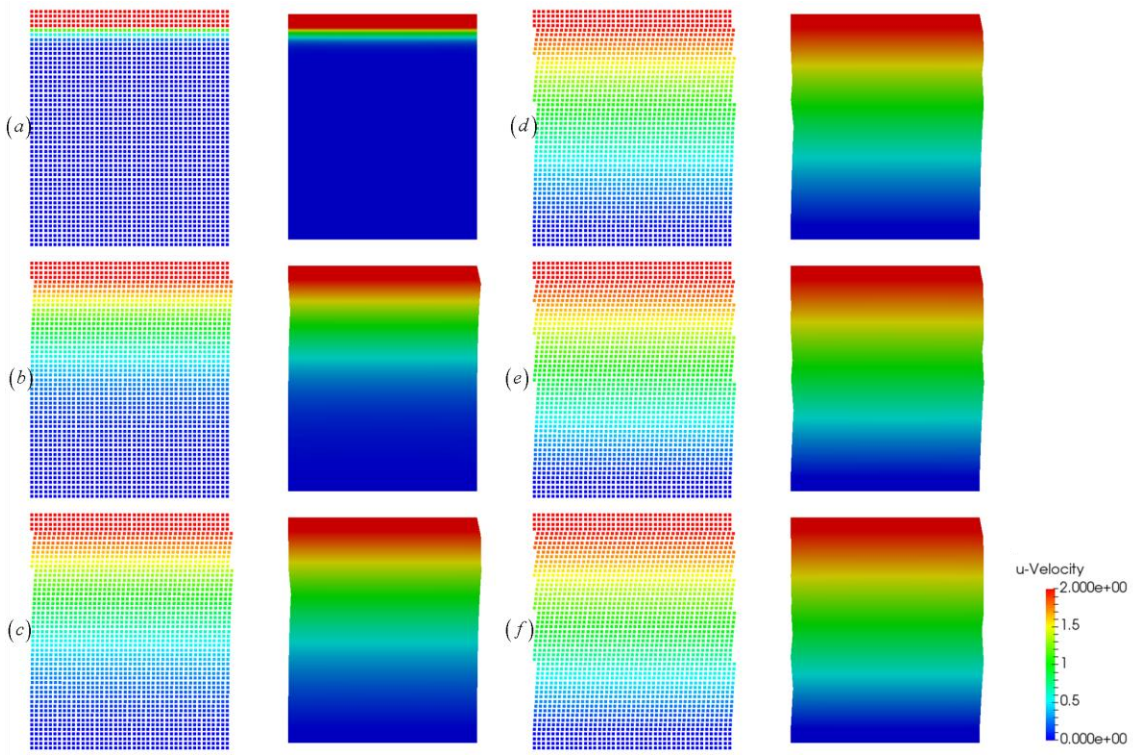

Figure 40 Particle snapshots and x-direction velocity plot at: (a) $t = 0.0002s$, (b) $t = 0.01s$, (c) $t = 0.02s$, (d) $t = 0.03s$, (e) $t = 0.04s$, (f) $t = 0.05s$.

Figure 40 and Figure 41 shows the development of x-direction velocity with respect to z position at various dimensionless time. This simulation result is compatible with analytical results discussed by other scholars.

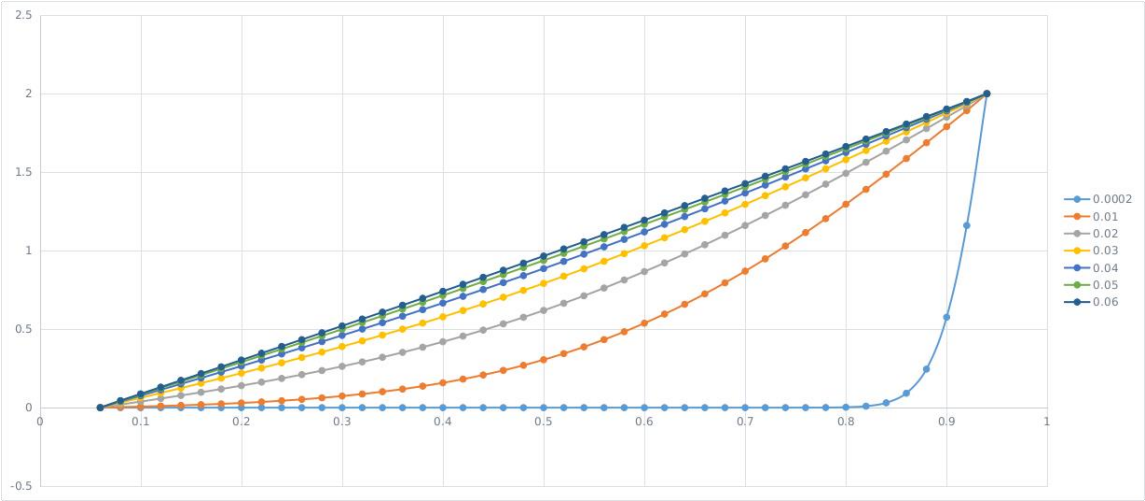

Figure 41 x-direction velocity plot at different time (x axis shows the z distant to the bottom)

4.3.2. Lid Driven Flow Inside Cavity without Remeshing

The second case tested with the proposed new method was lid driven flow inside a cavity (Figure 42). We simulated induced water flow inside square cavity driven with a cap of infinite length with constant x-direction moving speed U_0.

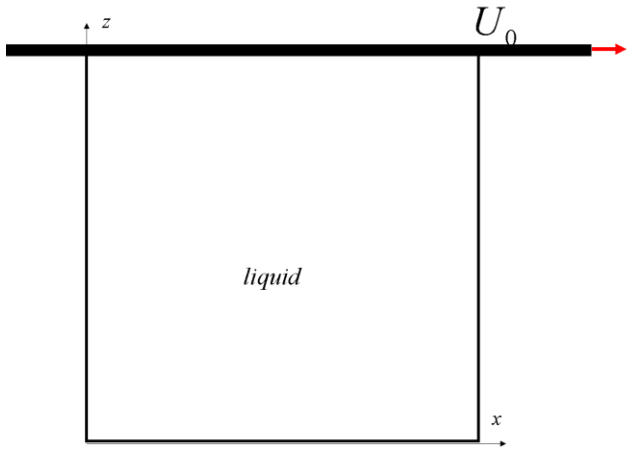

Figure 42 Schematic of lid driven water flow inside square cavity

Simulated domain of this case is a $1.0m \times 1.0m$ square cavity with lid velocity 2.0 m/s in x-direction. Reynolds Number Re in this simulation is equal to 1.0. The viscosity in this simulation is 2.0 in order to reduce the total time the simulation takes to reach steady state. Initial particle assignment and x-direction velocity distribution are shown in Figure 43. Top boundary particles have constant x-direction velocity while their physical locations are fixed during the simulation.

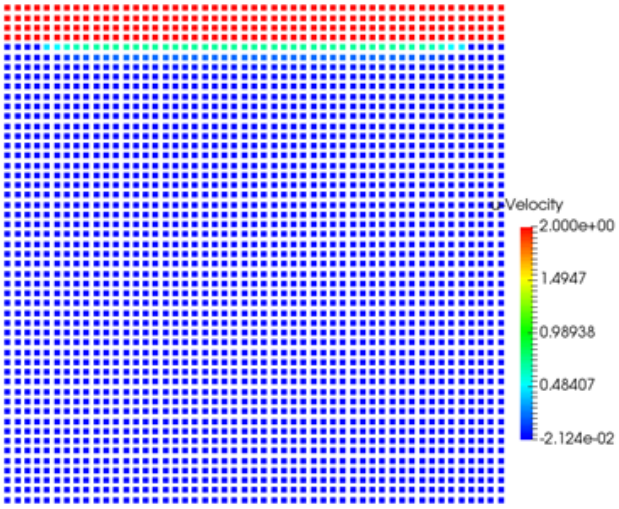

Figure 43 Initial particle assignment and velocity distribution for lid-driven flow inside cavity

Particle snapshot of lid driven transient flow inside a cavity are presented in following Figure 44. The simulation is close to steady state after 0.03s. The velocity distribution along the vertical center line was plotted in Figure 45. The streamline plot in Figure 46. The x-direction velocity has its minimum velocity at z location around half of the maximum height. These results are in consistent with previous results in such a low

Reynolds number. Note that a clear circulation flow pattern inside the enclosure can be observed in the streamline plot (Figure 46), which is a characteristic in a cavity flow.

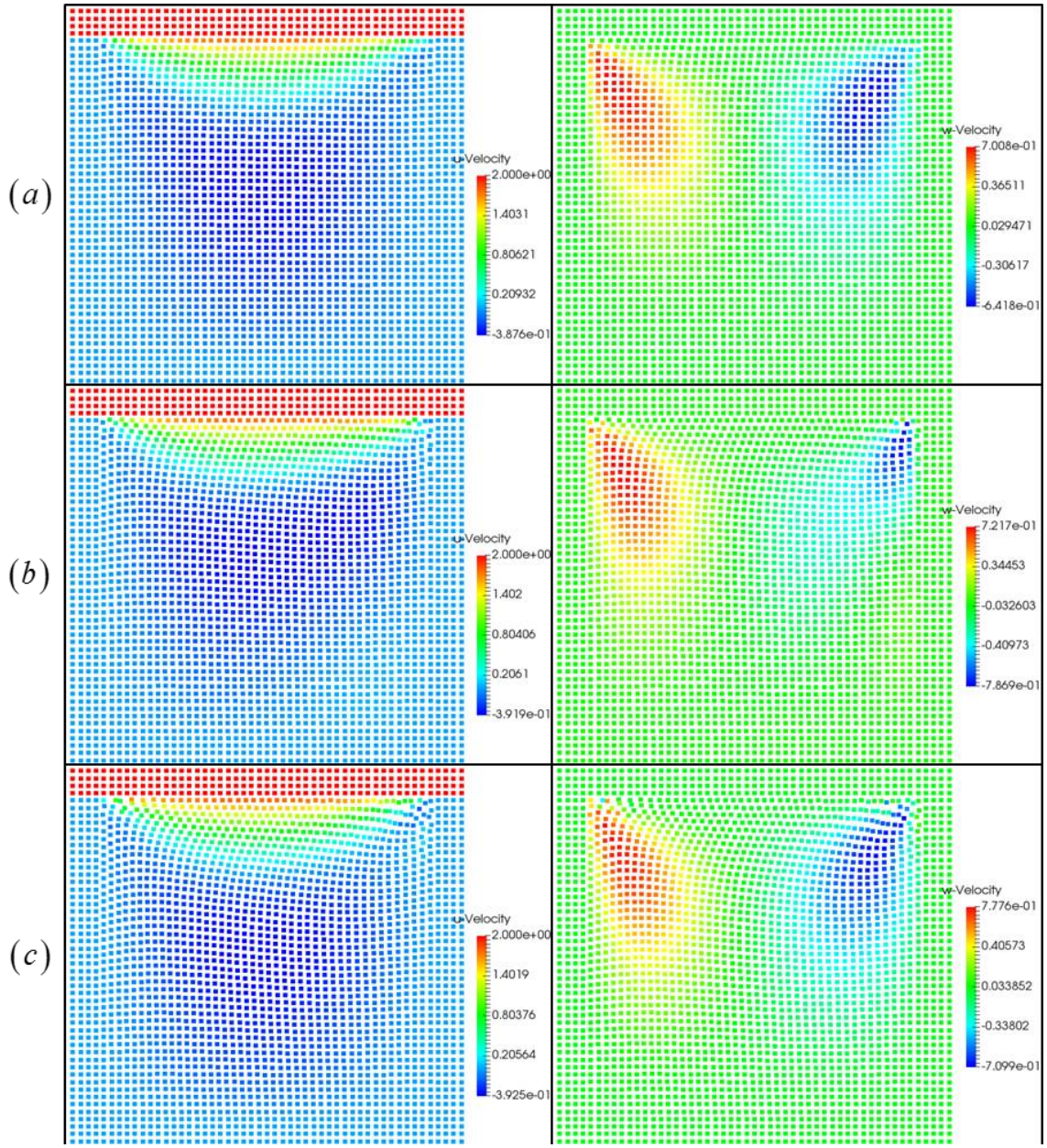

Figure 44 Particle snapshot of lid driven flow inside cavity at $(a)\ t = 0.2t_{fully}$, $(b)\ t = 0.6t_{fully}$, $(c)\ t = t_{fully}$. (t_{fully} represents the time it takes to reach fully developed pattern)

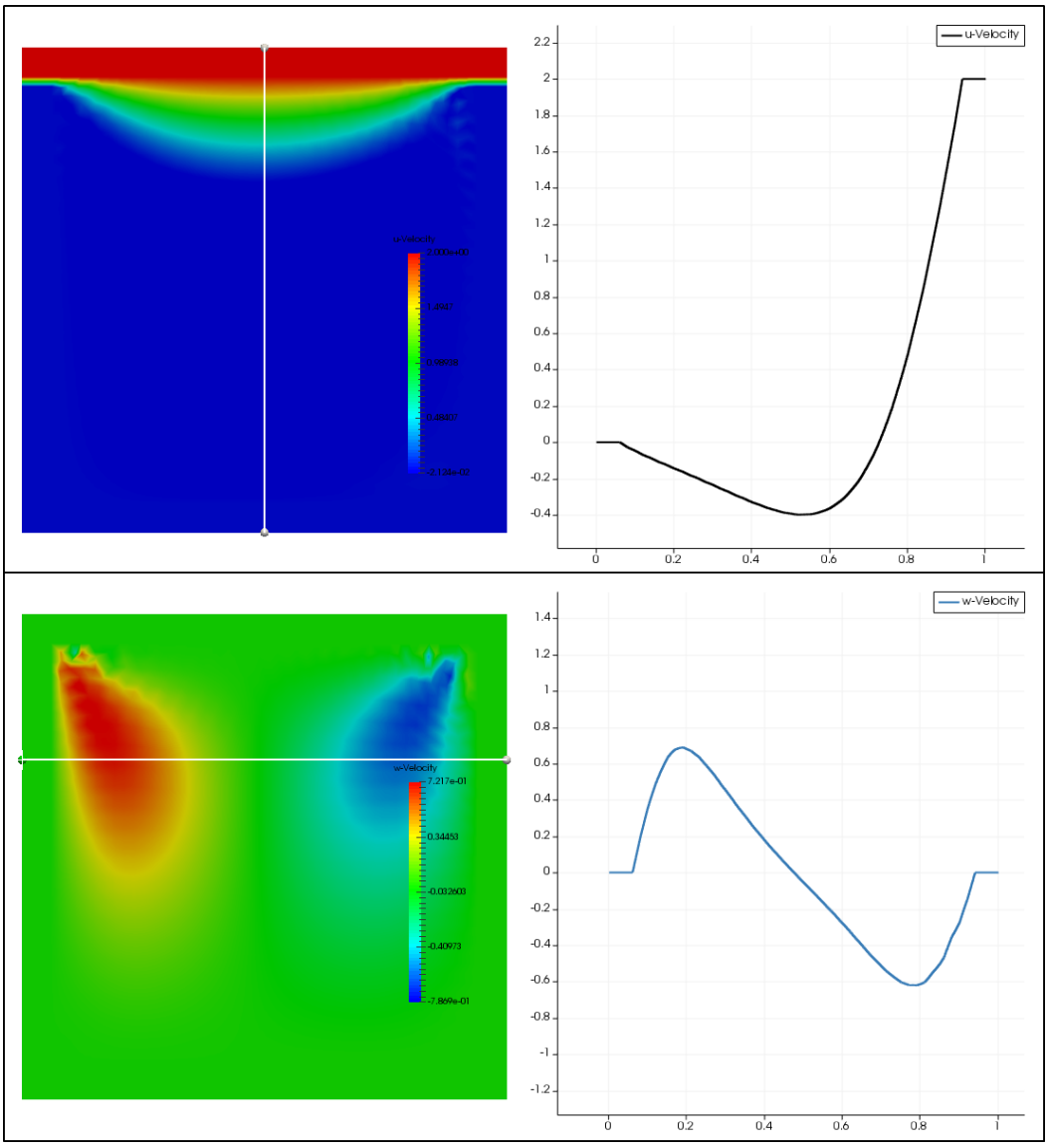

Figure 45 Velocity distribution along vertical center line (top) and along horizontal line at z=0.7 (bottom).

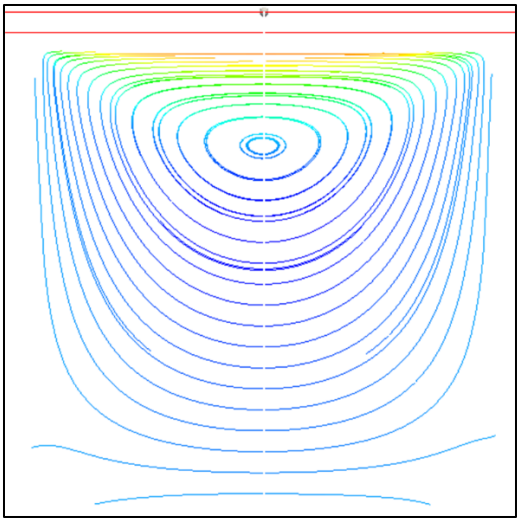

Figure 46 Streamline plot of lid-driven inside an enclosure at steady state

4.3.1. Lid Driven Flow inside Cavity with Remeshing

Although this new method we proposed can provide higher accuracy in calculation of derivative values, we also noticed a fact that this new algorithm does not provide high repulsive force when two fluid particles approaching to each other. This means under certain conditions, SPH particles will stay close to each other or even overlap with each other by using this high order accuracy new scheme. The overlap of fluid particles or higher particles number density in local regions, though has no violation of physics, are not good for a stable numerical simulation. When fluid particles are close to each other at certain location, there will be void region formed at another location when number of particles are fixed during simulation. This void region can induce non-physical results/numerical crash under certain conditions. This issue has been observed even in traditional SPH and methods have been proposed to solve this issue. For example in [65], the authors proposed remeshing method for maintaining the robustness and adaptive of

SPH simulation by projecting physical properties of particles into a better arranged new particle distribution at a fixed frequency. By doing so, errors due to the non-uniform distribution of fluid particles can be reduced which will increase the accuracy and stability of a SPH simulation.

We introduced a different remeshing method to keep the stability of our higher order accuracy meshfree simulation. Instead of remeshing after a fixed number of numerical iterations, we constantly project the fluid properties to uniformly distributed particles (for example initial distribution in our tests).

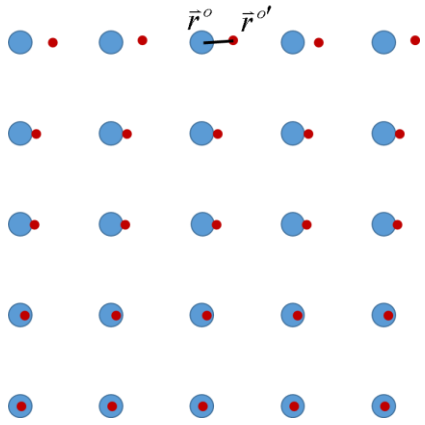

Figure 47 Remeshing to original particle distribution

With a given fluid particle i location ($\vec{r}_i^{\,o}$) and property (ϕ_i^o) at $t = t^o$, we are able to calculate the predicted location ($\vec{r}_i^{\,o'}$) and its corresponding properties $\phi_i^{o'}$ and $\nabla\phi_i^{o'}$ at $t = t^o + \Delta t$ (i.e., the red dots in Figure 47). With small enough time step, $\vec{r}_i^{\,o'} - \vec{r}_i^{\,o}$ is small and the physical properties of the original mesh (i.e., the blue dots in Figure 47) can be

extrapolated from the properties of the red dot position through Taylor series expansion. In summary, the new remeshing algorithm follows flowchart shown below (Figure 48).

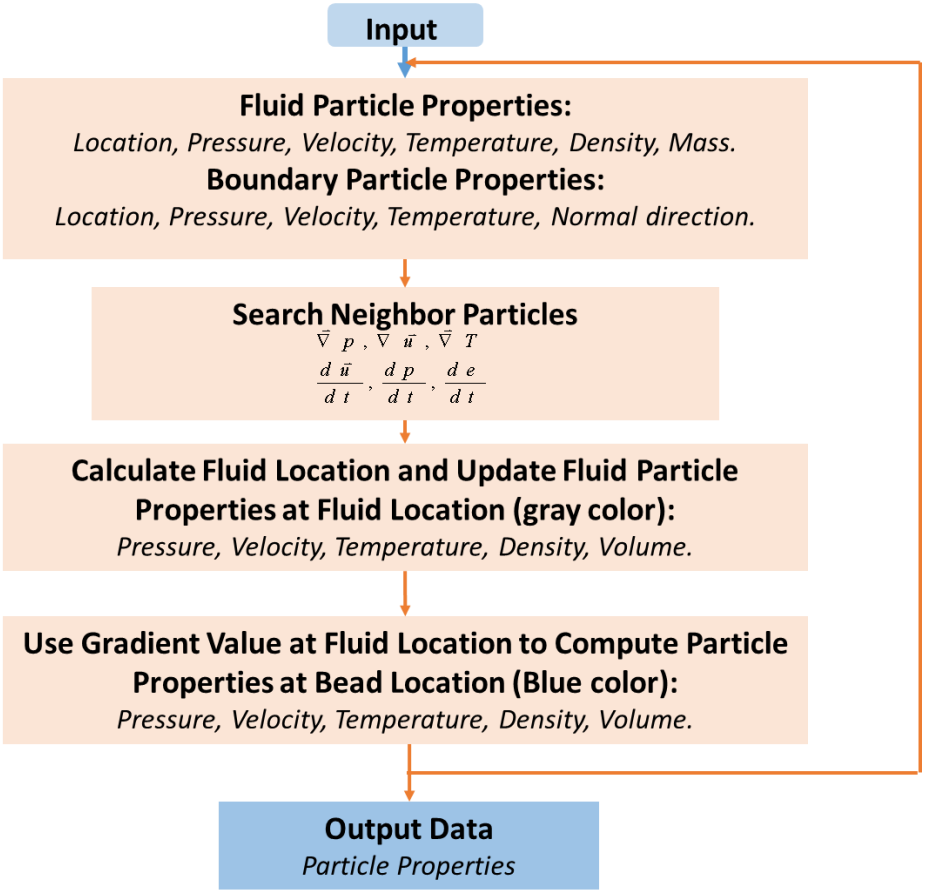

Figure 48 Remeshing algorithm flowchart

With this new algorithm, we redo the lid-driven flow inside a cavity as case 4.3.2. Figure 49 and Figure 50 illustrate the steady state velocity and pressure distributions of the fluid domain with Re=1.0. Figure 51 shows the streamline plot when it is fully developed.

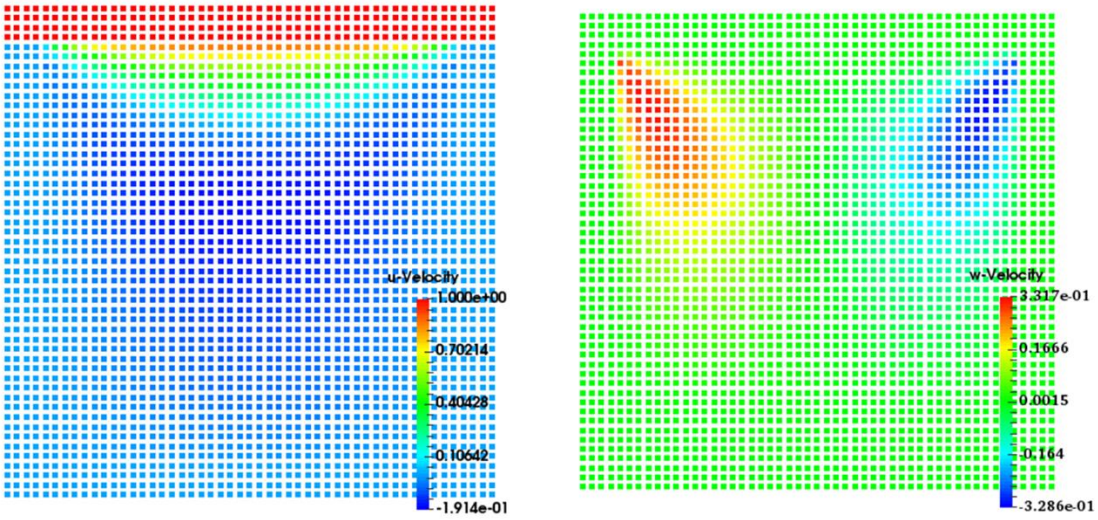

Figure 49 Velocity distribution of lid driven flow inside an enclosure with remeshing after fully developed

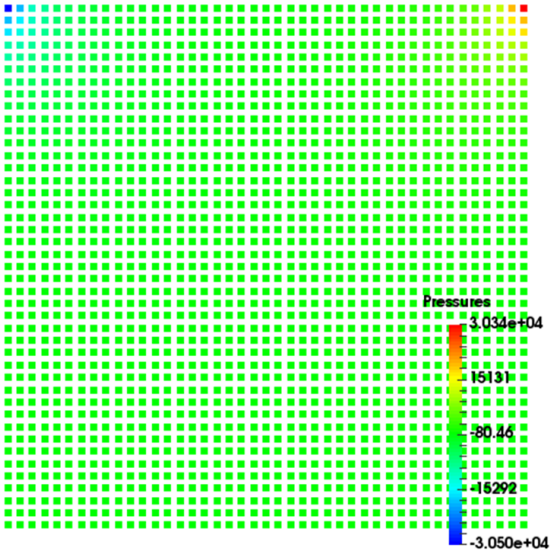

Figure 50 Pressure distribution of lid driven flow inside an enclosure with remeshing after fully developed (pressure smoothing is applied in this figure to filter out numerical noises)

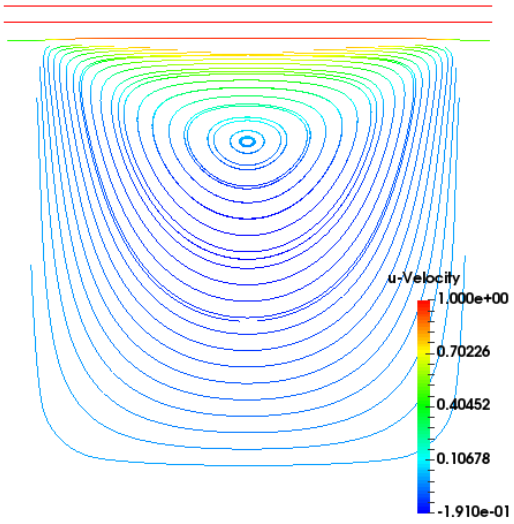

Figure 51 Streamline plot of did driven flow inside cavity with remeshing

We can see the improvement of the velocity distribution with this higher order accuracy scheme with remeshing in smoothness. The transient velocity of the flow field as well as x-velocity profiles along the center vertical line inside the cavity are presented in Figure 52. These transient velocity distributions along the center vertical line at different times are in good agreement with simulation result provide using OpenFOAM [66] (as Figure 53).

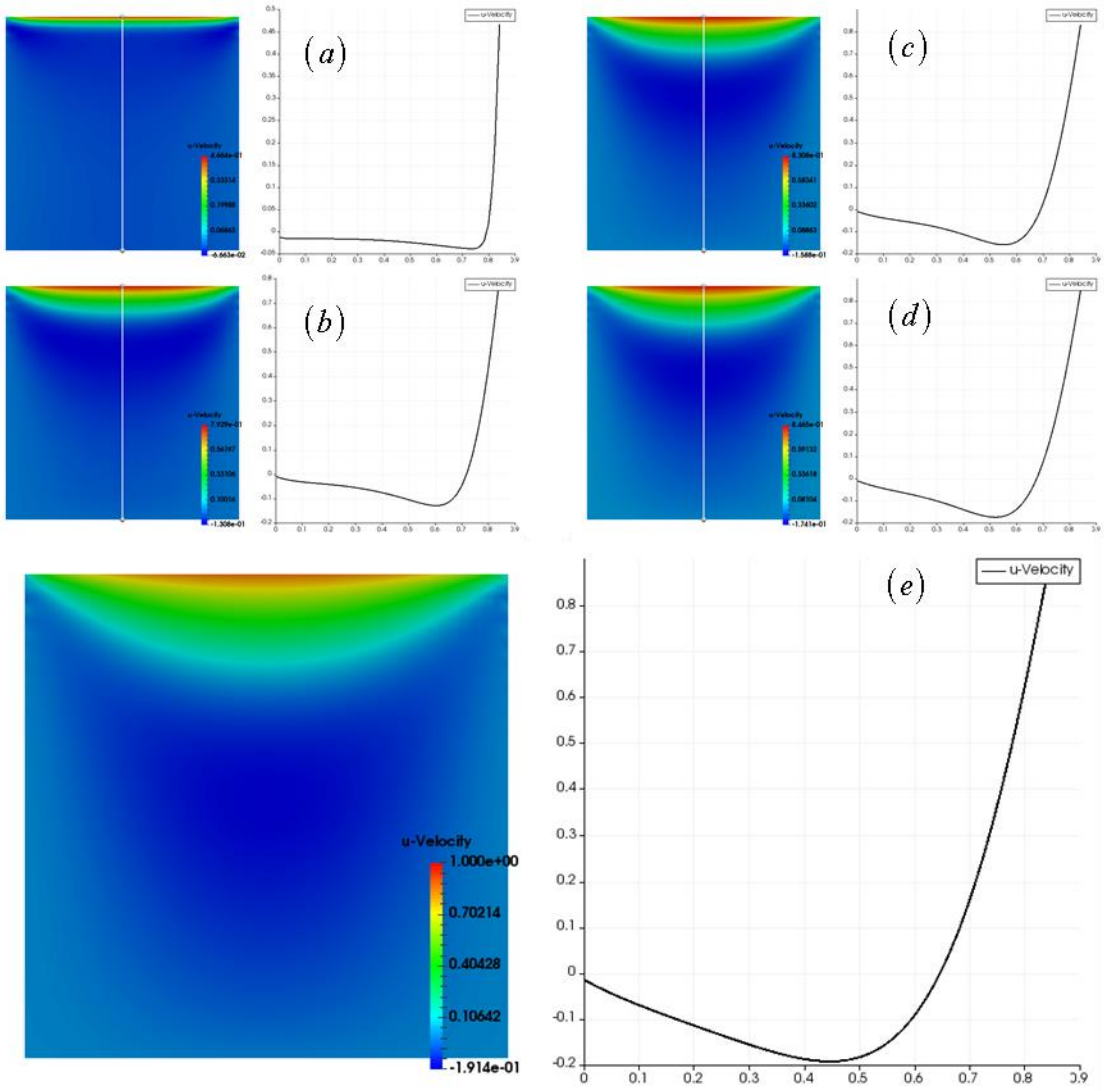

Figure 52 Transient development of lid driven flow inside cavity with remeshing at $(a)t = 0.02 \times t_{full}$; $(b)t = 0.25 \times t_{full}$; $(c)t = 0.5 \times t_{full}$; $(d)t = 0.75 \times t_{full}$; $(a)t = t_{full}$. (t_{fully} represents the time it takes to reach fully developed pattern)

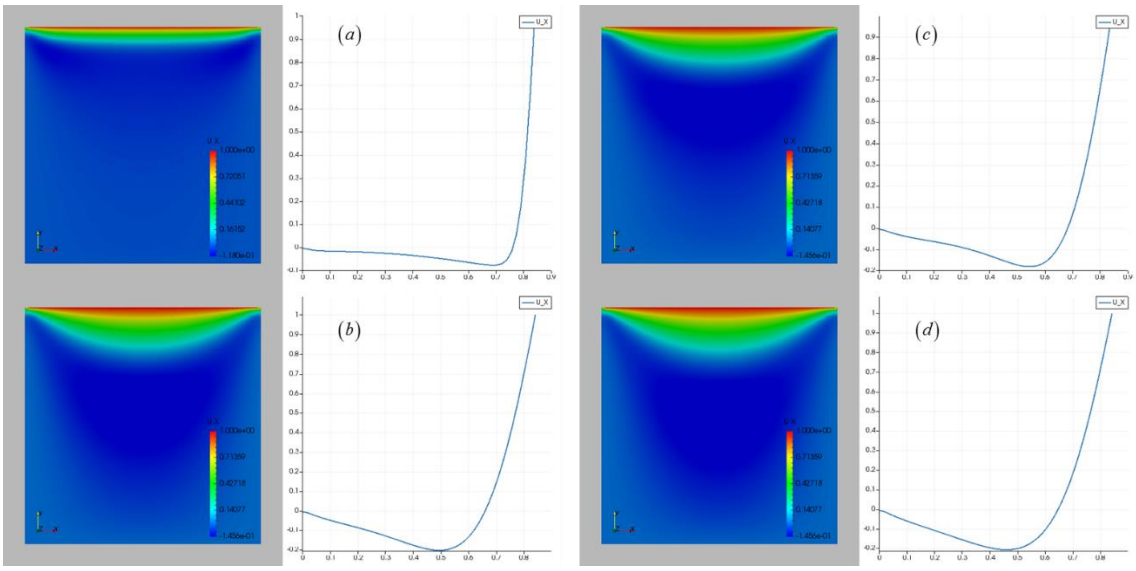

Figure 53 Transient velocity plot of lid-driven incompressible flow inside cavity using OpenFOAM [66] at $(a)t = 0.01 \times t_{full}$; $(b)t = 0.2 \times t_{full}$; $(c)t = 0.5 \times t_{full}$; $(d)t = t_{full}$. (t_{fully} represents the time it takes to reach fully developed pattern)

4.4 Conclusion

A high order accuracy meshfree scheme is introduced in this section. With this novel scheme, zeroths and first order truncation errors during derivative calculations are cancels through a Taylor series method. As a result, this new scheme can ensure 1st and 2nd orders of accuracy in gradient and Laplacian calculation. When the particle distribution is symmetric, the orders of accuracy can be even higher based on the selection of weight function.

In this new scheme, we solve the 1st and 2nd derivatives of the physical properties simultaneously by splitting the supporting domain with respect to the x = 0 and y =0 planes (also z =0 plane for 3D cases). The numerical algorithm applied in this section calculates pressure increment for each iteration based on modified mass conservation equation

coupled with equation of state. The density of the fluid is update at each time step with the calculated pressure value and the equation of state.

Couette Flow and Lid-Driven Flow are selected as the benchmark cases to verify this high order accuracy meshfree scheme. The results showed agree with analytical solution for Couette flow and incompressible flow solution with OpenFOAM for the lid-driven flow.

With this new meshfree numerical scheme, fluid particle can be very close to each other which is closer to real physics compared with traditional SPH. However, this particle agglomeration at A location implies formation of void regions at B locations if the numerical of fluid particle during the meshfree simulation is fixed. Void region cannot be handled mathematically with our new scheme which will finally induce non-realistic results or crash. To solve this issue with the new scheme, we applied remeshing method which project property distributions back to a uniform particle distribution. By doing so, our algorithm can provide stable and smooth results of the simulated physical properties under benchmark cases when boundary layer flow is important (e.g., the lid driven case).

5. LASER INDUCED LIQUID EJECTION *

5.1. Theory and Background of LIEB

5.1.1. Review of Experimental Studies on LIEB

As we discussed in Section 1.1, LIEB has attractive advantages compared with traditional heating methods. Numerous studies have been done in order to better understand the LIEB phenomenon. Experimental observation of the LIEB process is the first step to understand this complex physical process. Early experimental researches focused on LIEB at the surface of a liquid/solid domain as well as the associated liquid ejection process. For example, Yasuyuki et al. resolved jet formation and dynamics of liquid jet generated during UV laser induced explosive boiling in 1995 with nano-second laser imaging [67]. S.I. Kudryashov and S.D. Allen also studied the dynamics of vapor bubble in water during LIEB on a silicon wafer surface with high speed imaging in 2006 [68]. Later researches also investigated micro/nano-bubble formation and shock wave emission during and after LIEB inside a liquid domain without the presence of solid. For example, I. Apitz and A. Vogel [69] studied LIEB process of water and soft tissues (such as liver and skin) induced by ns Er:YAG laser in 2005. It is concluded in previous experimental results that LIEB involves with processes including (a) laser-solid interaction and heating, (b) cavitation/bubble formation, (c) bubble expansion, (d) bubble collapse and rebound. When LIEB is induced in a pure liquid domain, the LIEB is composed with (a) optical absorption in liquid through linear or cascade ionization, (b)

*Reprinted with permission from "Laser Induced Nano-Droplet Ejection for the Construction of Nano-Inkjets", by Yu Yang, Vijay M. Sundaram, Alok Soni and Sy-Bor Wen, IMECE2012-87747, Copyright 2012 by ASME.

phase change and vaporization of the liquid, (c) bubble formation and explosion. In this study, we interested in non-bio applications and focus on the LIEB at the liquid/solid interface.

5.1.2. Review of Theoretical Analysis on LIEB

Compared with the experimental study, theoretical analyses of LIEB are limited to simple situations with lower dimensions. For example, atomic-level MD simulations [70, 71] were applied in inter-molecular energy redistribution analysis inside a semi-infinite 2D molecular system during a LIEB with time step around fs level. Regarding large size domain with long time durations, coarse grained breathing sphere MD model by assuming grouped atoms as one simulation bead was also adopted by Leonid V. Zhigilei et al. in 1997 [72, 73] to study material ejection by LIEB induced high pressure. Macroscale Numerical studies based on continuous governing equations have also been done by S.N. Andreev et al. [74] in 2007 to determine the correlation between laser conditions and evaporation kinetics, which showed a qualitative consistency with the MD simulation done by Yusheng Dou et al. [75] in 2001. The higher order accuracy meshfree method presented in Section 4 has the potential to simulate this LIEB process with high accuracy.

5.1.3. Applications of LIEB

Based on the experimental/theoretical analyses [76, 77] of LIEB, high pressure vapor bubble and the resulting shock waves in the liquid domain are commonly observed in LIEB. The high-pressure vapor bubble and the high-pressure shockwave during a LIEB can be applied as microscale higher pressure supplier. For example, the thrust force from LIEB was applied as removing force for laser cleaning, micro-pump in inkjet printing

systems, “knife” in micro-machining [1]. In this study, we will focus on the LIEB applications in inkjets for micro-nano fabrications. One of the few examples of the applications is Laser-induced forward transfer (LIFT) which use a laser beam to transfer a thin film to a substrate through liquid instability induced by LIEB generated liquid vaporization and shock wave. LIFT was successfully demonstrate by Bohandy et al. in 1986 [78]. By controlling laser energy and the beam profile, printing pattern can be controlled with micrometer precision for micro-fabrication. In 2000s, LIFT was also introduced to transfer biomolecules onto a bio-substrate, which was known as biological laser printing [79].

5.2. Introduction of Laser Driven Non-Contact Inkjet Printing

As discussed in 3.1.3, LIEB generate high pressure within a short time period can be used as microscale pumping forces used in inkjet systems. Currently, Inkjet techniques are used in high-resolution and high volume printing [80] since 1990s. Several inkjet methods were defined based on the jet dynamics such as spray plating, continuous inkjet printing, and drop-on-demand printing. Inkjet printing methods are also divided into different groups based on their drivers such as piezoelectric actuator, micro electric heater, and acoustic modulate inkjet printing (as Figure 54).

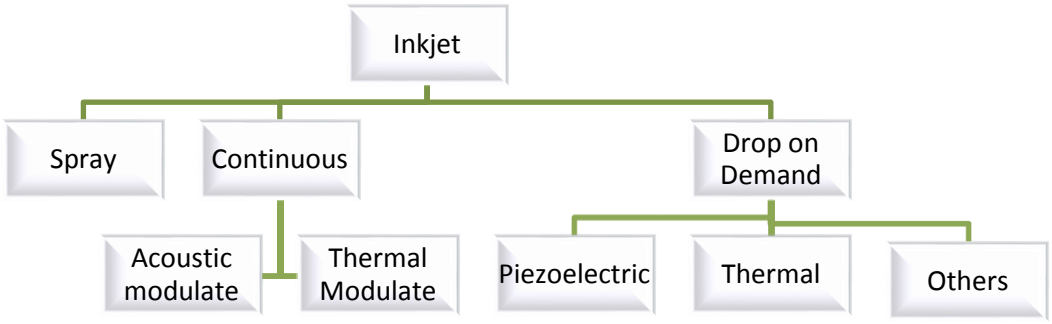

Figure 54 Fundamentals of inkjet printing technologies

5.2.1. Theory and Background of Inkjet

A liquid jet coming out from nozzle with a radius will lose its original cylindrical shape and break up into droplets or sprays. Based on the applied pressure to the nozzle of inkjet, the fluid can eject from the nozzle with different exit velocity. The exit velocity determines the dominant hydrodynamics instability during the droplet formation. For low driving pressure and associated low exit velocity of this fluid, a liquid jet with diameter similar to aperture size of nozzle can be formed. This low velocity liquid jet coming out from nozzle can be explained by Plateau-Rayleigh instability theory which provides the thread of fluid breaking up into droplets in order to minimize the surface energy [81, 82]. The theoretical analysis is presented in next section.

5.2.1.a. Plateau-Rayleigh Instability Theory

For any surface between two fluids (for example background gas and liquid water) with r_1 and r_2, Young-Laplace equation can be used to described the hydrostatic pressure increment as:

$$\Delta p = \sigma \left(\frac{1}{r_1} + \frac{1}{r_2} \right)$$ **Equation 71**

where, σ is the surface tension and r is radius of the liquid jet/droplet. Then, the hydrostatic pressure of liquid drop can be expressed by assuming $r_1 = r_2$ as:

$$\Delta p = \frac{2\sigma}{r}$$ **Equation 72**

In a liquid cylinder with radius of r_l and a perturbation curvature r_p (shown in Figure 55), applying Bernoulli's Theorem at cross-sections A and B with radius r_{la} and r_{lb}.

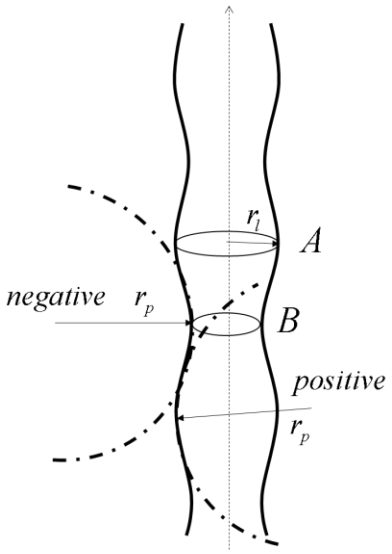

Figure 55 Schematic of liquid cylinder disturbance

$$\frac{1}{2}\rho u_A + \rho g z_A + P_A = \frac{1}{2}\rho u_B + \rho g z_B + P_B$$

$$P_A \approx P_0 + \frac{\sigma}{r_{la}} \qquad \textbf{Equation 73}$$

$$P_B \approx P_0 + \frac{\sigma}{r_{lb}}$$

with P_0 represents the ambient pressure. Then, we are able to find:

$$\frac{u_B}{u_A} = \sqrt{1 + \frac{2}{Fr}\frac{(z_B - z_A)}{r_{la}} + \frac{2}{We}\left(1 - \frac{r_{la}}{r_{lb}}\right)}$$

$$Fr = \frac{u_A^2}{g r_{la}} \qquad \textbf{Equation 74}$$

$$We = \frac{\rho u_A^2 r_A}{\sigma}$$

From the conservation law: $\pi r_{la}^2 u_A = \pi r_{lb}^2 u_B$, we are able to find the radius correlation between cross-section A and cross-section B as equation below.

$$\frac{r_{la}}{r_{lb}} = \frac{u_B}{u_A} = \left[1 + \frac{2}{Fr}\frac{(z_B - z_A)}{r_{la}} + \frac{2}{We}\left(1 - \frac{r_{la}}{r_{lb}}\right)\right]^{1/4} \qquad \textbf{Equation 75}$$

Assume the pressure inside the liquid jet with initial radius can balance the normal pressure with surface tension, then it gives:

$$P_0 = \frac{\sigma}{r_0} \qquad \textbf{Equation 76}$$

The perturbation wave induced radius change along the liquid jet can be expressed as a wave function as:

$$\tilde{r} = r_0 + \varepsilon e^{\omega t + ikz} \qquad \textbf{Equation 77}$$

where ε is the perturbation amplitude which is smaller than r_0, ω is the growth rate of instability and k is the wave number along gravitational direction. The wavelength of perturbation can be expressed as $2\pi / k$.

Substituting the pressure, velocity and radius into the Navier-Stokes equation, the dispersion relation of linear stability of low viscosity fluid can be derived to indicate the dependence of growth rate on the wavenumber:

$$\omega^2 = \frac{\sigma k}{\rho r_0^2} \frac{I_1(kr_0)}{I_0(kr_0)} \left(1 - k^2 r_0^2\right)$$

where, I is the modified Bessel function of first kind.

5.2.1.b. Four Regimes of Jet Breakup

The complexity of jet breakup process is due to the effecting parameters, such as physical properties of liquid and background gas, fluid velocity coming out from nozzle, and the geometry of the nozzle. Grant and Middleman [83] reported "breakup curve" of low speed Newtonian liquid in 1966 (as Figure 56). In the general breakup curve plot, section ABC with a low velocity (smaller than v^0) correspond to the single droplet coming out from nozzle without definable breakup length. The linear region CD can be described by Weber's analysis [84] for the liquid jet breaking due to the surface tension only. The shape of breakup curve beyond point E is not explained clearly by Grant and Middleman, they agree with most scholars that the jet breakup length at first increase linearly with velocity increase and reaches the maximum and then decrease.

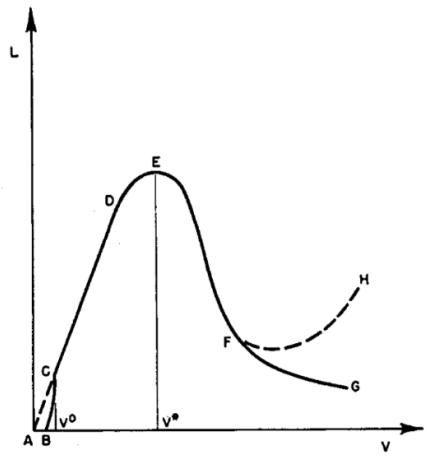

Figure 56 Grant and Middleman's general shape of breakup curve, reprinted with permission from [83]

Figure 57 [85] shows four regimes of jet breakup reflecting the jet changes in breakup length. Typically, when a liquid flow through a smooth nozzle into air, the four regimes can be observed as:

1. Rayleigh jet breakup, which occurs when the liquid flows down from nozzle and liquid jet break up mainly due to the surface tension force. The drops formed in this regime are slightly larger than the size of nozzle.
2. First wind induced breakup regime, which occurs when the liquid flowing down from nozzle with droplet size of the similar to the jet diameter. The breakup is dominated by static pressure as well as surface tension.
3. Second wind induced breakup regime, which occurs also when liquid flow downward and produce drops smaller than jet diameter. The formation of droplets are mainly due to the growth of surface wave which is opposite to the surface tension.

4. Atomization regime, which forms droplets which are much less than nozzle size (i.e., spray).

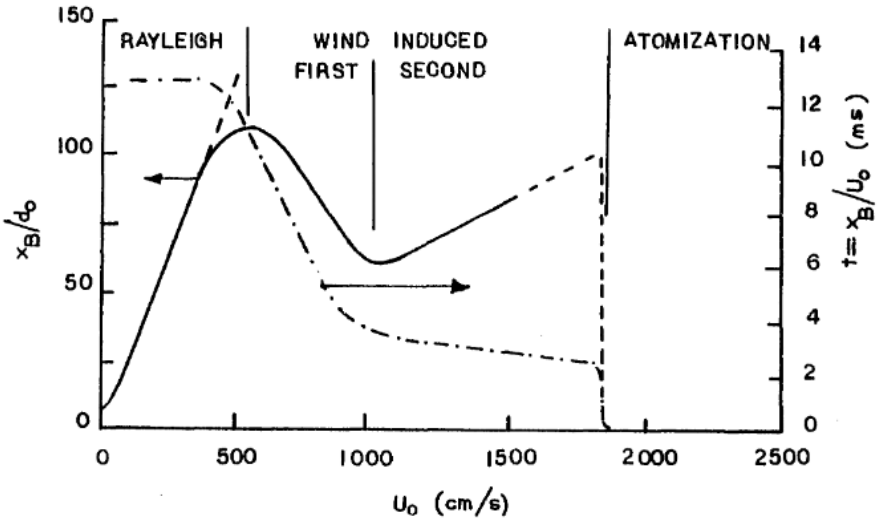

Figure 57 Breakup curve of water coming out from a nozzle (D=0.05cm) in to air background at 295K, reprinted from [85]

Based on previous experimental tests, for the same liquid material coming out from the same nozzle, breakup of liquid jet is highly depending on the velocity coming out of the nozzle. Therefore, the controlling of liquid velocity coming out from the nozzle is the key factor for the precise controlling of inkjet printing.

5.2.2. Applications of Inkjet in Micro-Fabrication

Micro/nano electrical/optical devices are commonly fabricated with layer-by-layer techniques through either bottom-up or top-down approaches. These layer-by-layer micro-manufacturing techniques allow high volume fabrication with low cost. However, there are situations when the layer-by-layer approaches not appropriate. For example, biologically active functional materials is challenging to go through most of the lithograph

or deposition process requiring different corrosive chemicals and/or a vacuum environment. Also, layer based techniques are material and time consuming in low feature density fabrication (e.g., fabrication of a few standalone structures in a large area) or fabrication of structures requiring an assembly of large number of layered processing. To solve these issues, direct writing (DW) has received significant attention in the last decade. Direct writing (DW) is also known as direct printing which can create 2D/3D features on a substrate by precisely controlling the positions of patterning head(s). DW includes a diverse group of process techniques (e.g. droplet based DW, dip-pen lithography and focused ion beam DW). Among these DW techniques, inkjet-based DW features with its fast generation of a standalone or large area structures on 2D or 3D surfaces through depositing sequence of droplets on the target. Inkjet based DW has become one of the standard in fast prototyping of micro and macro structures based on the given blueprints.

In addition to the fast processing speed, DW with inkjet printing also provides several benefits: 1) Inkjet techniques only deposit materials where it is desired. For example, if the amount of area required to be covered is small compared to the total area, the saving of rare/expensive materials can be significant and it is more environmental friendly. 2) Inkjet printing can reduce the interaction among different materials during deposition due to the noncontact feature. In other words, it can deposit materials on sensitive/unstable surfaces without destroy of the surface structure. It can also be applied on non-flat surfaces for 3D features' construction [86, 87]. 3) Inkjet printing has high flexibility in adjusting the outcomes through a software programming to assign the trajectories of the print head of the inkjet.

5.2.3. Limitations of Current Inkjet Technologies

Current inkjet methods mainly rely on thermal electric heater and piezoelectric actuator as the driving force, and can provide resolution less than 10 μm. This resolution, however, is not enough in many advanced micro fabrication requiring few micron to sub-micro scale resolution. To achieve the higher resolution, new inkjet methods such as electro-hydrodynamic jet printing [88] and dynamic mode AFM tip droplet deposition [89] have been proposed and can achieve resolution <10 μm or even nano-meter scale.

However, these newly proposed techniques are limited for deposition of ionized ink materials on conductive substrates. To solve the issue, we push the limit of tradition thermal inkjet from 10s μm to a few μm (or even submicron). To achieve the goal, both the channel and pressure supply of a thermal inkjet should be reduced and be well controlled during printing process. While micro/submicron-scale fluidic channels and nozzles are available [90], available pressure suppliers based on traditional thermal and piezo-electric schemes cannot provide both μs (or even sub-μs) pulsed duration and 10s of Mbar pressure to overcome the surface tension of liquid at micro (or sub-micro) scale . Therefore, a new pressure driver through optically induced pulsed heating i with a combination of pulsed laser and nano-optical devices is proposed in this study. The new optically induced pressure driver is coupled to a micro/submicron nozzle to generate confined heating and then explosive boiling and ejection of ink from the nozzle.

5.3. Laser Induced Micro-Droplet Ejection

The third part of this study is motivated by the fact that high pressure can be generated by LIEB with laser. This high pressure, which is orders higher than that from a piezo-electric actuator and thermal heaters, can be used to establish inkjets providing sub-micron scale droplets. The concept of utilizing LIEB in constructing laser inkjets is illustrated in Figure 58 and Figure 59. For continuous laser inkjet illustrated in Figure 58, three main physical mechanisms happen in a sequence as (a) a laser beam is delivered to tapered metal micro nozzle, (b) localized confined heating is induced by laser which can induce explosive boiling, (c) higher pressure vapor from LIEB expands and pushes liquid out with high velocity and form spray. For construction of drop-on-demand laser inkjet illustrated in Figure 59, similarly, three main physical mechanisms happen in a sequence for ink ejection as (a) a pulsed laser light is delivered to the nozzle and induce confined heating, (b) localized heating and vaporization of liquid layer forms bubble on the surface, (c) high pressure bubble expands and pushes liquid droplet out from the nozzle aperture, (d) vapor bubble collapse and ready for next drop on demand ejection.

To construct the required metallic micro nozzle for the laser inkjet with LIEB, we prepared tapered glass pipette with both inner wall and outer wall metal coating as the metal micro nozzle in [91] [92]. These micro nozzles are used to experimentally test the non-contact laser inkjet with LIEB. Detailed fabrication procedures of the micro-nozzle and experimental setup to verify the LIEB driven non-contact inkjet are discussed in the following sections.

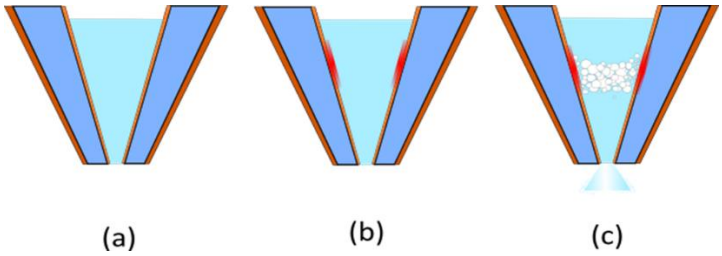

Figure 58 Proposed mechanism for continuous spray

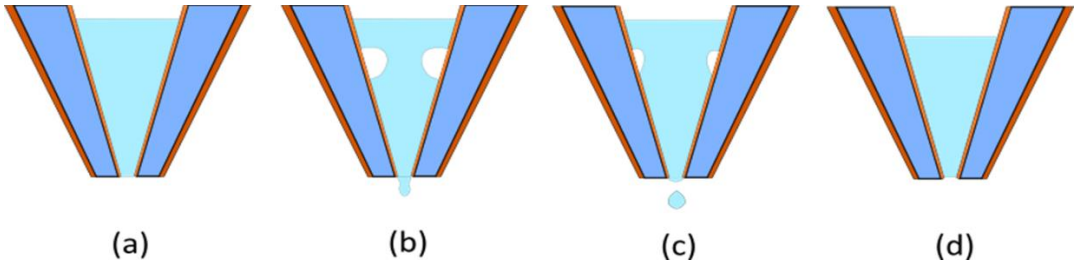

Figure 59 Proposed mechanism for drop on demand ejection

5.4. Fabrication of Micro-Nozzle

We used following fabrication procedures to construct a tapered hollow glass pipette with both inner wall and outer wall metal coating to serve as the metal micro nozzle in the LIEB laser inkjets.

To coat the inner wall of glass pipette, we used continuous flow electro-less plating (CF-EL) methods [93] and the setup was presented in Figure 60. In the CF-EL method, electro-less Au plating solutions were injected into the capillary through a micro syringe (500F-GT 500uL syringe, SGE Analytical Science) driven by syringe pump (NE300, New Era Pump System Inc.). The chemical liquid used for the EL plating is 6:1 volume rate mixture of gold ion solution (0.024M tetra-chloro auric acid ($HAuCl_4$), 0.75M sodium hydroxide (NaOH), and 0.086M sodium chloride (NaCl) in water) as well as reduction

agent (0.5vol% glycerol ($C_3H_8O_3$) in water). After deposition, to get a better idea of the Au plating properties, SEM (Figure 61) image was taken after cutting pipette into pieces.

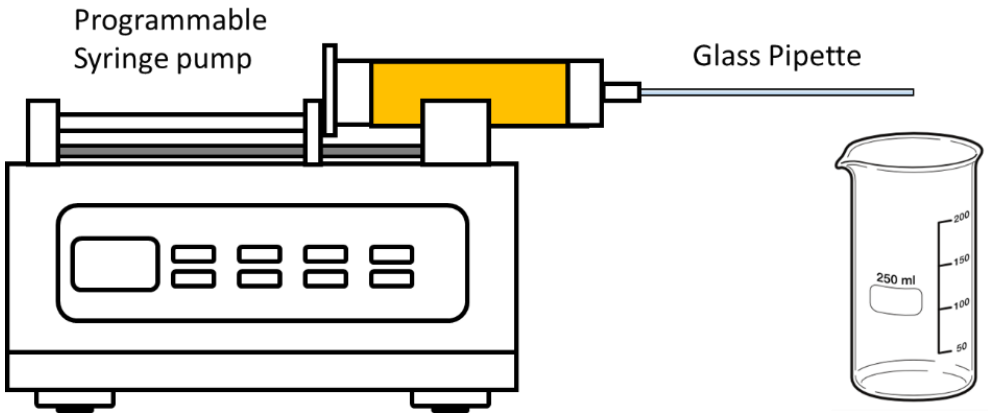

Figure 60 Experimental setup for CF-EL plating

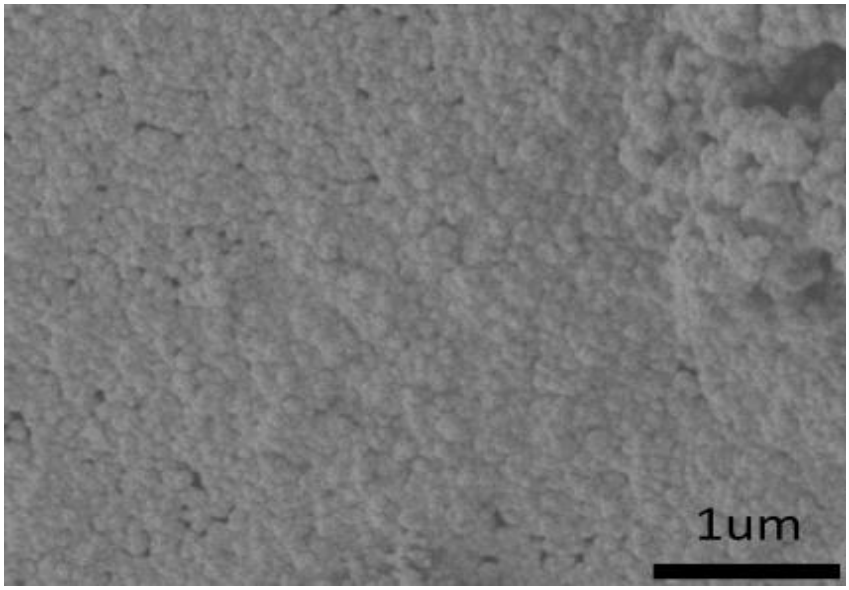

Figure 61 SEM image of CF-EL plating

After inner wall coating, the tapering of the pipette is achieved with a Sutter N-87 Flaming/Brown micropipette programmable puller. Figure 62 shows the optical image of tapered pipette tip with inner wall coating. The tip diameter is checked by SEM image and demonstrated to be less than 1 μm.

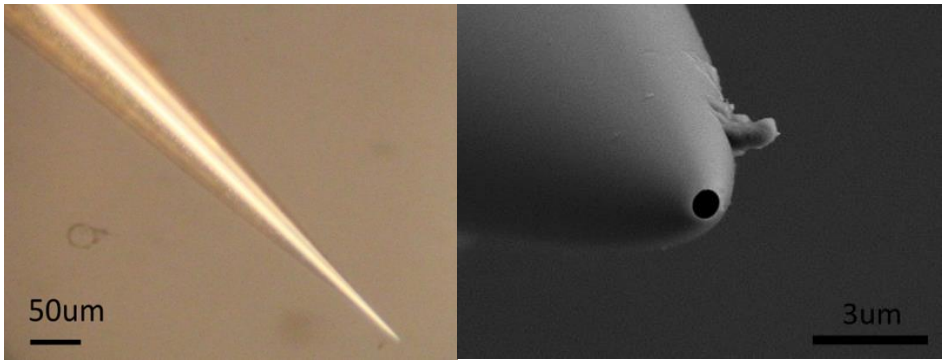

Figure 62 Optical (left) and SEM (right) images of tapered pipette

To get a confined heating from the nozzle, outer wall metal coating is also needed in our system. In order to deposit thin and uniform metal layer outside nozzle, E-beam deposition was utilized (shown as Figure 63). Nozzle was mounted and maintain a constant rotation speed inside deposition system.

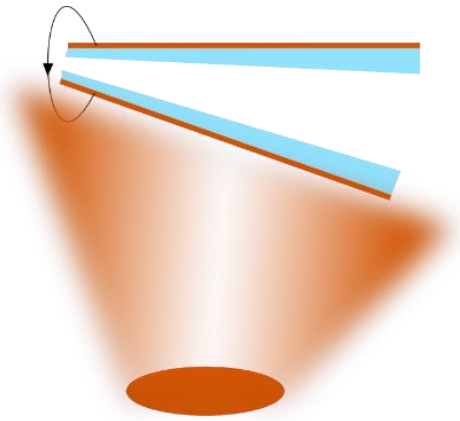

Figure 63 E-Beam deposition on the outer wall of nozzle

To operate the metal coated hollow glass pipette as the micro nozzle in the laser driven inkjets, separation distance between nozzle tip and substrate needs to be precisely maintained. To maintain the separation distance, the force feedback with micro tuning fork which is used in NSOM (Near-Field Scanning Optical Microscope) scanning system is adopted here. In this method, the fabricated micro nozzles were attached to tuning forks purchased from Digi-Key with DYMAX glue (as Figure 64). Then tuning fork can be mounted on the 6-axis piezo-motor stage controlled by the feedback loop of a scanning probe system (NW2000 from nanononics.com) providing ~10 nm x-y-z resolution.

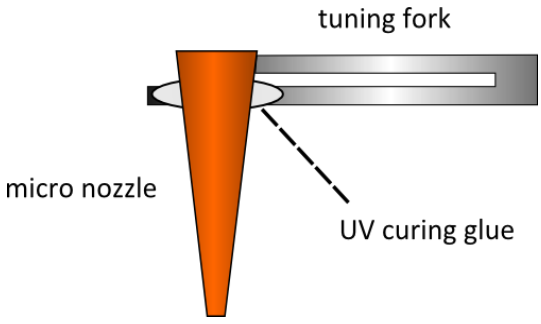

Figure 64 Mounting nozzle on tuning fork

5.5. Experimental Setup

To test the functionality of the metal coated hollow glass pipette as the micro nozzle in the laser driven inkjets, we integrated these nozzles in a scanning probe system and coupled with different laser light as illustrated in Figure 65. Upright microscopy in Figure 65 was adopted not only to couple laser light to the micro metal nozzle through high numerical aperture objective, but also used to take optical image of micro droplets after the experiments. In order to maintain a consistent laser coupling conditions during experimental studies, self-constructed side microscopy was applied which can observe the laser light coupling from tip light emission as well as visualize separation distance between nozzle tip and substrate surface.

In this study, multiple laser conditions (e.g. continuous laser, ns pulsed laser, μs pulsed laser) were tested. Laser spot with a diameter same as entrance size (~400μm) of the nozzle was delivered to the nozzle entrance through a 10X objective lens.

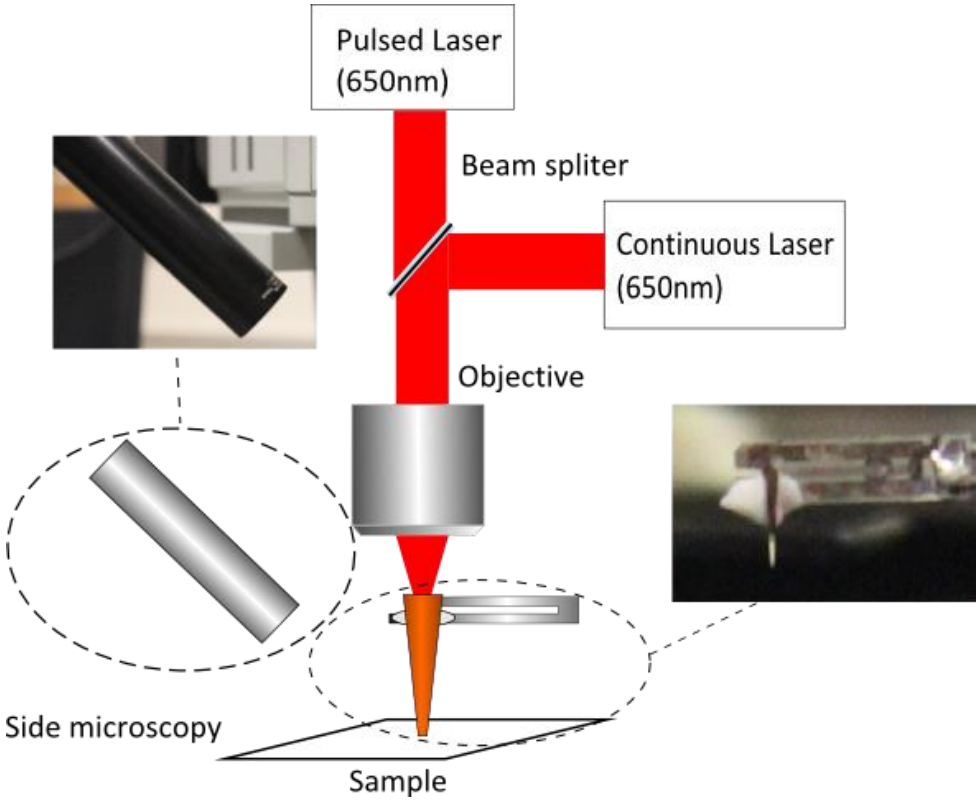

Figure 65 Experimental setup

5.6. Results and Discussion

5.6.1. Spray Generation from Continuous Laser

The nozzle was first coupled with a continuous laser of λ~650nm. In this study, pure glycerol was used as the ink material. To fill the nozzle with ink materials, micro-nozzle was first immersed in ink materials for 30 min. Two different input laser powers, namely, 0.6 mW and 1.1 mW were examined. Figure 66 and Figure 67 shows the optical images of the micro-spray generated on the surface of a clean silicon wafer when the incident laser power is ~0.6 mW and ~ 1.1mW.

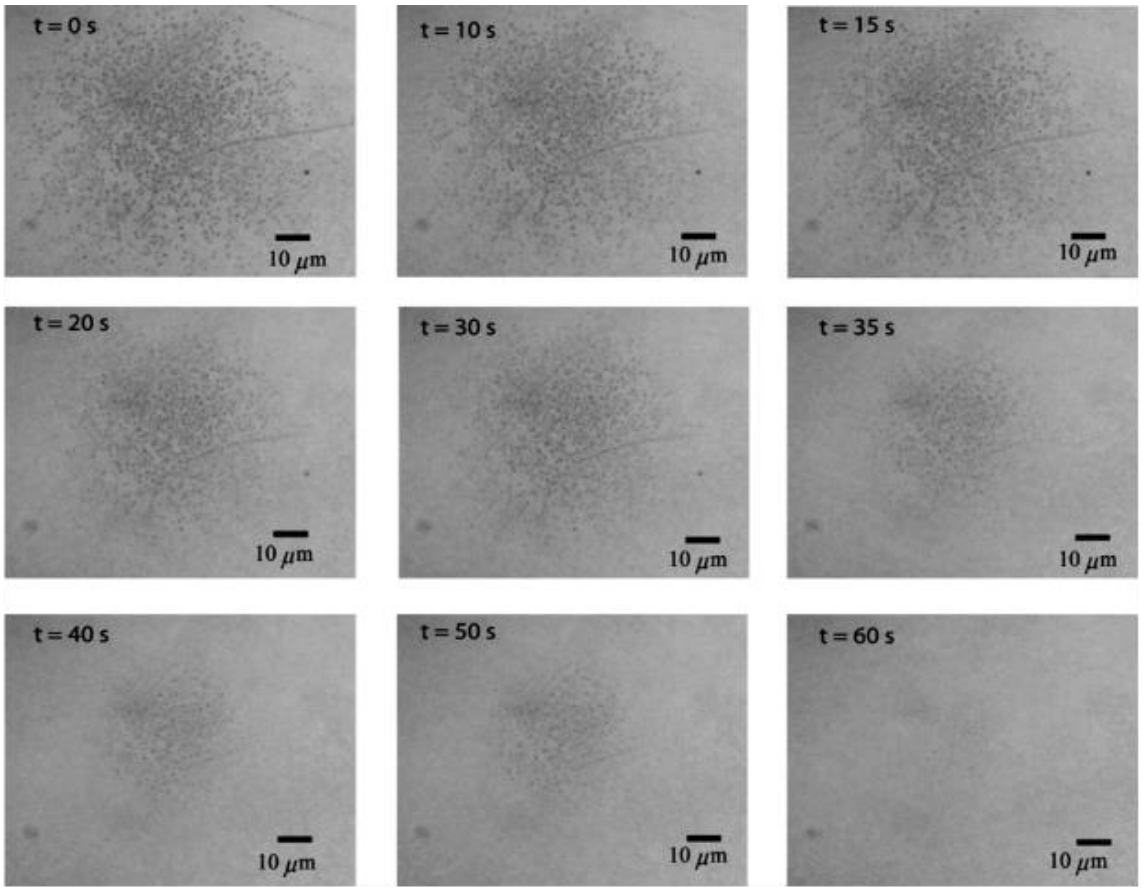

Figure 66 Optical microscope image of nano-spray deposited on silicon wafer under input laser power of 0.6 mW. The sequence of images are taken at different times after the experiment was conducted

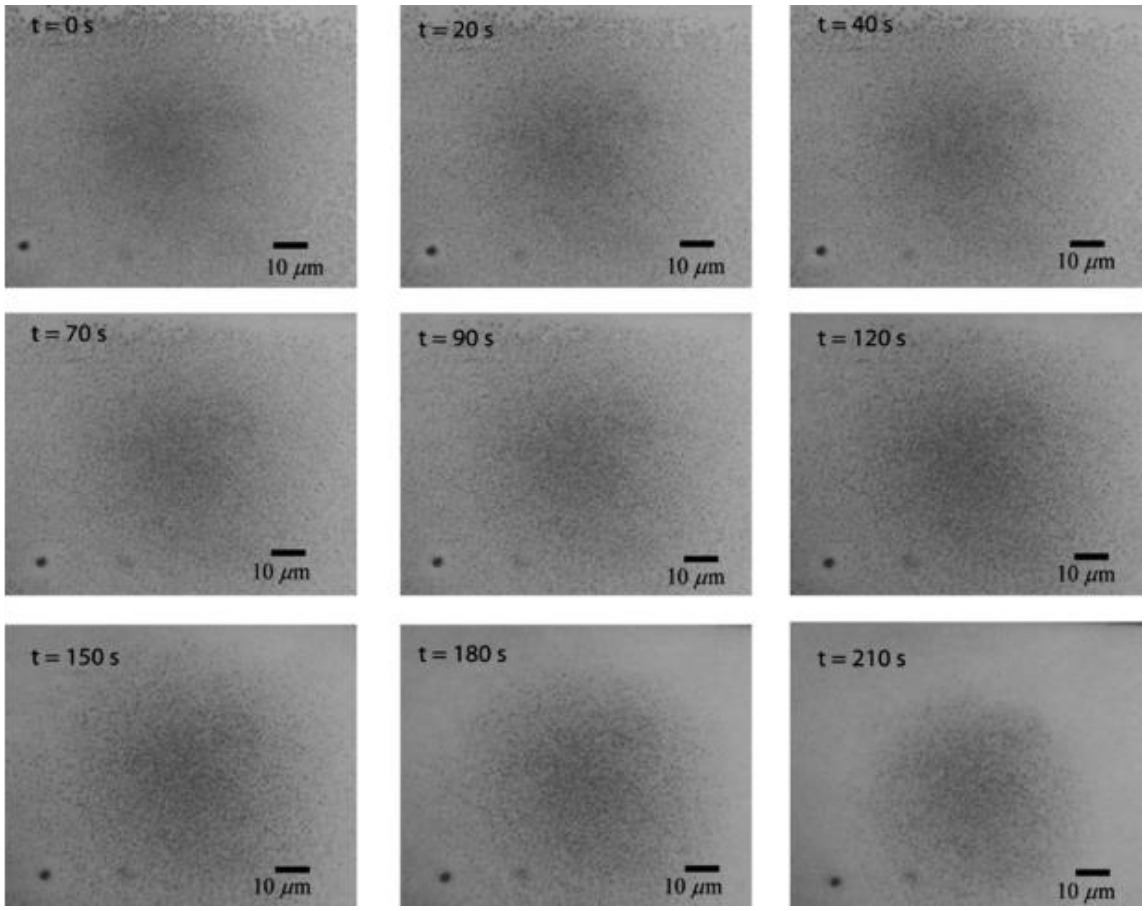

Figure 67 Optical microscope image of nano-spray deposited on silicon wafer under input laser power of 1.1 mW. The sequence of images are taken at different times after the experiment was conducted.

The high pressure induced by explosive boiling squeezed ink materials out from micro nozzle and form liquid jets. The velocity of liquid ejection is high enough to break the liquid jets into droplets which are much smaller than the aperture size. The droplets are deposited on the substrate after atomization process. After generating the spray, we can clearly observe the droplet evaporation and disappearance after few minutes. The region of the target covered with the spray is more confined with the lower laser power. Continuous laser with high enough intensity always provides a large spray composed with

micro/nano scale droplets from the nano-nozzle. The spray evaporates in 1-2 hr. after the experiment. The composition of the evaporable spray from the high energy continuous laser can be by product of the oxidation of glycerol. As discussed in [94], a large variety of products can be generated during the oxidation of glycerol such as DHA, Glyceraldehyde, Glyceric acid, Hydroxymethyl glyoxal etc.. Some of these by products are not stable under the common condition. Therefore, we are able to see the vaporization after the generation of spray.

5.6.2. Drop-on-Demand Inkjet Induced by Pulsed Laser

To construct Drop-on-Demand inkjet system, liquid ejection from the nozzle needs to obtain a smaller velocity than spray inkjet system. Therefore, intensive explosive boiling of ink induced by pulsed laser is adopted. The resulting droplet patterns vary from microscale sprays to separated droplets varies with laser energy.

Aperture size of the nozzle used here is less than 1.0 μm. After filling the nozzle, continuous laser (λ=650nm) was first coupled into the nozzle to confirm the alignment. Then pulsed laser light (λ=650nm with 4 ns pulse duration) was delivered to the nozzle following the same optical path. Two different laser energies, namely, 1 nJ and 1.4 nJ, were examined in this study. Phase contrast image of the experimental results with these two laser energy was presented in Figure 68.

With the increase of pulsed laser energy, micro droplet ejected from the nozzle become small spray due to the increment of pressure generated by LIEB inside the probe.

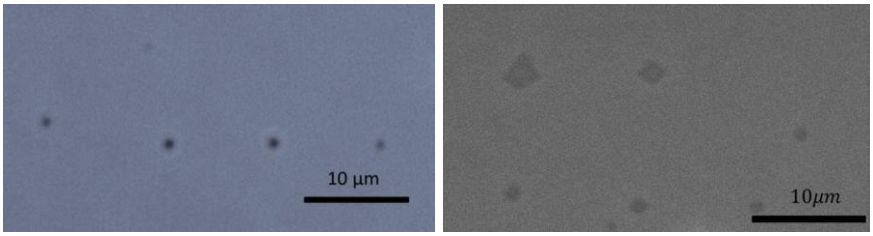

Figure 68 Phase contrast image of DoD droplets with 1nJ (left) and 1.4 nJ (right) with ns pulse laser

5.6.3. Discussion

When the laser strikes the inner coating of a tapered nano-nozzle, the optically induced joule heating can rapidly heat the Au inner coating of the nano-nozzle[95]. Such rapid increase of the temperature of the nano-nozzle can raise the temperature of adjacent ink to a temperature higher than its boiling temperature through conduction. Explosive boiling of ink material then induced high pressure which is much higher than the room pressure. As a result, ink inside the nozzle can be squeezed out from the aperture of the nano-nozzle and forms a liquid jet when the pressure inside the nano-nozzle overcomes the surface tension of the ink at the aperture. When the velocity of the induced liquid ejection is high, the induced liquid jet breaks into a combination of droplets with diameters smaller than the aperture of the nozzle owing to very short wavelength hydrodynamic instability[95], which also causes the spray to travel in a wide angle from the aperture of the nozzle. Such droplet ejection was observed commonly when the liquid ejection is induced by continuous laser with high enough power.

To induce DOD ejection from the nano-nozzle, the velocity of the induced liquid from the aperture of the nano nozzle should be as small as possible[96]. Such requirement can be fulfilled when the intensive explosive boiling of the liquid is induced by pulsed

light. The pulse light provides short duration, controlled heating of the superheated ink which limits the amount of momentum supplied to the liquid jet by the explosive boiling. It is predicted in previous study[97] that the pulsed heating duration of the ink should be smaller than 1 μs (or even a few ns) if sub-micron DOD ink ejection is desired. Therefore, with ns pulsed laser of appropriate laser energy, DOD ink ejection was demonstrated in this study. To achieve a better consistency of the results from the DOD ejection, the laser energy should be more precisely controlled with less fluctuation during operation. Note that the examined laser driven scheme with nano-nozzles can be extended to generation of nano-droplets much smaller than 1 μm when nano-nozzles with much smaller apertures are applied.

5.7. Summary

The laser induced nano-inkjet is successfully demonstrated with continuous laser. Nano-spray with droplet diameter less than 500 nm can be achieved with glycerol as the ink. For liquid experiencing a regular boiling process, however, cannot result in observable nano-spray when they are adopted as inks. By replacing continuous laser with pulse laser and improve the light absorption of the nano-nozzle through additional metallic coating, pulsed localized heating can be confined to around the aperture of the nano-nozzle. As a result, explosive boiling of liquid can be induced, which will allow the observable nano-droplet ejection to be achieved with inks such as glycol and water.

6. CONCLUSION AND FUTURE RESEARCH

6.1. Conclusions

There is an increasing demand of high resolution printing techniques especially in electronics fabrication in recent decades. As a non-contact direct writing method, inkjet printing can reduce both chemical waste and interaction between substrate and top materials during fabrication. However, inkjet printing techniques are limited in the droplet size. We notice that the real limitation of inkjet techniques is the rapid increment of driven force which can be generated in various ink materials and less/or even no effect on substrate materials. In this PhD work, we proposed a non-contact laser induced inkjet printing technique using LIEB as driven force. LIEB have been proven to generate sudden high pressure when laser with high enough energy is interacting with target surface based on previous experimental and theoretical analysis.

The experimental part of the PhD work starts with the design and fabrication of micro-nozzle for the inkjet. The nozzle we proposed in this study is a tapered hollow probe fabricated by depositing metal coating on a pulled glass pipette. The aperture size of the generated nozzle can be precisely controlled during pulling process. Droplet can be generated by applying laser light with various energy and pulse duration into the nozzle. The absorptivity of laser light close to the tip can generate localized heating and induce phase change of liquid materials filled inside. Sudden vaporization of liquid material generates high pressure and squeezes liquid out from nozzle. With different laser energy and laser pulse duration, maximum pressure value can be different and achieve at different

time point. Therefore, various outcome velocity of ink material can be achieved which can form different patterns on the substrate. The experimental result in this study shows the generated patterns can vary from single droplet, to micro/large scale spray by apply ns pulsed laser or continuous laser light.

The second portion of this PhD study focuses on numerical analysis of fluid and energy transport of weakly compressible fluid (i.e., water) by meshfree method (SPH). The motivation of this theoretical analysis is to better understand the physics involved in LIEB and its associated flow characteristics. SPH was selected as the starting method for analyzing the fluid dynamics and energy transport problems with: (1) interfaces between liquid domain and background gas (top surface of liquid film); (2) rapid expansion of vapor bubble inside a liquid domain; (3) transient phase change between liquid and vapor under intense laser induced joule heating. Traditional SPH has its advantages in dealing with free surface and moving interface compared with traditional meshed CFD. However, in traditional SPH, to handle the thermally induced flow, Boussinesq approximation equation is required, which valid only when the temperature difference is small. Therefore, we first extended the traditional SPH by including EoS in the energy transport simulation, which allows us to simulate a wide range of thermally induced flow without BS assumption. However, through gain experience in traditional SPH simulation, we noticed the limitations of SPH in achieving high enough numerical accuracy in derivative computing and providing numerical stability without artificial smoothing process for low compressibility fluid (e.g., water). These limitations of traditional SPH prevent it as a valid

tool to study highly dynamic fluid transport problems driven by large temperature variation and rapid phase change (i.e., LIEB).

As result, we spent the remaining half the PhD study on developing a new meshfree scheme which can (a) handle thermally induced flow with equation of state directly, (b) handle weakly compressible flow such as water/glycerol which are commonly applied as the based solution of ink materials in inkjets without additional smoothing, (c) handle physical boundary conditions directly through mass/momentum/energy conservation with no special treatment. A high order accuracy meshfree scheme is introduced in this PhD study to better handle weakly compressible fluid directly. With this novel scheme, 2^{nd} and 1^{st} orders of accuracy in gradient and Laplacian calculation for randomly distributed simulating particles even higher accuracy in gradient and Laplacian calculation for symmetrically distributed simulating particle can be achieved. In additional to the development of the novel high order accuracy meshfree scheme, we also introduced remeshing method for this new scheme which can prevent formation of void regions of simulating particles during a meshfree calculation to ensure a long term simulation stability with the novel numerical scheme even with a boundary layer driven flow.

6.2. Future Research

The numerical analysis part in this study can be extended in the following ways for future research:

i. Direct simulation of free convection, phase change, and bubble dynamics without simplification such as Boussinesq Approximation.

ii. Direct simulation of pressure wave propagation inside liquid domain with/without phase change (micron cavitation process).

iii. Hydrodynamics with free surface, such as liquid ejection.

The experimental part in this study can also be extended in following ways:

i. Ink materials such as photo-epoxy can be used to better observe pattern size and shape by curing ink materials after deposited on the substrate.

ii. Laser induced inkjet system can also be applied in liquid environment and test liquid ejection with background pressure from surrounding liquid.

REFERENCES

1. J. Lawrence, J. Pou, D. K. Y. Low and E. Toyserkani, Advances in Laser Materials Processing Technology, Research and Applications Preface, (WoodHead Publishing in Mechanical Engineering, 2010), pp. 629-670.
2. F. J. Adrian, J. Bohandy, B. F. Kim, A. N. Jette and P. Thompson, J Vac Sci Technol B 5 (5), 1490-1494 (1987).
3. N. R. Schiele, D. T. Corr, Y. Huang, N. A. Raof, Y. B. Xie and D. B. Chrisey, Biofabrication 2 (3), 032001-032014 (2010).
4. S. G. Farah, D. T. Azar, C. Gurdal and J. Wong, J Cataract Refr Surg 24 (7), 989-1006 (1998).
5. H. K. Park, Dissertation Abstracts International 56-05 (Section: B), 2827 (1994).
6. H. K. Park, D. Kim, C. P. Grigoropoulos and A. C. Tam, J Appl Phys 80 (7), 4072-4081 (1996).
7. H. K. Park, X. Zhang, C. P. Grigoropoulos, C. C. Poon and A. C. Tam, J Heat Trans ASME 118 (3), 702-708 (1996).
8. O. Yavas, P. Leiderer, H. K. Park, C. P. Grigoropoulos, C. C. Poon, W. P. Leung, N. Do and A. C. Tam, Appl Phys A-Mater 58 (4), 407-415 (1994).
9. H. K. Park, C. P. Grigoropoulos, O. Yavas, W. P. Leung, C. Poon and A. C. Tam, Transport Phenomena in Thermal Engineering Volume 1, (Begellhouse, 1993), pp. 1084-1089.
10. G. R. Liu, Mesh Free Methods: Moving Beyond the Finite Element Method. (CRC Press, 2002).

11. E. Leveugle, A. Sellinger, J. M. Fitz-Gerald and L. V. Zhigilei, Phys Rev Lett 98 (21), 216101 (2007).

12. G. R. Liu and M. B. Liu, Smoothed Particle Hydrodynamics: A Meshfree Particle Method. (World Scientific, Singapore, 2003).

13. L. B. Lucy, Astron J 82 (12), 1013-1024 (1977).

14. R. A. Gingold and J. J. Monaghan, Mon Not R Astron Soc 181 (2), 375-389 (1977).

15. G. Lodato and D. J. Price, Mon Not R Astron Soc 405 (2), 1212-1226 (2010).

16. M. Gomez-Gesteira, A. J. C. Crespo, B. D. Rogers, R. A. Dalrymple, J. M. Dominguez and A. Barreiro, Comput Geosci-Uk 48, 300-307 (2012).

17. N. Sukumar and E. A. Malsch, Arch Comput Method E 13 (1), 129-163 (2006).

18. W. Dehnen and H. Aly, Mon Not R Astron Soc 425 (2), 1068-1082 (2012).

19. H. Wendland, Adv Comput Math 4 (1), 389-396 (1995).

20. J. J. Monaghan, Annu Rev Astron Astr 30, 543-574 (1992).

21. J. J. Monaghan, Rep Prog Phys 68 (8), 1703-1759 (2005).

22. J. J. Monaghan, Universitext, (Springer, 2005), pp. 143-194.

23. A. Colagrossi, PhD Thesis, University a di Roma La Sapienza (2004).

24. S. Rosswog, Mon Not R Astron Soc 448 (4), 3628-3664 (2015).

25. D. J. Price, J Comput Phys 231 (3), 759-794 (2012).

26. L. Brookshaw, P Astron Soc Aust 6 (2), 207-210 (1985).

27. D. Garcia-Senz, R. M. Cabezon and J. A. Escartin, Astron Astrophys 538, A9 (2012).

28. A. Khayyer and H. Gotoh, Appl Ocean Res 37, 120-126 (2012).

29. A. Khayyer and H. Gotoh, Appl Ocean Res 32 (1), 124-131 (2010).

30. W. K. Liu and Y. J. Chen, Int J Numer Meth Fl 21 (10), 901-931 (1995).

31. H. Ikari, A. Khayyer and H. Gotoh, Journal of Ocean Engineering and Marine Energy 1 (4), 361-376 (2015).

32. E. S. Lee, C. Moulinec, R. Xu, D. Violeau, D. Laurence and P. Stansby, J Comput Phys 227 (18), 8417-8436 (2008).

33. P. W. Cleary and J. J. Monaghan, J Comput Phys 148 (1), 227-264 (1999).

34. G. L. Vaughan, T. R. Healy, K. R. Bryan, A. D. Sneyd and R. M. Gorman, Int J Numer Meth Fl 56 (1), 37-62 (2008).

35. A. J. C. Crespo, M. Gomez-Gesteira and R. A. Dalrymple, Cmc-Comput Mater Con 5 (3), 173-184 (2007).

36. J. J. Monaghan and A. Kos, J Waterw Port C-Asce 125 (3), 145-154 (1999).

37. R. P. Fedkiw, J Comput Phys 175 (1), 200-224 (2002).

38. S. Kulasegaram, J. Bonet, R. W. Lewis and M. Profit, Comput Mech 33 (4), 316-325 (2004).

39. J. Bonet, S. Kulasegaram, M. Rodriguez-Paz and M. Profit, Comput Method Appl M 193 (12-14), 1245-1256 (2004).

40. A. Mayrhofer, B. D. Rogers, D. Violeau and M. Ferrand, Comput Phys Commun 184 (11), 2515-2527 (2013).

41. S. Adami, X. Y. Hu and N. A. Adams, J Comput Phys 231 (21), 7057-7075 (2012).

42. H. Takeda, S. M. Miyama and M. Sekiya, Prog Theor Phys 92 (5), 939-960 (1994).

43. M. E. Danis, M. Orhan and A. Ecder, Int J Comput Fluid D 27 (1), 15-31 (2013).

44. A. M. Aly, Int J Numer Method H 25 (3), 513-533 (2015).

45. K. Szewc, J. Pozorski and A. Taniere, Int J Heat Mass Tran 54 (23-24), 4807-4816 (2011).

46. K. Johannsen, Computat Geosci 7 (3), 169-182 (2003).

47. W. R. Boos, J. R. Scott and K. A. Emanuel, J Phys Oceanogr 34 (1), 334-341 (2004).

48. M. Gomez-Gesteira, B. D. Rogers, A. J. C. Crespo, R. A. Dalrymple, M. Narayanaswamy and J. M. Dominguez, Comput Geosci-Uk 48, 289-299 (2012).

49. J. P. Morris, P. J. Fox and Y. Zhu, J Comput Phys 136 (1), 214-226 (1997).

50. M. Meister, G. Burger and W. Rauch, J Hydraul Res 53 (1), 149-149 (2015).

51. J. W. Swegle, S. W. Attaway, M. W. Heinstein, F. J. Mello and D. L. Hicks, Report No. SAND--93-2513; Other: ON: DE94013817; TRN: 94:006512 United States10.2172/10159839 SCA: 360103; 990200; PA: EDB-94:094794; ERA-19:021962; NTS-94:020022; SN: 94001036853 English, 1994.

52. Matthias Müller , David Charypar , Markus Gross, Particle-based fluid simulation for interactive applications, Proceedings of the 2003 ACM SIGGRAPH/Eurographics symposium on Computer animation, July 26-27, 2003, San Diego, California

53. P. W. Cleary, Appl Math Model 22 (12), 981-993 (1998).

54. H. A. Luther, Mathematics of Computation 22 (102), 434-436 (1968).

55. A. M. Aly and S. E. Ahmed, Int J Heat Mass Tran 77, 1155-1168 (2014).

56. R. Hyland and A. Wexler, Ashrae J 25 (5), 64-64 (1983).

57. J. Patterson and J. Imberger, J Fluid Mech 100 (Sep), 65-86 (1980).

58. Y. Z. Amir Faghri, John Howell, Advanced Heat and Mass Transfer. (Global Digital Press, 2010).

59. A. V. Getling, Usp Fiz Nauk+ 161 (9), 1-80 (1991).

60. Q. R. Zhu, L. Hernquist and Y. X. Li, Astrophys J 800 (1), 6 (2015).

61. R. Di Lisio, E. Grenier and M. Pulvirenti, Comput Math Appl 35 (1-2), 95-102 (1998).

62. J. Bonet and T. S. L. Lok, Comput Method Appl M 180 (1-2), 97-115 (1999).

63. Z. He, PhD Thesis, University of Delaware, Department of Mathematical Sciences (2015).

64. S. Gottlieb, C. W. Shu and E. Tadmor, Siam Rev 43 (1), 89-112 (2001).

65. A. K. Chaniotis, D. Poulikakos and P. Koumoutsakos, J Comput Phys 182 (1), 67-90 (2002).

66. The OpenFOAM Foundation, www.openfoam.org .

67. Y. Tsuboi, H. Fukumura and H. Masuhara, J Phys Chem-Us 99 (25), 10305-10312 (1995).

68. S. I. Kudryashov and S. D. Allen, J Appl Phys 100 (10), 104908-1-11 (2006).

69. I. Apitz and A. Vogel, Appl Phys a-Mater 81 (2), 329-338 (2005).

70. A. Bencsura, V. Navale, M. Sadeghi and A. Vertes, Rapid Commun Mass Sp 11 (6), 679-682 (1997).

71. A. Bencsura and A. Vertes, Chem Phys Lett 247 (1), 142-148 (1995).

72. L. V. Zhigilei, P. B. S. Kodali and B. J. Garrison, Chem. Phys. Lett. 276 , 269-273 (1997).

73. L. V. Zhigilei, P. B. S. Kodali and B. J. Garrison, J Phys Chem B 101 (11), 2028-2037 (1997).

74. S. N. Andreev, S. V. Orlov and A. A. Samokhin, Phys. Wave Phen. 15 (2), 67-80 (2007).

75. Y. S. Dou, L. V. Zhigilei, N. Winograd and B. J. Garrison, J Phys Chem A 105 (12), 2748-2755 (2001).

76. A. Vogel, S. Busch and U. Parlitz, J Acoust Soc Am 100 (1), 148-165 (1996).

77. A. Vogel, U. Parlitz and S. Busch, P Soc Photo-Opt Ins 2391, 74-88 (1995).

78. J. Bohandy, B. F. Kim and F. J. Adrian, J Appl Phys 60 (4), 1538-1539 (1986).

79. J. A. Barron, P. Wu, H. D. Ladouceur and B. R. Ringeisen, Biomed Microdevices 6 (2), 139-147 (2004).

80. G. D. Martin and I. M. Hutchings, in Inkjet Technology for Digital Fabrication (John Wiley & Sons, Ltd, 2012), pp. 21-44.

81. L. Rayleigh, Proceedings of the Royal Society of London 29 (196-199), 71-97 (1879).

82. L. Rayleigh, Proceedings of the London Mathematical Society s1-10 (1), 4-13 (1878).

83. R. P. Grant and Middlema.S, Aiche J 12 (4), 669-678 (1966).

84. C. Weber, Z Angew Math Mech 11, 136-154 (1931).

85. R. D. REITZ, Ph.D. Thesis, Princeton University (1978).

86. K. Seung Hwan, C. Jaewon, H. Nico, N. Koo Hyun and P. G. Costas, J. Micromech and Microeng 20 (12), 125010 (2010).

87. V. Sanchez-Romaguera, M.-B. Madec and S. G. Yeates, Reactive and Functional Polymers 68 (6), 1052-1058 (2008).

88. J.-U. Park, M. Hardy, S. J. Kang, K. Barton, K. Adair, D. k. Mukhopadhyay, C. Y. Lee, M. S. Strano, A. G. Alleyne, J. G. Georgiadis, P. M. Ferreira and J. A. Rogers, Nat Mater 6 (10), 782-789 (2007).

89. K. Kaisei, N. Satoh, K. Kobayashi, K. Matsushige and H. Yamada, Nanotechnology 22 (17) (2011).

90. J. W. van Honschoten, G. J. M. Krijnen, V. B. Svetovoy, H. E. de Bree and M. C. Elwenspoek, "Optimization of a two-wire thermal sensor for flow and sound measurements," Technical Digest. MEMS 2001. 14th IEEE International Conference on Micro Electro Mechanical Systems (Cat. No.01CH37090), Interlaken, Switzerland, 2001, pp. 523-526.

91. W. Sy-Bor, Journal of Physics D: Applied Physics 43 (28), 285502 (2010).

92. S. Alok and W. Sy-Bor, Journal of Physics D: Applied Physics 45 (18), 185101 (2012).

93. G. G. Jang and D. K. Roper, J Phys Chem C 113 (44), 19228-19236 (2009).

94. E. Farnetti, J. Kaspar and C. Crotti, Green Chem 11 (5), 704-709 (2009).

95. S. P. Lin and R. D. Reitz, Annu Rev Fluid Mech 30, 85-105 (1998).

96. J. R. Castrejon-Pita, N. F. Morrison, O. G. Harlen, G. D. Martin and I. M. Hutchings, Phys Rev E 83 (3), 036306 (2011).

97. Y. Wang, J. Bokor and A. Lee, P Soc Photo-Opt Ins 5374, 628-636 (2004).